Phase and Amplitude Dynamics of Quantum Self-Oscillators

Inauguraldissertation

zur

Erlangung der Würde eines Doktors der Philosophie

vorgelegt der

Philosophisch-Naturwissenschaftlichen Fakultät

der Universität Basel

von

Ehud Amitai

von

Israel

Basel, 2018

Genehmigt von der Philosophisch-Naturwissenschaftlichen Fakultät

auf Antrag von

Prof. Dr. Christoph Bruder
Prof. Dr. Andrew Armour

Basel, 26.06.2018

Prof. Dr. Martin Spiess
The Dean of Faculty

Abstract

Department of Physics

Ph.D.

Phase and Amplitude Dynamics of Quantum Self-Oscillators

by Ehud Amitai

Self-oscillators form a special class of oscillators, generating and maintaining a periodic motion while having some (or complete) independence of the frequency spectrum of oscillations from the spectrum of their power source. Pendulum clocks, brain neurons, fireflies, and cardiac pacemaker cells, are all examples of self-oscillators. Self-oscillations are not limited to the regime of classical physics, but are seen in the quantum regime as well. In both regimes, self-oscillators may demonstrate two intriguing phenomena: (1) Synchronization, a phenomenon in which self-oscillators adjust their rhythm due to weak coupling to a drive or to another self-oscillating systems; (2) Amplitude death, a phenomenon in which two or more coupled self-oscillators approach a stable rest-state. In the work presented in this thesis, we have mostly investigated these phenomena in quantum self-oscillators.

Chapter 2 tries to answer the question "Are there quantum effects in the synchronization phenomenon, which cannot be modeled classically?" Using a quantum model of a self-oscillator with nonlinearity in its energy spectrum, we have answered this question in the affirmative. We have demonstrated that the anharmonic, discrete energy spectrum of the oscillator leads to multiple resonances in both phase locking and frequency entrainment.

Coupling two quantum anharmonic self-oscillators, we show in Ch. 3 that genuine quantum effects are also expected in the amplitude death phenomenon. This is apparent in the multiple resonances of the mean phonon number of the oscillators, reflecting their quantized nature.

Chapter 4 is concerned with the investigation of the synchronization phenomenon in an experimental system, an optomechanical cell coupled to a drive. In the classical parameter regime, we derive analytical Adler equations describing the synchronization of the optomechanical cell to two different drives: (1) an optical drive and (2) a mechanical drive. We demonstrate numerically that synchronization should also be observed in the quantum parameter regime.

In Ch. 5 we describe our work in the field of Cooper pair splitters, a device consisting of two quantum dots side-coupled to a conventional superconductor. In this work, we go beyond the standard approximation of assuming the quantum dots to have a large charging energy. We derive a low-energy Hamiltonian describing the system, and suggest a scheme for the generation of a spin triplet state shared between the quantum dots, therefore extending the capabilities of the Cooper pair splitter to create entangled nonlocal electron pairs.

Acknowledgements

In conducting the research covered in this thesis, spanning a period of over three years, I have disturbed, interrupted, interrogated and emailed many people, yet I have never once met anything but patience and politeness. I thank them all. I would also like to thank by name at least part of this list of people:

First and foremost, Prof. Christoph Bruder deserves a big thank you for allowing me to become a member of his wonderful group and for giving me the opportunity to research under his wing. During this research time period, and thanks to his supervision, I have been immersed in interesting scientific research, have developed my personal scientific skills, and have even had personal insights. For all of the above, for helping me define goals, for providing a healthy environment, for being always available, and for everything that wasn't mentioned, thank you Christoph!

I would also like to thank Prof. Andrew Armour for accepting the role of a co-referee in my Ph.D. defense. This requires time and effort, and I am very grateful for his willingness to do so.

Another big thank you is in order for Prof. Martino Poggio, for agreeing to be the chair of this defense. This is much appreciated, and I am very thankful for that.

In the department of physics, I was lucky to find colleagues and friends which have contributed much to my scientific development, and for my personal well being as well. I am very happy to have had the opportunity to collaborate scientifically with Dr. Rakesh P. Tiwari, Dr. Stefan Walter, Prof. Thomas L. Schmidt, Dr. Simon E. Nigg, Dr. Niels Lörch, Dr. Andreas Nunnenkamp and Dr.-to-be Martin Koppenhöfer. I have learned a great deal from each name in this respectable list, and am very grateful for that. One more respectable name that ought be mentioned, is Tibor Sekera. For fruitful discussions regarding the foundations of quantum mechanics, love, lucid dreaming, Slovakian politics, salsa, and basically anything that comes to mind, thank you!

In supporting this thesis behind the scenes, there is an endless amount of people that should be thanked. So thank you! I would also enjoy adding a personal note to some of them:

Woman, Dubinho, Missy and Yogi, thank you for always providing me a place called home. Whether physically near or far, I always feel it is right next to me. Pashi, thank you for everything. Forever part of me. Chocho, for carrying me when needed, for a

second home, thank you. Armelle, for the pleasure of knowing you, for teaching what strength is, I'm forever grateful. DJ Yoo, Niggro, Shishu, Ophirush, and Osmo, having friends like you is a great luxury, and I appreciate it soooo much. Thank you.

CONTENTS

ACRONYMS

EOM	**E**quation **O**f **M**otion
vdP	**v**an **d**er **P**ol
FPE	**F**okker-**P**lanck **E**quation
CPS	**C**ooper **P**air **S**plitter
EPR	**E**instein-**P**odolsky-**R**osen
QD	**Q**uantum **D**ot
BCS	**B**ardeen-**C**ooper-**S**chrieffer
SW	**S**chrieffer-**W**olff

CHAPTER 1

THEORETICAL BACKGROUND

"Just the facts, ma'am"

Dan Aykroyd, Sgt. Joe Friday in the pseudo-parody Dragnet (was actually not said by Sgt. Joe Friday in the Dragnet radio or television series)

In this thesis, we describe our scientific research and discoveries that shed light on quantum effects in the phase and amplitude dynamics of quantum self-oscillators, and our contribution to quantum state engineering using Cooper pair splitters (CPSs). This work did not, however, come out of the blue. It is best viewed in the context of recent research [1, 12, 18, 55, 57, 59, 71, 72, 82, 83, 134, 135, 138, 139, 142, 143, 151], placing additional building blocks on already grounded foundations. In order to better understand the work described in this thesis, it is therefore required to understand many relevant concepts and recent advances. While it is beyond the scope of this thesis to indeed review all the required knowledge, we try in this chapter to explain and put into context the most relevant part of it.

In Sec. 1.1 we discuss what defines and what are the characteristic features of a self-oscillator [10, 99]. In part 1.1.1 of this section we discuss a generic model of a self-oscillator, the van der Pol (vdP) model [130, 131]. We will show that this model contains the essential characteristics of a self-oscillator, discuss its classical description, and move further to discuss rather recent advances: The description of a vdP oscillator in the quantum regime [72, 134]. This quantum vdP oscillator is used in the works presented in Ch. 2 and in Ch. 3. We then describe the phase dynamics of self-oscillators that lead to the phenomenon of synchronization in part 1.1.2 of this section. We explain the classical phenomenon [10, 99], its quantum generalization [1, 12, 71, 72, 134, 135, 139], and briefly discuss how to quantify synchronization in the quantum regime. In part 1.1.3 we explain the amplitude-death phenomenon: Dissipatively coupling two self-oscillators may result in the decay and even complete stop of their oscillations. We discuss classical and quantum [57] descriptions of this phenomenon. In part 1.1.4 we describe a specific experimental platform in which self-oscillations may be observed, the optomechanical

system. We turn to introduce the different topic of CPSs in Sec. 1.2. Throughout the body of work presented in this thesis, we have relied in our description on time-evolution equations for quantum systems. Specifically, the master equation for the time-evolution of a density matrix and the time-evolution equation for the Wigner function. We briefly discuss the essentials of these in Sec. 1.3.

1.1 Self-oscillators

Self-oscillators form a special class of all oscillators [10, 99], containing diverse oscillating objects such as pendulum clocks, blinking fireflies, contracting human hearts, chemical Belousov-Zhabotinsky reactions, and brain neurons. As their name suggests, self-oscillators generate and maintain a periodic motion while having "the complete or partial independence of the frequency spectrum of oscillations from the spectrum of the energy (power) source" [10, 70]. This description of self-oscillators implies that the following essential features must be present in a self-oscillating system:

- Incoherent power source – in order to generate a periodic motion, or maintain one in the presence of dissipation, the self-oscillator must contain a source of power. This power source needs to be incoherent to allow for the independence of the frequency spectrum of the self-oscillator from its own frequency spectrum (a forced harmonic oscillator is therefore not a self-oscillator).
- Dissipation – to maintain a periodic motion in the presence of a power source, some dissipative mechanism is needed to balance the energy gain.

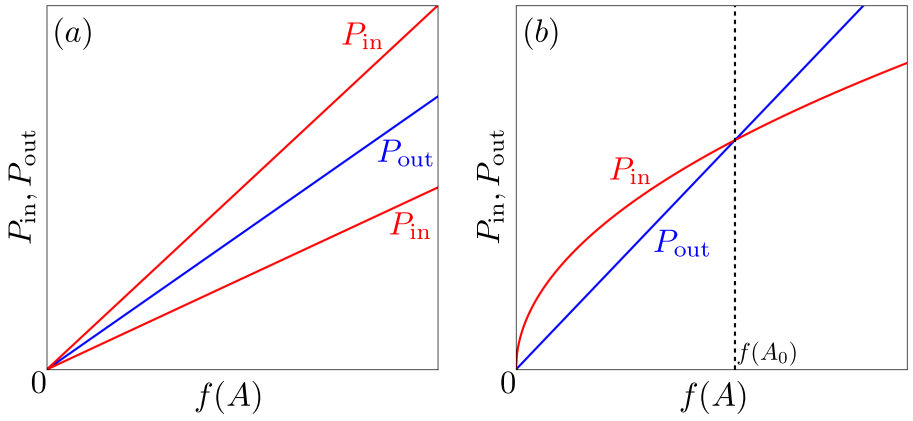

FIGURE 1.1: The dependence of the power entering the system P_{in} and the power leaving the system P_{out} as a function of $f(A)$. (a) When the dependence of both P_{in} and P_{out} is linear, the system would always gain or, alternatively, lose energy. No stable-amplitude oscillations can occur. (b) When the dependence of at least one of P_{in} and P_{out} is nonlinear (in this example – P_{in}), oscillations with stable amplitude A_0 may develop.

- Nonlinearity – The power entering the system via the power source P_{in} and the amount of power leaving the system via dissipation P_{out} are proportional to some function of the amplitude of oscillations $f(A)$. As shown in Fig. 1.1 (a), if both P_{in} and P_{out} are linear functions of $f(A)$, no stable periodic motion can be produced. If at least one of P_{in} and P_{out} are nonlinear, a stable periodic motion can be maintained, as shown in Fig. 1.1 (b).

This description of a self-oscillator, and these essential features, are also reflected in the phase space picture of a self-oscillator. Since the motion of a self-oscillator is periodic, its trajectory in phase space is a closed loop. Considering self-oscillators that can be described using the position and momentum coordinates only, we show examples of closed loops in Fig. 1.2 (a). As shown, these closed loops need not be circles. However, for closed loops which are sufficiently close to a circle, the notion of phase ϕ and amplitude A_0 can be easily defined, as depicted in Fig. 1.2 (a). Other trajectories in the vicinity of the closed loop, will tend towards it. This is because trajectories with smaller (larger) amplitudes would gain more (less) energy than they dissipate, therefore growing (shrinking) in amplitude. Once a trajectory coincides with the closed loop, it is in energetic equilibrium, and the amplitude is stable. For that reason, perturbations in the amplitude will decay, returning to the stable amplitude A_0, as seen in Fig. 1.2 (b). Since the other trajectories in its vicinity spirals into it as time approaches infinity, the closed loop is also named *limit-cycle*, and self-oscillators are named *limit-cycle oscillators*. While the amplitude of the self-oscillator is stable, the phase of the self-oscillator is free. This is a direct result of the incoherence of the power spectrum. All values of ϕ are equivalent, and therefore if an initial phase ϕ_0 is changed via some perturbation to ϕ_1, the perturbation neither grows nor decays. An example for it is shown in Fig. 1.2 (b).

1.1.1 The van der Pol model

As mentioned before, self-oscillations are widespread in natural and engineered systems, and self-oscillators contain diverse oscillating objects. When studying phenomena related to self-oscillations, one can focus on specific systems which demonstrate self-oscillations and study them in detail (as we have done in Ref. [3] and show in Ch. 4). However, when one is interested in studying more fundamental phenomena, common to many different kinds of self-oscillators, a platform-independent model is required. Exactly such a prototypical model of a self-oscillator was provided by Balthazar van der Pol in 1926 [130]. In the following, we briefly describe the vdP model for classical self-oscillators. Then we turn to discuss the quantum vdP model [72, 134]. The quantum model is a generalization of the vdP model to the quantum regime.

The classical model

The equation of motion (EOM) describing a damped harmonic oscillator is

$$\ddot{x} + \gamma\dot{x} + \omega_m^2 x = 0, \tag{1.1}$$

where x is the position coordinate, γ describes dissipation, and ω_m is the natural frequency of oscillation. The equation of the vdP oscillator is

$$\ddot{x} + \left(-G + 8\kappa x^2\right)\dot{x} + \omega_m^2 x = 0. \tag{1.2}$$

By comparing the vdP oscillator to the damped harmonic oscillator, we easily see that $G > 0$ describes a negative linear dissipation rate (or energy gain rate), while $\kappa > 0$ describes a nonlinear dissipation rate. We can also understand the emergence of limit-cycles in this model in an intuitive fashion: For very small x, the system gains energy more than it dissipates, therefore the oscillations are increasing in amplitude. For very large x, the system dissipates energy more than it gains, therefore the oscillations are decreasing in amplitude. Some attracting trajectory in phase space should therefore be formed. Furthermore, we see that there is nonlinearity present. These are exactly the requirements described previously for a self-oscillator. The periodicity of the vdP oscillator range from harmonic to a triangle wave (van der Pol has indeed used the model to describe relaxation oscillators, simulating the biological heart [131]). Limit-cycles of

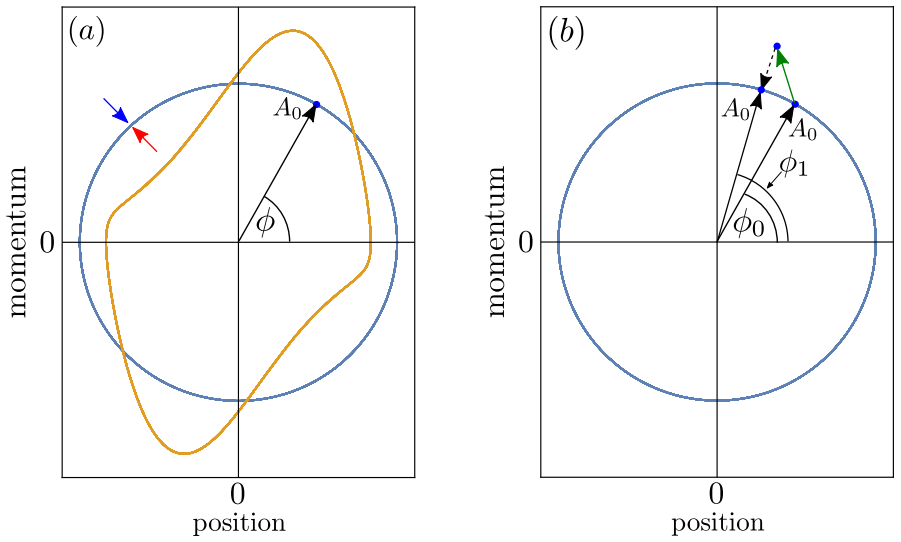

FIGURE 1.2: (a) Two forms of limit-cycles in phase space. Phase space points in the vicinity of a limit-cycle are attracted to it due to the processes of energy gain and energy dissipation, which are marked by red and blue arrows respectively. For a circular limit-cycle the definition of the stable amplitude A_0 and the phase of oscillation ϕ are standard and intuitive. (b) In a frame rotating with the frequency of oscillation, the periodic oscillation correspond to a stationary point (blue full circle) on the limit-cycle. Perturbing the oscillator (marked by a green arrow) will lead to a decay of the amplitude perturbation (dashed arrow), while the perturbation of the phase remains.

the vdP oscillator are shown in Fig. 1.2 (a). In a weak nonlinear regime, for which the limit-cycles are almost circular, the above vdP equation is reduced to a generic amplitude equation [10],

$$\dot{\alpha} = \left(-i\omega_m + G/2 - \kappa|\alpha|^2\right)\alpha, \tag{1.3}$$

where $\alpha(t)$ is a complex amplitude. The vdP oscillator described by Eq. (1.3) exhibits a circular limit-cycle of amplitude $A_0 = \sqrt{G/(2\kappa)}$.

To obtain A_0, one should use radial coordinates and insert $\alpha = Ae^{i\phi}$ into Eq. (1.3) and then split the resulting equation into real and imaginary parts. This leads to

$$\dot{A} = \frac{G}{2}A - \kappa A^3,$$
$$\dot{\phi} = -\omega_m.$$

By requiring a stable amplitude, $\dot{A} = 0$, one obtains $A_0 = \sqrt{G/(2\kappa)}$. We can also see that the phase ϕ of the oscillator is changing linearly with time, as expected for a self-oscillator with a harmonic frequency.

The quantum model

To describe a quantum vdP oscillator, the following master equation (for a quick recapitulation of the master equation see Sec. 1.3.1) for the density matrix was proposed [72, 134]

$$\dot{\rho} = -i\left[\omega_m a^\dagger a, \rho\right] + G\mathcal{D}[a^\dagger]\rho + \kappa\mathcal{D}[a^2]\rho, \tag{1.4}$$

where $a^\dagger$ and a are the creation and annihilation operators of the quantum harmonic oscillator, and the Lindblad operator is defined as $\mathcal{D}[x]\rho \equiv x\rho x^\dagger - (x^\dagger x\rho + \rho x^\dagger x)/2$. This master equation describes an oscillator with natural frequency ω_m, which gains energy linearly with rate G and dissipates energy nonlinearly with rate κ. These are the previously-described features of a self-oscillator. Indeed, the EOM for the classical amplitude of oscillation, $\alpha \equiv \langle a \rangle$, which is obtained using the Heisenberg EOM and after employing a mean-field approximation, is just Eq. (1.3).

We would like to obtain the EOM for $\alpha = \langle a \rangle$,

$$\frac{\mathrm{d}\alpha}{\mathrm{d}t} = \frac{\mathrm{d}}{\mathrm{d}t}\mathrm{Tr}\left\{a\rho\right\} = \mathrm{Tr}\left\{a\frac{\mathrm{d}\rho}{\mathrm{d}t}\right\} = \mathrm{Tr}\left\{a\left(-i[\omega_m a^\dagger a, \rho] + G\mathcal{D}[a^\dagger]\rho + \kappa\mathcal{D}[a^2]\rho\right)\right\}, \tag{1.5}$$

where we have used Eq. (1.4) to replace $\mathrm{d}\rho/\mathrm{d}t$. Using the fact that the trace is invariant under cyclic permutations, and using the commutation relation $\left[a, a^\dagger\right] = 1$, one can then obtain the EOM for α. As an example, we explicitly demonstrate

the calculation for the energy gain term,

$$\begin{aligned} G\mathrm{Tr}\left\{\mathcal{D}[a^\dagger]\rho\right\} &= G\mathrm{Tr}\left\{a\left(a^\dagger\rho a - \frac{1}{2}aa^\dagger\rho - \frac{1}{2}\rho aa^\dagger\right)\right\} \\ &= G\left(\langle a^2a^\dagger\rangle - \frac{1}{2}\langle a^2a^\dagger\rangle - \frac{1}{2}\langle aa^\dagger a\rangle\right) \\ &= \frac{G}{2}\langle a\rangle = \frac{G}{2}\alpha. \end{aligned} \tag{1.6}$$

Continuing in a similar fashion with the other terms, one obtains Eq. (1.3).

To better illustrate inherently quantum features which are not present in the classical vdP model, we would like to visualize the density matrix ρ of the quantum vdP oscillator in phase space. For that purpose, we will use the Wigner density function $W(x,p)$ (for a quick recapitulation of the Wigner density function see Sec. 1.3.2). A prototypical example of the dynamics arising from the master equation Eq. (1.4) is shown in Fig. 1.3. Initialized in some state (a coherent state in this specific example), the phase space distribution adjusts (smearing-out along the phase direction in this example) until reaching a ring-like steady state. This steady state is the limit-cycle of the quantum vdP oscillator, obtained independently of the chosen initial state. Two main features distinguish this limit-cycle from the classical limit-cycle (Fig. 1.2):

- The quantum limit-cycle has a certain *width* along the radial direction. This reflects fluctuations in the amplitude of oscillation, and therefore it reflects the amount of noise present in the system. In stark contrast to the classical vdP oscillator, even in the absence of any noise source, some width remains. This is a

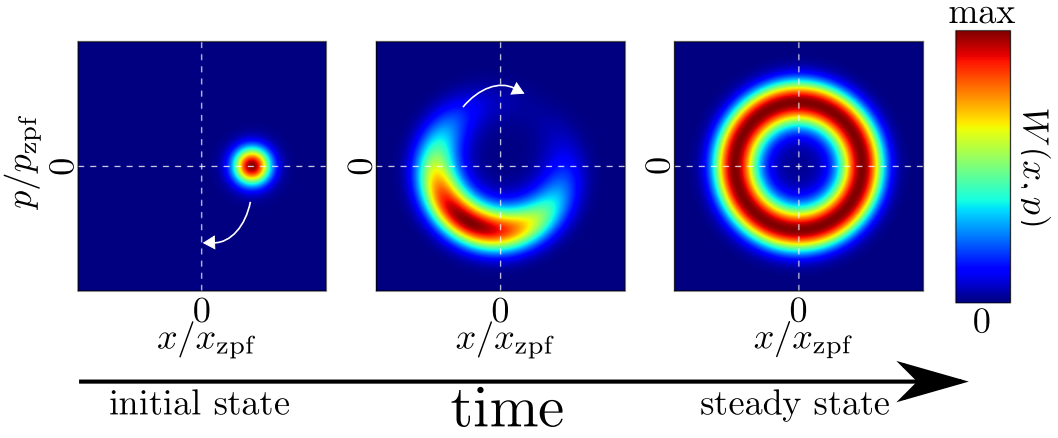

FIGURE 1.3: Time evolution of the Wigner density function $W(x,p)$ representing the state of the quantum vdP oscillator. From left to right: initialized in a coherent state, the state rotates in phase space (white arrows) and smears out along the phase direction, until reaching a ring-like steady state for which the phase is completely undetermined. This steady state is the limit-cycle for the quantum vdP oscillator. This figure is adapted from a similar figure appearing in Ref. [137].

direct result of the Heisenberg's uncertainty principle, $\sigma_x \sigma_p \geq \hbar/2$, where σ_x and σ_p are the standard deviations of the position x and momentum p, correspondingly. As the uncertainty principle disallows the localization of the quantum vdP oscillator in a certain point in phase space, it cannot occupy a determined radius. The quantum vdP oscillator therefore contains noise inherently, in contrast with a classical vdP oscillator.

- Though the limit-cycles of both the classical and quantum vdP oscillators are drawn as circles in phase space, only the quantum limit-cycle is in a steady state. The state of the classical oscillator is actually changing with time, moving in phase space along the limit-cycle trajectory. The ring-like quantum steady state represents a completely undetermined phase, and is the quantum analogue of the fact that the phase of the classical self-oscillator is free.

We would now like to discuss the feasibility of experimentally implementing a quantum vdP oscillator system. In the literature, mainly two platforms have been proposed as candidates [57, 72, 135]. The first promising platform is an ion trap with natural frequency ω_m, where a trapped ion has a ground state $|g\rangle$ and excited states $|e\rangle, |e'\rangle \ldots$, see Fig. 1.4. A linear energy gain rate can be obtained by exciting the ion via laser to an excited state $|e\rangle$ detuned by ω_m. Subsequently, the ion will decay to $|g\rangle$. The net result is the addition of one energy quanta. This process is done routinely in experiments [73]. In a similar fashion, by exciting the laser to an excited state $|e'\rangle$ detuned by $-2\omega_m$, one can remove two energy quanta, thus constructing a quantum vdP oscillator. The second suggested platform is a cavity optomechanical system [8], in which a quadratic optomechanical coupling needs to be established in addition to the standard linear coupling [92]. This is therefore relevant to the "membrane-in-the-middle" geometry [126] and to cold atoms localized within the electromagnetic cavity [100]. To understand the

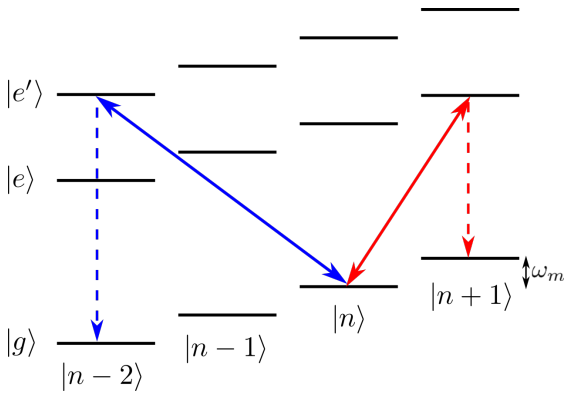

FIGURE 1.4: Quantum vdP oscillator can be implemented using an ion trap with natural frequency ω_m. Driving the ion via a laser detuned by ω_m to an excited state $|e\rangle$ (red arrow) will lead to a subsequent decay back to $|g\rangle$ (dashed arrow), and therefore causing a one-phonon gain process. Driving the ion via a laser detuned by $-2\omega_m$ to an excited state $|e'\rangle$ (blue arrow) will lead to a two-phonon loss process. Figure is adapted from a similar figure appearing in Ref. [72].

basic idea, let us discuss the "membrane-in-the-middle" setup. Utilizing the standard linear optomechanical coupling (see Sec. 1.1.4), we can drive a first cavity mode on the blue one-phonon sideband, therefore implementing the linear energy gain process. In addition, if the membrane is placed at a node or anti-node of the cavity field, the frequency of a second cavity mode is parametrically modulated by the position squared of the mechanical oscillator [92]. Then, one can drive the cavity with an additional laser on a red two-phonon sideband. This will lead to a two-phonon energy loss process. Implementing this will thus realize a quantum vdP oscillator.

In Ch. 2 and Ch. 3, we will use a Kerr quantum vdP oscillator model, i.e. a quantum vdP oscillator with an additional nonlinearity in its energy spectrum, obtained by an additional term in the Hamiltonian $K(a^\dagger a)^2$. In this context, we would like to further add that trapping potentials with very large anharmonicities in position can be realized [54, 136, 149]. Specifically, in Ch. 2 we discuss the limit $K \gg G + \kappa$. This can also be realized with almost lossless resonators, e.g. $K = 20$ kHz in Ref. [136] and typical heating rates on the order of 100 Hz [38]. For optimized systems [24, 45] heating rates on the order of Hz have been reported. In optomechanical systems, proposals for future engineering of strong Kerr anharmonicities have been made [58, 80, 105, 146].

1.1.2 Phase dynamics: Synchronization

Synchronization is the phenomenon in which a self-oscillator adjusts its rhythm due to weak coupling to a drive or to another self-oscillating system [10, 99]. "Frequency locking" describes a scenario in which the observed frequency of the self-oscillator matches the frequency of the drive or the frequency of other self-oscillators after synchronization has occurred. "Frequency entrainment" usually refers to the case in which the observed frequency is drawn closer (but do not match) to the synchronizing frequency. When the self-oscillator is frequency locked to a drive or to another self-oscillator, it implies a constant relative phase between the two. This is termed "phase locking". In many cases in which noise is present, strict frequency locking or phase locking cannot occur. In such cases, the self-oscillator develops some preference for the relative phase, in contrast to its originally completely free phase.

First observed and described by Dutch scientist Christian Huygens already in 1673 [56], the scientific understanding of synchronization has had a long history [124]. Synchronization may occur in every self-oscillatory system, and is therefore prevalent in all the natural sciences, manifesting itself in, for example, change of oscillation frequency in pendulum clocks, fireflies blinking in unison, adjustment of the circadian rhythm in many living systems, and in the memorizing process taking place in the brain [10, 99, 124].

In the following, we will focus only on the synchronization of a self-oscillator to an external harmonic reference signal. Understanding this simplest case of synchronization will be sufficient for the purposes of this thesis. To develop an intuitive understanding of the process, let us work in a frame rotating with the frequency of the drive, and assume

the self-oscillator and the drive are not coupled. If the frequency of the self-oscillator ω_m is identical to the frequency of the drive ω_d, i.e. $\Delta = \omega_d - \omega_m = 0$, then its phase space description is just a stable point (see Fig. 1.5 (a)). If however the detuning Δ has some finite value, this point will rotate (counter-clockwise for $\Delta < 0$ or clockwise for $\Delta > 0$), moving along a limit-cycle in phase space. When a weak coupling between the driving force and the self-oscillator is turned on, the drive can be represented by some constant vector in phase space (in the reference frame of the drive). When the state of the oscillator is represented by points 1 or 2 in Fig. 1.5 (a), the force acts only in a radial direction, trying to change the amplitude. Since the amplitude of the self-oscillator is stable, and the coupling between the drive and the self-oscillator is assumed weak, the force has no impact on these phase space points. When acting on other points along the limit-cycle, the force will have a radial contribution and a tangential contribution. The tangential contribution will change the phase of the oscillator. Examining the force diagram of points 3 to 6, we understand that the force will push the state of the self-oscillator towards state 1. If the detuning Δ is small enough, the drive will thus force the oscillator to remain in state 1, meaning that the frequency of the oscillator is now locked to the frequency of the drive.

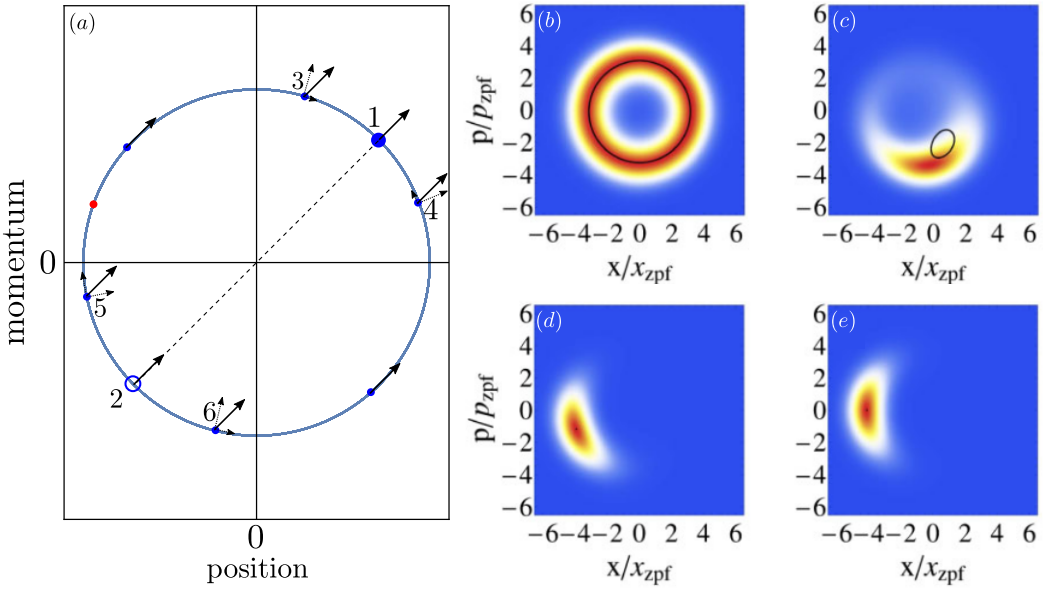

FIGURE 1.5: Synchronization of a self-oscillator to an external drive. (a) A generic phase-space diagram for a self-oscillator in the frame of reference of a driving field. When $\Delta = 0$, the state of the oscillator is described by stable phase space point (red dot). When $\Delta \neq 0$, a limit-cycle appears. In the presence of a forcing drive, a stable and unstable equlibrium points are created at points 1 and 2, correspondingly. If Δ is small enough, the oscillator will remain at point 1, therefore phase-locked to the drive. (b)-(e) Classical phase space trajectory of the vdP oscillator (black solid line), and the Wigner function representation of the quantum vdP oscillator, for $E/G = 1$ and $\kappa/G = 0.1$. (b) $\Delta/G = 16$, (c) $\Delta/G = 0.6$, (d) $\Delta/G = 0.1$, (e) $\Delta/G = 0$. Figures (b)-(e) are taken from Ref. [134].

We would now like to analyze the synchronization of our choice of prototypical self-oscillator, the vdP oscillator, to a drive. Classically, adding a drive term to Eq. (1.3) results in

$$\dot{\alpha} = \left(-i\omega_m + G/2 - \kappa|\alpha|^2\right)\alpha - E\cos(\omega_d t). \tag{1.7}$$

Working in the rotating frame of the drive is obtained via the transformation $\alpha \to \alpha e^{i\omega_d t}$. Evoking the rotating frame approximation, done by neglecting fast rotating terms with frequency $2\omega_d$, we obtain

$$\dot{\alpha} = \left(i\Delta + G/2 - \kappa|\alpha|^2\right)\alpha - E. \tag{1.8}$$

Quantum mechanically, adding a drive term to Eq. (1.4) and working in a frame rotating with the frequency of the external drive, results in the master equation

$$\dot{\rho} = -i\left[-\Delta a^\dagger a + iE(a - a^\dagger), \rho\right] + G\mathcal{D}[a^\dagger]\rho + \kappa\mathcal{D}[a^2]\rho. \tag{1.9}$$

Synchronization of the quantum vdP oscillator to an external drive, and the comparison to the classical scenario, was studied in Refs. [72] and [134]. Figure 1.5 (b)-(e), taken from Ref. [134], shows the Wigner density function for the quantum vdP oscillator, and the phase space trajectory of the classical vdP oscillator in solid black line, for different detuning values. As previously discussed, when Δ is large, the influence of the external drive is not sufficient to allow for phase-locking. The vdP oscillator is then moving along its limit-cycle (Fig. 1.5 (a)). As Δ is decreased, the classical vdP oscillator starts moving along a smaller trajectory, until finally becoming phase-locked to the drive. In the quantum mechanical case, this synchronization process manifests itself as a concentration of the Wigner density into a probability blob. The noise contained in the quantum description limits the ability to phase-lock. A complementary view

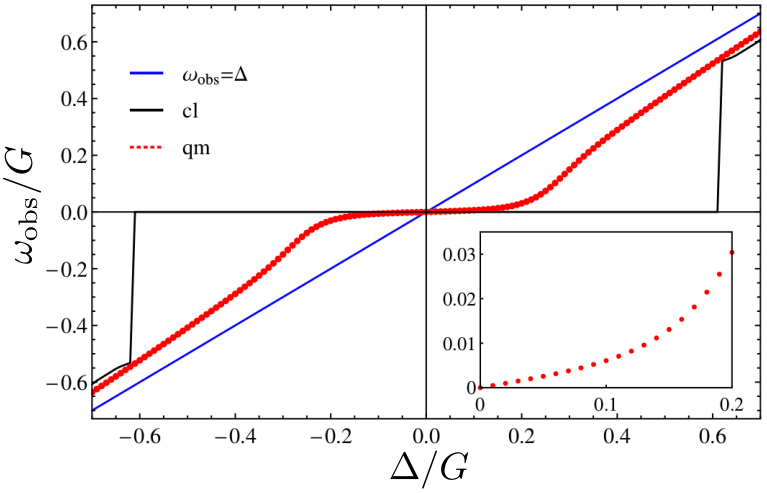

FIGURE 1.6: Observed frequency ω_{obs} as a function of detuning Δ, for $\kappa/G = 0.1$ and $E/G = 1$. Blue: undriven case. Black: classical model. Red: quantum model. Inset: zoom-in for the quantum case at small Δ. This figure is taken from Ref. [134].

of the process is obtained by examining the observed frequency of the vdP oscillator, ω_{obs}, as a function of the detuning. This is shown in Fig. 1.6, taken from Ref. [134] as well. For small enough Δ, the observed frequency of the classical vdP oscillator (black line) locks to the frequency of the external drive. In the quantum case, there is only frequency entrainment, as the noise does not allow for frequency locking (red line and inset). As Δ is increased, the observed frequency is increasingly independent of the drive frequency. Refs. [72] and [134] have demonstrated that for a quantum self-oscillator, in stark contrast to a classical self-oscillator, noise is inherent in the description. The effect of noise though, can also occur in a classical self-oscillator [10, 99]. In our work [77], described in Ch. 2, we have tried to find genuine quantum signatures in synchronization of self-oscillators, which cannot be found in classical descriptions.

While most works describing the synchronization of a quantum vdP oscillator to a drive focused solely on the case of an external harmonic drive [72, 77, 134], recent work [120] had shown that synchronization may also occur when applying a squeezing Hamiltonian to the quantum vdP oscillator. In fact, they had shown that applying a drive of the form $i\eta(a^2 - a^{\dagger 2})$ leads to enhancement of the synchronization, as compared with a harmonic drive $iE(a - a^\dagger)$. This enhancement manifest itself as stronger frequency entrainment, and as a narrower frequency distribution. This may help to experimentally observe quantum synchronization, as it strengthens the synchronization signal as compared with the noise found in the system.

In Sec. 1.1.1 we have discussed the feasibility of experimentally implementing a quantum vdP oscillator. Adding a forcing drive, in both the ion trap setup and the optomechanical setup, can be done by shining an additional laser. By changing the frequency of this harmonic drive, synchronization can be probed.

Quantifying synchronization

In contrast to the synchronization process of a classical noiseless self-oscillator to an external drive, when a quantum (noisy) self-oscillator synchronizes, strict frequency locking or strict phase locking does not occur. How can one then quantify the emergence of synchronization, manifesting itself in the phase preference developed by the self-oscillator? An intuitive way is looking at the phase distribution of a self-oscillator, and quantify synchronization as the emergence of peaks above a flat distribution (free phase). These peaks are reflected in the Wigner density function, in which a transition from a rotationally symmetric Wigner function to a more-concentrated Wigner function occurs. Such an approach is taken in our Refs. [77] and [3]. The synchronization measure is defined as the absolute value of the measure defined in Ref. [138], i.e.

$$S = |S|e^{i\theta} = \frac{\langle a \rangle}{\sqrt{\langle a^\dagger a \rangle}} = \frac{\text{Tr}\left[a\rho\right]}{\sqrt{\text{Tr}\left[a^\dagger a \rho\right]}} = \frac{\sum_{m=0}^{\infty} \langle m| a\rho |m\rangle}{\sqrt{\sum_{m=0}^{\infty} \langle m| a^\dagger a\rho |m\rangle}} = \frac{\sum_{m=0}^{\infty} \sqrt{m+1}\rho_{m+1,m}}{\sqrt{\sum_{m=0}^{\infty} m\rho_{m,m}}}. \tag{1.10}$$

The numerator holds information regarding the spread of the phase space distribution, while the denominator is introduced for the purpose of normalization. In cases where no phase-preference develops, the Wigner function (see Sec. 1.3.2) corresponding to ρ will be rotationally symmetric and $S \propto \langle a \rangle \propto \langle x + iP \rangle = 0$. In cases where there is only a small variation of the phase, such as in a coherent state, $|S| \to 1$. This measure will not work well in the presence of multiple-peaked phase space distributions. Still, as we are interested in the synchronization of a self-oscillator to a harmonic drive of one frequency only, S is adequate for our purposes.

1.1.3 Amplitude dynamics: Amplitude death

When coupling two or more self-oscillators, the oscillations of the entire system may be strongly suppressed and even approach a stable rest-state. Such behavior is relevant in diverse areas such as biological gene-regulating networks [128], chemical oscillators [11], and even in the flickering of nearby candles [93]. Different sorts of mechanisms may be responsible for this stabilization of the otherwise unstable rest state [69]: (a) a large frequency detuning between the oscillators, (b) existence of time-delay in the coupling, (c) coupling the oscillators via conjugate variables. This phenomenon is known in the literature as "amplitude death" or "oscillation death" [68, 69, 99, 112]. While both terms are often used, Ref. [68] distinguishes the case in which both oscillators approach an identical steady state, and the case in which each oscillator approaches a different steady state. "Amplitude death" refers to the former, while "oscillation death" refers to the latter. In our work [2] presented in Ch. 3, two dissipatively coupled self-oscillators stabilize their zero-amplitude rest-state via a Hopf bifurcation [6, 39, 88], therefore approaching an identical steady state. We keep this nomenclature, and use the term "amplitude death" for the work [2] described in Ch. 3.

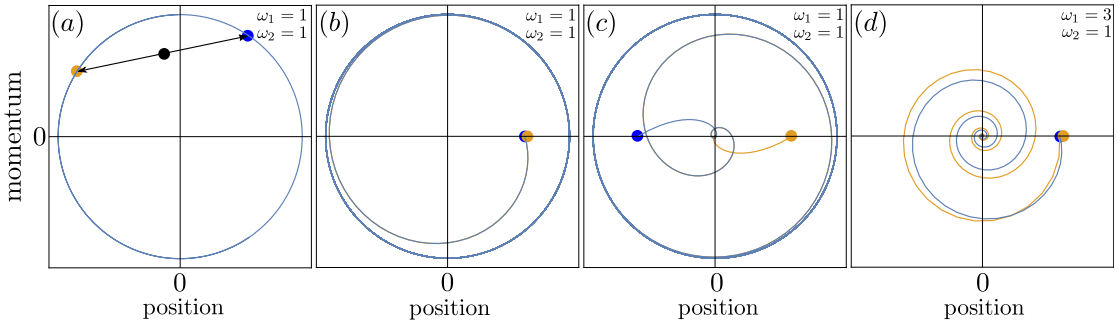

FIGURE 1.7: (a) The dissipative coupling attempts to pull the oscillators towards their average position. (b) When two identical oscillators have the same amplitude, the dissipative term has no effect. (c) When two identical oscillators have different amplitudes, the dissipative term acts to suppress the oscillations. When the oscillators reach an almost identical amplitude, the dissipative term has no effect, and oscillations grow back to the limit-cycle. (d) For different oscillators, being in a state of identical amplitude is only temporary. The dissipative term therefore stabilizes the rest-state. $\kappa/G = 0.2$ and $V/G = 2$ in all plots.

To gain an intuitive understanding, let us consider the most basic scenario of two dissipatively coupled classical vdP oscillators. Using Eq. (1.3), the coupled equations read

$$\begin{aligned}\dot{\alpha}_1 &= \left(-i\omega_m + G/2 - \kappa|\alpha_1|^2\right)\alpha_1 + \frac{V}{2}(\alpha_2 - \alpha_1),\\ \dot{\alpha}_2 &= \left(-i\omega_m + G/2 - \kappa|\alpha_2|^2\right)\alpha_2 + \frac{V}{2}(\alpha_1 - \alpha_2),\end{aligned} \tag{1.11}$$

where V denotes the strength of the dissipative coupling. The basic idea is that such a diffusive coupling attempts to pull the oscillators towards their average position in phase space (see Fig. 1.7 (a)). Because of that, the dissipative coupling will eventually lead the oscillators to an almost identical amplitude. At that point, the coupling which is proportional to the amplitude difference $\propto (\alpha_1 - \alpha_2)$ will have no effect. If the oscillators are identical, they will then follow identical trajectories, until oscillating along their limit-cycle. An example is shown in Fig. 1.7 (b)-(c). If the oscillators are far-enough detuned however, they will follow different-enough trajectories in phase space. The dissipative coupling will then completely suppress their oscillations, leading to amplitude death. This can be seen in Fig. 1.7 (d). Studying the stability of the rest-state, Ref. [6] predicted the rest-state to be stable in the regime $G < V < (\Delta^2 + G^2)/(2G)$. This can be seen in Fig. 1.8 (a), in which the amplitude-of-oscillation squared, $|\alpha_1|^2$, is shown as a function of Δ and V. The upper bound is the analytical equivalent of the intuitive explanation suggested in this paragraph. The lower bound is basically the requirement that the coupling strength is larger than the attraction of the limit-cycle.

What should we expect when dissipatively-coupling two quantum vdP oscillators? Will the amplitude death phenomenon still occur? How is this different than the classical case? Questions such as these were first studied in Ref. [57]. Building on Eq. (1.4), the master equation describing the dissipatively-coupled quantum vdP oscillators is given

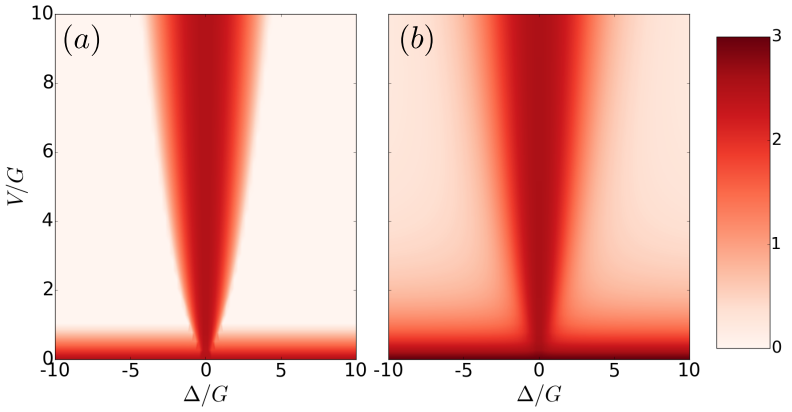

FIGURE 1.8: (a) The amplitude of oscillation squared $|\alpha_1|^2$ and (b) the mean phonon number $\langle a_1^\dagger a\rangle$, as a function of Δ and V. In (a), oscillations are completely suppressed in the regime $G < V < (\Delta^2 + G^2)/(2G)$. In (b), a more moderate suppression occurs, as the complete suppression is hindered by quantum noise. $\kappa/G = 0.2$ in both plots.

by

$$\dot{\rho} = \sum_{m=1}^{2} \left(-i[\omega_m a_m^\dagger a_m, \rho] + G\mathcal{D}[a_m^\dagger]\rho + \kappa\mathcal{D}[a_m^2]\rho \right) + V\mathcal{D}[a_1 - a_2]\rho. \tag{1.12}$$

This master equation reproduces Eq. (1.11) in the classical limit. Numerically simulating it, the mean phonon number of the first oscillator as a function of Δ and V is shown in Fig. 1.8 (b). Similar to the classical case, a strong suppression is seen in the regime $G < V < (\Delta^2 + G^2)/(2G)$. This means that amplitude death occurs when dissipatively-coupling quantum self-oscillators as well. In contrast to the classical noiseless case however, the complete suppression of oscillations is hindered by quantum noise, and is replaced by a more moderate suppression. That noise is inherent in the quantum description of the amplitude death phenomenon, in contrast with the classical description, was established in Ref. [57]. Still, classical self-oscillators may contain noise in their description, which will have a similar effect on the amplitude death phenomenon [95]. In our work [2], described in Ch. 3, we try to find quantum effects in the amplitude death phenomenon which cannot be obtained in any classical description.

In Sec. 1.1.1, we have commented on the possible experimental implementations of a quantum vdP oscillator, using trapped ions or cavity optomechanics. Obtaining a dissipative coupling in an optomechanical setup can be done by adding a cavity mode which is coupled linearly to two vdP oscillators and is driven by a laser. When the cavity mode dissipation rate is large, one can adjust the detuning between the driving laser and the natural frequency of this mode, allows to engineer the desired dissipative coupling [134]. In trapped ion systems, a Lindblad term $V\mathcal{D}[(a_1+a_2)(a_1-a_2)]\rho$ can be engineered using various techniques [30, 71, 114].

1.1.4 An experimental platform: Optomechanical systems

In previous subsections, we have discussed properties of self-oscillators. We have used a minimal model of a self-oscillator, which is able to capture these properties, the vdP model. In this section however, we would describe an experimental platform, the optomechanical system, which may exhibit self-oscillations as well. This is relevant to our work [3] which is presented in Ch. 4, in which we discuss how the optomechanical self-oscillatory state can be synchronized by an external drive.

An optomechanical system, in its most basic form, is a system in which one electromagnetic radiation field mode is coupled to one mechanical vibrational mode [8]. The simplest form of an optomechanical system is consisting of a Fabry-Pérot cavity, in which one of the two mirrors is mounted on a spring, and is free to oscillate. A schematic of the system is seen in Fig. 4.1. The photons in the cavity are impinging on the free-to-oscillate mirror, therefore transferring momentum. Due to this radiation pressure, the mirror will move. As it is doing so, the resonance frequency of the cavity is changed, leading to a different radiation field in the cavity. This backaction effect is the fundamental mechanism coupling the electromagnetic mode and the vibrational mode.

A Hamiltonian description is obtained by representing the electromagnetic (ω_c) and mechanical (ω_m) modes as harmonic oscillators,

$$H_0 = \omega_m b^\dagger b + \omega_c a^\dagger a, \tag{1.13}$$

where a and b are the optical and mechanical annihilation operators. In the simple scenario we have described so far, the cavity resonance frequency is modulated by the mechanical amplitude of oscillation,

$$\omega_c(x) \approx \omega_c + x\partial\omega_c/\partial x + \dots \quad . \tag{1.14}$$

In most cases, the second order term which is proportional to $\propto \partial^2\omega_c/\partial x^2$ can be neglected [8]. We then define the optical frequency shift per displacement, $G \equiv -\partial\omega_c/\partial x$. The Hamiltonian can then be written as

$$H_0 = \omega_m b^\dagger b + \omega_c a^\dagger a - g_0 a^\dagger a(b + b^\dagger), \tag{1.15}$$

where we have used $x = x_{\mathrm{zpf}}(b+b^\dagger)$ with x_{ZPF} being the zero-point fluctuation amplitude of the mechanical oscillator, and we have defined the vacuum optomechanical coupling strength, $g_0 \equiv G x_{\mathrm{ZPF}}$. We can add a Hamiltonian term describing a driving of the electromagnetic cavity by an external laser with frequency ω_L and strength E_L, $H_L = -iE_L(ae^{i\omega_L t} - a^\dagger e^{-i\omega_L t})$. It is then convenient to work in a frame rotating with the drive frequency. This can be easily accomplished by applying the unitary transformation $U = \exp(i\omega_L a^\dagger a t)$, leading to

$$H = \omega_m b^\dagger b - \Delta a^\dagger a - g_0 a^\dagger a(b + b^\dagger) - iE_L(a - a^\dagger), \tag{1.16}$$

where $\Delta = \omega_L - \omega_c$ is the detuning of the electromagnetic cavity frequency from the frequency of the laser drive.

Applying the unitary transformation $U = \exp(i\omega_L a^\dagger a t)$ will lead to a new Hamiltonian,

$$H = U H_{\mathrm{old}} U^\dagger - iU\frac{\partial U^\dagger}{\partial t}. \tag{1.17}$$

By using $Ua^\dagger U^\dagger = a^\dagger e^{i\omega_L t}$, $U\partial U^\dagger/\partial t = -i\omega_L a^\dagger a$, $UbU^\dagger = b$ and their complex conjugates, one obtains the transformed Hamiltonian.

In addition to the Hamiltonian description, which describes only the unitary dynamics of the optomechanical system, one should also take into account the dissipation of the electromagnetic cavity and of the mechanical oscillator. This dissipation occurs, e.g., because of light leaking out of the cavity with rate γ_c, or because of viscous damping caused by interactions of the mechanical oscillator with the surrounding gas atoms, leading to a mechanical dissipation rate γ_m. There are a few alternatives to account for this dissipation. One can use the input-output theory, which is formulated on the level of Heisenberg EOMs, and add terms such as $-\frac{\gamma_c}{2}a - \sqrt{\gamma_c}a_{\mathrm{in}}$ and $-\frac{\gamma_m}{2}b - \sqrt{\gamma_m}b_{\mathrm{in}}$

into the EOMs for the operators a and b, respectively [8, 26, 41]. The operators a_{in} and b_{in} represent quantum noise, and have zero mean $\langle a_{\text{in}} \rangle$. By taking the expectation value of these Heisenberg EOMs, one obtains classical equations for the amplitudes of the optical cavity and mechanical oscillator. We have simulated such equations later on in this thesis, see Eqs. (4.62) and (4.65). Another alternative mean to account for dissipation, is by using the Lindblad master equation [15, 19, 41, 132]. A discussion and derivation of the dissipative terms of the Lindblad master equation is presented below in Sec. 1.3.1. Using it, and the optomechanical Hamiltonian, Eq. (1.16), the master equation describing the time evolution of the density matrix of the optomechanical system is given by

$$\frac{\mathrm{d}\rho}{\mathrm{d}t} = -i\,[H, \rho] + \mathcal{L}_m \rho + \mathcal{L}_c \rho, \tag{1.18}$$

with the Lindblad operators

$$\mathcal{L}_m \rho = \gamma_m (n_{\text{th}}^{(m)} + 1)\mathcal{D}[b]\rho + \gamma_m n_{\text{th}}^{(m)} \mathcal{D}[b^\dagger]\rho, \tag{1.19}$$

and

$$\mathcal{L}_c \rho = \gamma_c (n_{\text{th}}^{(c)} + 1)\mathcal{D}[a]\rho + \gamma_c n_{\text{th}}^{(c)} \mathcal{D}[a^\dagger]\rho, \tag{1.20}$$

where $n_{\text{th}}^{(m)}$ and $n_{\text{th}}^{(c)}$ are the mean boson number in thermal equilibrium of the mechanical and electromagnetic cavity, respectively. For the electromagnetic cavity, $n_{\text{th}}^{(c)} = k_B T/\hbar\omega_c$ is close to zero for optical fields (other than microwave fields) at room temperature. We therefore approximate $n_{\text{th}}^{(c)} \approx 0$. As the mechanical frequency is much smaller, $\omega_m \ll \omega_c$, we cannot use the same approximation for the mechanical dissipation. The last master equation, with $n_{\text{th}}^{(c)} = 0$, constitutes our optomechanical quantum model presented in Ch. 4.

Generation of self-oscillations

As discussed previously in this section, in order for self-oscillations to be maintained, nonlinearity in the energy dissipation must be present. This nonlinearity is inherent to the optomechanical Hamiltonian, Eq. (1.16), as it contains terms of three operators. These terms lead to nonlinear Heisenberg EOMs, $\dot{a} = i\,[H_0, a]$ and $\dot{b} = i\,[H_0, b]$. Still, to better understand the regime in which self-oscillations begin, it is fruitful to examine a linearized version of H_0. The linearized approximation is obtained by splitting the electromagnetic cavity field into an average strong (classical) coherent amplitude $\langle a \rangle = \alpha$ and a fluctuating term, $a = \alpha + \delta a$. By placing the last expression into Eq. (1.16), the optomechanical interaction part of the Hamiltonian can be written as

$$H_{\text{int}} = -g_0 |\alpha|^2 (b + b^\dagger) - g_0 \left(\alpha^* \delta a + \alpha \delta a^\dagger\right)(b + b^\dagger) + \mathcal{O}(\delta a^\dagger \delta a), \tag{1.21}$$

where we have omitted the term proportional to $\delta a^\dagger \delta a$ as it is smaller by a factor $|\alpha|$. This linearized interaction Hamiltonian leads to multiple important results, many of which are described in Ref. [8]. We shall only describe the most important effects. One static

effect stems from the first term in Eq. (1.21), which indicates the presence of a constant radiation-pressure force, $\bar{F} = G|\alpha|^2$. This can be omitted by appropriately shifting the displacement's origin, and then use an effective detuning $\Delta_{\text{eff}} = \Delta + 2g_0^2|\alpha|^2/\omega_m$. A second effect, dynamical in nature, is termed the optical spring effect. According to it, the mechanical frequency is shifted as a result of the induced laser field. A third effect, is the optical induced damping of the mechanical oscillator. According to it, for sufficiently weak laser drive, $|\alpha|g_0 \ll \gamma_m$, the effective mechanical damping rate is given by

$$\gamma_{\text{eff}} = \gamma_m + \gamma_o, \tag{1.22}$$

where the optically induced damping rate is

$$\gamma_o = |\alpha|^2 g_0^2 \left(\frac{\gamma_m}{\gamma_m^2/4 + (\Delta + \omega_m)^2} - \frac{\gamma_m}{\gamma_m^2/4 + (\Delta - \omega_m)^2} \right). \tag{1.23}$$

This optical damping may be positive, if $\Delta < 0$. This will lead to additional damping, in a process called optomechanical cooling. The mechanical oscillator can even be cooled into the quantum ground state [84, 141]. This optical damping may also be negative, if $\Delta > 0$. In such a case, it can lead to amplification of thermal fluctuations, and finally to an instability if $\gamma_{\text{eff}} < 0$. An intuitive understanding of these processes may be developed in the scattering picture [8], see Fig. 1.9. In this picture, incoming laser photons of frequency ω_L may scatter into motional sidebands of frequency $\omega_L \pm \omega_m$. These motional sidebands become asymmetric for $\Delta \neq 0$ due to the cavity density of

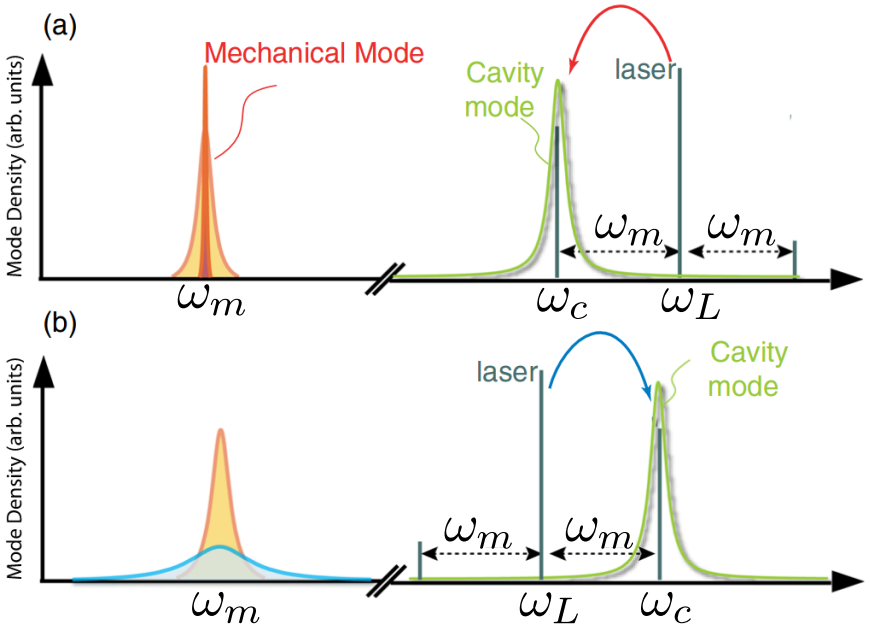

FIGURE 1.9: Scattering picture of amplification and cooling of the mechanical oscillator. (a) For $\Delta > 0$, photons scatter to a lower energy sideband, therefore adding energy to the mechanical oscillator. (b) For $\Delta < 0$, photons scatter to a higher energy sideband, therefore cooling the mechanical oscillator. Figure is taken from Ref. [8].

states. For a blue-detuned laser, $\Delta > 0$, photons will scatter to the lower-in-energy sideband in greater numbers than to the higher-in-energy sideband, as schematically shown in Fig. 1.9 (a). From energy conservation considerations, we understand that this process will add energy to the mechanical oscillator. For a red-detuned laser, $\Delta < 0$, the opposite will occur, and energy will be extracted from the mechanical oscillator, as seen in Fig. 1.9 (b).

To understand the rise of self-oscillations, we shall discuss now the result of $\gamma_{\text{eff}} < 0$. In such a case, the mechanical oscillator is continuously gaining energy. The linearized Hamiltonian we have used in describing the optical induced damping effect cannot predict a saturation of the growth of the mechanical oscillation amplitude. It is therefore the nonlinear nature of the optomechanical interaction Hamiltonian, Eq. (1.16), that will limit this growth. This, in essence, concludes our list of features that must be present in a self-oscillating system. There is an incoherent power source, and a nonlinear dissipative mechanism. We therefore expect the mechanical oscillator to demonstrate self-oscillations for some parameters.

The effects caused by the nonlinear optomechanical interaction, $g_0 a^\dagger a(b + b^\dagger)$, may be strengthened by increasing the number of photons in the electromagnetic cavity, $a^\dagger a$. This can be done by using a strong laser drive E_L. In such a case, the resulting nonlinear effects are considered classical, as it is basically a classical electromagnetic field interacting in a nonlinear manner with the mechanical oscillator. In the blue-detuned regime, researchers have indeed observed the optically-induced classical self-oscillations of the mechanical oscillator [20, 65, 145], and have furthermore mapped the attractor diagram of the resulting limit-cycles as a function of amplitude and detuning, both theoretically [85] and experimentally [17, 87]. The effect of the optomechanical interaction

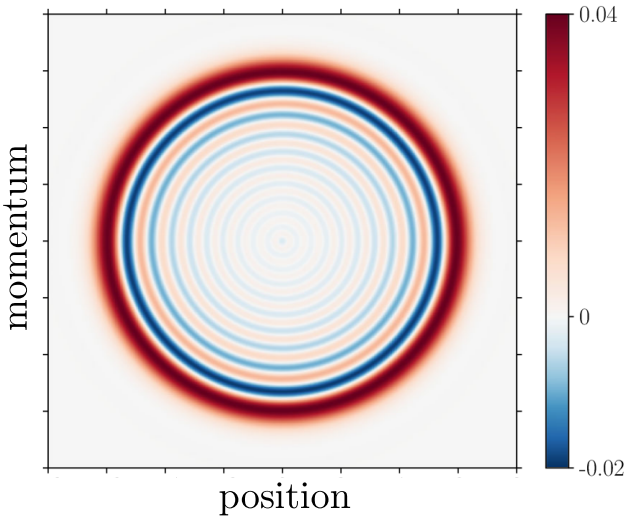

FIGURE 1.10: Wigner function representation of an optomechanical limit-cycle in the quantum regime, $g_0 = 5.5/\gamma_c$. In this interesting example, taken from Ref. [79], negative regions of the Wigner function are found, indicating a non-classical state.

may also be strengthened, alternatively, by using optomechanical systems having a large single-photon optomechanical coupling, $g_0 > \gamma_c$. This allows for nonlinear effects to be observed even in a quantum regime, in which the mechanical oscillator is influenced by a smaller number of cavity photons. In this quantum parameter regime, the limit-cycles exhibited by the mechanical oscillator were studied theoretically [79, 81]. A quite generic example of such a limit-cycle is shown in Fig. 4.2. A rather special example was provided in Ref. [79], and is shown here, Fig. 1.10. In this example, Wigner function negativity is found, indicating a quantum state (see also Sec. 1.3.2 below). In our work [3] presented in this thesis in Ch. 4, we have studied the synchronization of the mechanical self-oscillator to an additional external drive. This was done both in the classical and quantum parameter regimes.

1.2 Cooper pair splitters

Local realism is the combination of the principle of locality, by which cause-and-effect are limited to the speed of light, and the assumption of realism, which according to it a particle must have a pre-existing value for any possible measurement. Though regarded as intuitively true in classical physics, it is possible to demonstrate that quantum-entangled objects may contradict this notion, therefore having non-local correlations. A natural way to demonstrate this non-locality is by creating Einstein-Podolsky-Rosen (EPR) pairs of particles [36], which are then put to the test of the Bell inequalities [13]. Such EPR pairs had been successfully generated using photons [7], and it had become standard practice in the field of quantum optics, applied in quantum teleportation and quantum communication [14, 129]. The first device able to generate EPR electronic pairs, is the Cooper pair splitter (CPS) [52].

In a conventional s-wave superconductor, at sufficiently low temperatures, electrons near the Fermi surface become unstable against the formation of Cooper pairs. Each Cooper pair is composed of two electrons in an entangled spin-singlet state. One may then obtain a device able to generate entangled electronic pairs, by using the Cooper pairs occuring naturally in a s-wave superconductor. By coupling the superconductor to an electronic fork or Y-junction device, the two constituting electrons may emerge each in one of the two different arms of the electronic fork. This is shown in Fig. 1.11 (a), taken from Ref. [52]. The Cooper pairs, however, may also emerge in the same arm, therefore not being splitted. To avoid the latter process, one can construct the electronic fork out of two quantum dots (QDs). This is shown in Fig. 1.11 (b). If the charging energy of the QDs is very large, double occupancy cannot occur. The constituting electrons are then forced to split, or to tunnel sequentially, see Fig. 1.11 (c). By using high tunnel barriers, it is possible to strongly suppress the sequential tunneling process. Such devices are now termed CPSs, and were first theoretically proposed in Refs. [25, 75, 104], and then experimentally realized in architecutres based on InAs nanowires in Refs. [27, 51, 52], and on carbon nanotubes in Refs. [50, 113].

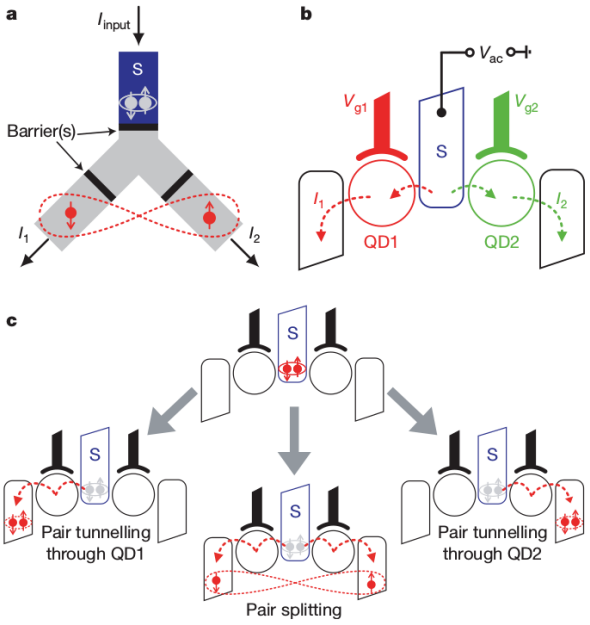

FIGURE 1.11: (a) A Cooper pair from a superconductor (blue rectangle) may split in an electronic fork, therefore providing an EPR electronic pair. (b) To suppress processes in which the Cooper pairs emerge in the same arm, the arms are made up of tunable quantum dots (QDs), with a large charging energy. (c) The Cooper pairs may still tunnel sequentially through the same arm. To strongly suppress this processes, high tunnel barriers should be used. Figure is taken from Ref. [52]

As the typical goal of using a CPS is to spatially separate the Cooper pairs, and a required intermediate step is to suppress the tunneling of a whole Cooper pair onto one QD, theoretical treatments of the CPS assume an infinite charging energy for each QD. This is known as the Coulomb blockade approximation. In our work [4], in contrast, we study the case where the charging energy is small compared with the superconducting gap. We then theoretically demonstrate the ability of the CPS to operate in that parameter regime as well, and suggest a scheme for the generation of triplet-correlated pairs of electrons.

1.3 Required basics of quantum optics

Each chapter of this thesis involved studying the dynamical time-evolution of a specific quantum system. The dynamics of the CPS system presented in Ch. 5 is unitary, and therefore the time-evolution of the system is then described by the Schrödinger equation. The vdP oscillators and the optomechanical system, which are described in Chs. 2-4, are dissipative by nature. For that reason, their dynamics is non-unitary. When describing their time-evolution, we have used the optical master equation. Detailed derivations and elaborate discussions of this master equation can be found in many textbooks, among which are Refs. [15, 19, 41, 132]. Nevertheless, we would like to present in this section

the approximations involved in obtaining the optical master equation. To do so, we shall quickly derive the master equation in Sec. 1.3.1, while highlighting the approximations taken.

Chapters 2-4 involve also the topic of phase space representations of quantum mechanics. Specifically, we have used the Wigner density function to visualize quantum states in some cases, and as a more-intuitive substitute for the density matrix in other cases. While excellent textbooks cover this topic [19, 132], we shall, for completeness' sake, introduce the Wigner density function in Sec. 1.3.2.

1.3.1 Master equation

To describe a dissipative quantum system, we start by treating the system, the environment (or bath) the system interacts with, and the interaction, using the Hamiltonian

$$H = H_S + H_B + V, \tag{1.24}$$

where H_S, H_B and V are the system Hamiltonian, bath Hamiltonian, and interaction Hamiltonian correspondingly. The time-evolution of H is unitary, and is described by the propagator $U(t) = \exp(-iH/t)$. In the interaction picture, the time-evolution of the density matrix of the whole system, ρ_T, is described via the Heisenberg equation,

$$i\dot{\rho}_T^{(I)} = \left[V^{(I)}, \rho_T^{(I)}\right], \tag{1.25}$$

where $\rho_T^{(I)} = U_0^\dagger \rho_T U_0$, $V^{(I)} = U_0^\dagger V U_0$, and $U_0 = \exp[-i(H_S+H_B)t]$. A recursive solution can be obtained via integration,

$$\rho_T^{(I)}(t) = \rho_T^{(I)}(0) - i\int_0^t \mathrm{d}t_1 \left[V^{(I)}(t_1), \rho_T^{(I)}(t_1)\right]. \tag{1.26}$$

Iterating once more, we have

$$\rho_T^{(I)}(t) = \rho_T^{(I)}(0) - i\int_0^t \mathrm{d}t_1 \left[V^{(I)}(t_1), \rho_T^{(I)}(0)\right] - \int_0^t \mathrm{d}t_1 \int_0^{t_1} \mathrm{d}t_2 \left[V^{(I)}(t_1), \left[V^{(I)}(t_2), \rho_T^{(I)}(t_2)\right]\right]. \tag{1.27}$$

We can continue and repeat the process of iteration, obtaining a series expansion in powers of the interaction potential V. Such a series expansion is known as the Born series. Assuming that V is small, we shall keep terms only up to second order in V. This is the *Born approximation*. Obtaining an equation for the dynamics of the density matrix of the system only can be done via tracing out the bath degrees of freedom.

Using $\rho^{(I)} = \mathrm{Tr}_B\left\{\rho_T^{(I)}\right\}$, we obtain from the last equation

$$\begin{aligned}\rho^{(I)}(t) = \rho^{(I)}(0) - i\int_0^t \mathrm{d}t_1 \mathrm{Tr}_B\left\{\left[V^{(I)}(t_1), \rho_T^{(I)}(0)\right]\right\} \\ - \int_0^t \mathrm{d}t_1 \int_0^{t_1} \mathrm{d}t_2 \mathrm{Tr}_B\left\{\left[V^{(I)}(t_1), \left[V^{(I)}(t_2), \rho_T^{(I)}(0)\right]\right]\right\}.\end{aligned} \tag{1.28}$$

We now assume that initially the system and the bath are uncorrelated, so that $\rho_T(0) = \rho(0) \otimes \rho_B(0)$, where ρ describes the system only, and ρ_B describes the bath only. If we now further assume that the interaction is such that $\mathrm{Tr}_B\{V(t)\rho_B\} = 0$, then the first order in V term in Eq. (1.28) is vanishing. Continuing by taking the time derivative of Eq. (1.28), we have the master equation

$$\dot{\rho}^{(I)}(t) = -\int_0^t \mathrm{d}t_1 \mathrm{Tr}_B\left\{\left[V^{(I)}(t), \left[V^{(I)}(t_1), \rho^{(I)}(t) \otimes \rho_B\right]\right]\right\}. \tag{1.29}$$

In the last equation we evaluate terms which involve taking the average with respect to the bath. In principle, this bath may retain a memory of past times for a while, and can transfer it back to the system. We shall now exclude this possibility, by assuming that the correlation time of fluctuations in the bath is much smaller than the time scale of the evolution that we want to follow. Basically, we assume the bath to have no memory of past events. This is the *first Markov approximation*. Since the two-point correlation function is significant only when $t_1 = t$, we can extend the upper integration limit appearing in the last equation to infinity. After doing so, we have finally obtained the optical master equation. To analyze the case of a harmonic dissipative oscillator, we need to consider a specific form of V. For linear damping of the harmonic oscillator, it can be assumed to be

$$V = a^\dagger \Gamma(t) e^{i\Omega t} + a\Gamma^\dagger(t) e^{-i\Omega t}, \tag{1.30}$$

where $\Gamma(t) = \sum_k g_k b_k e^{-i\omega_k t}$, a and b are the annihilation operators of the system and bath respectively, Ω is the harmonic oscillator frequency, ω_k is the frequency of the different bath modes, and g_k characterizes the coupling between the bath mode k and the harmonic oscillator. When plugging this form of interaction Hamiltonian back into Eq. (1.29), one shall encounter terms as

$$\begin{aligned}\mathrm{Tr}_B\{V(t)V(t_1)\rho_B\} &= a^\dagger a e^{i\Omega(t-t_1)}\mathrm{Tr}_B\left\{\Gamma(t)\Gamma^\dagger(t_1)\rho_B\right\} + aa^\dagger e^{-i\Omega(t-t_1)}\mathrm{Tr}_B\left\{\Gamma^\dagger(t)\Gamma(t_1)\rho_B\right\} \\ &= \sum_k g_k^2\left[a^\dagger a e^{i(\Omega-\omega_k)(t-t_1)}(n_k - 1) + aa^\dagger e^{-i(\Omega-\omega_k)(t-t_1)} n_k\right],\end{aligned} \tag{1.31}$$

where we have used $\langle b_i^\dagger b_k\rangle_B = \delta_{i,k} n_k$, where n_k is the thermal occupation number of the bath. We therefore see that we shall also encounter integrals of the form

$$\int_0^\infty \mathrm{d}t_1 e^{\pm i(\Omega-\omega_k)t_1} = \pi\delta(\Omega - \omega_k) \pm iPV\left(\frac{1}{\Omega - \omega_k}\right), \tag{1.32}$$

where PV denotes the Cauchy principal value. The Cauchy term will contribute to a small shift in the frequency of the oscillator [132], and it is therefore neglected. Using expressions as shown in Eq. (1.31), and the approximated integral result of Eq. (1.32), one can obtain from Eq. (1.29) the optical master equation for the damped harmonic oscillator,

$$\dot{\rho}^{(I)} = \gamma(n_{\rm th}+1)\left(a\rho a^\dagger - a^\dagger a\rho/2 - \rho a^\dagger a/2\right) + \gamma n_{\rm th}\left(a^\dagger \rho a - a a^\dagger \rho/2 - \rho a a^\dagger/2\right), \quad (1.33)$$

where $n_{\rm th}$ is the mean number of bath quanta at frequency Ω, and we have defined $\gamma/2 \equiv \sum_k g_k^2 \delta(\omega_k - \Omega)$. We have used exactly this form of master equation, with $n_{\rm th} = 0$, to describe the linear damping of the vdP oscillator in Chs. 2-3, and the linear dissipation of the electromagnetic cavity part of the optomechanical system in Ch. 4. In Ch. 4 we have also described the linear damping of the mechanical part of the optomechanical system using this form of Lindblad equation as well, with $n_{\rm th}$ being constant.

1.3.2 Wigner function

The Wigner density function is a quasiprobability distribution function, mapping the density matrix between real phase space functions and Hermitian operators [140]. Using the definition of the symmetrically ordered characteristic function [132],

$$\chi(\beta) = {\rm Tr}\left[D(\beta)\rho\right] = {\rm Tr}\left\{\rho e^{\beta a^\dagger - \beta^* a}\right\}, \quad (1.34)$$

where a and $a^\dagger$ are the annihilation and creation operators of photons, and $D[\beta]$ is the displacement operator of amplitude β, one can define the Wigner density function as the Fourier transform of this $\chi(\beta)$

$$W(\alpha) = \frac{1}{\pi^2}\int e^{\alpha\beta^* - \alpha^*\beta}\chi(\beta){\rm d}^2\beta. \quad (1.35)$$

The Wigner function always exists for any density matrix, but it is not always positive [41]. In order to interpret the Wigner density function as a classical probability distribution function, $W(\alpha)$ needs to be non-negative for all α. Having negativity in the Wigner density function over small regions of the phase space is therefore a signature for a quantum state. This negativity is suggested as an indicator of nonclassicality [62]. An example of an optomechanical limit-cycle with negative regions of the Wigner function is shown in Fig. 1.10.

In Chs. 2-3 we have transformed the master equation to an equivalent equation for the Wigner function. A detailed discussion of this transformation can be seen in Ref. [41] or in Ref. [132]. We would only comment, that by using an EOM for the characteristic function

$$\dot{\chi}(\beta) = {\rm Tr}\left\{D(\beta)\dot{\rho}\right\}, \quad (1.36)$$

and the Baker-Hausdorff identity, one can obtain a master equation for the characteristic function, which leads to a master equation for the Wigner density function.

CHAPTER 2

GENUINE QUANTUM SIGNATURES IN SYNCHRONIZATION OF ANHARMONIC SELF-OSCILLATORS

"Elementary, my dear Watson"

Sherlock Holmes, fictional character (was actually not said in the Conan Doyle books)

This chapter is based on our results that were published in

- Niels Lörch, Ehud Amitai, Andreas Nunnenkamp, and Christoph Bruder
  Genuine quantum signatures in synchronization of anharmonic self-oscillators
  Phys. Rev. Lett. **117**, 073601 (2016)

We study the synchronization of a van der Pol (vdP) self-oscillator with Kerr anharmonicity to an external drive. We demonstrate that the anharmonic, discrete energy spectrum of the quantum oscillator leads to multiple resonances in both phase locking and frequency entrainment not present in the corresponding classical system. Strong driving close to these resonances leads to nonclassical steady-state Wigner distributions. Experimental realizations of these genuine quantum signatures can be implemented with current technology.

2.1 Introduction

In recent years, there has been great experimental progress in studying the synchronization phenomenon with micro- and nanomechanical oscillating systems [9, 86, 119, 147, 148]. Recent advances in nanotechnology will even enable experiments with large arrays of self-oscillators in the near future [35, 109]. This progress and these advances set the scene for studying synchronization in the quantum regime [150]. Indeed, the topic of quantum synchronization has become very active [1, 3, 18, 55, 59, 71, 72, 82, 83, 134, 135, 138, 139, 142, 143, 151]. This includes theoretical proposals for studying quantum synchronization with mesoscopic ensembles of atoms [142, 143, 151], lasers [18], cavity optomechanics [3, 82, 134, 135, 138], trapped ions [55, 71, 72], micromasers [28], and arrays of coupled nonlinear cavities [59]. In addition, the dynamics of quantum synchronization are investigated [139], it was shown that using a squeezing Hamiltonian instead of a harmonic drive can produce stronger synchronization [120], and open conceptual questions regarding the relation of synchronization to entanglement [83] and to mutual information [1] are being discussed.

As discussed in Sec. 1.1.1, in the quantum regime the canonical commutation relation $[\hat{x}, \hat{p}] = i$ between the position and momentum operators, which correspond to the position and momentum observables of the self-oscillator, must be taken into account ($\hbar = 1$). For that reason, the quantum self-oscillator will always have inherent noise. The quantum vdP oscillator, being a prominent example of a quantum self-oscillator, will therefore also always have quantum noise in its description. Recent theoretical work characterized how synchronization quantitatively differs between the quantum and classical realizations of the quantum vdP oscillator in phase locking [71, 72] as well as in frequency entrainment [134, 135]. It was shown that while synchronization is hindered by quantum noise compared to the noiseless classical model [134, 135], noise is less detrimental [71, 72] than one would expect from a semiclassical description.

The aim of the work [77] described in this chapter was to find and elucidate quantum effects in the synchronization behavior of quantum vdP oscillators which are *qualitatively* different than what is expected from a corresponding semiclassical model. In this work, we studied the synchronization of a quantum vdP oscillator with Kerr anharmonicity to an external drive. This constitutes a model for self-oscillators for which *both* the damping and the frequency is amplitude-dependent. We showed that their synchronization behavior is *qualitatively* different in the quantum and the classical regimes. We have found two genuine quantum signatures. First, while synchronization of one such oscillator to an external drive is maximal at one particular frequency classically, the corresponding quantum system shows a tendency to synchronize at multiple frequencies. Using perturbation theory in the drive strength, we demonstrated that these multiple resonances reflect the quantized anharmonic energy spectrum of the oscillator. We showed that these features are observable in the phase probability distribution if the Kerr anharmonicity is large compared to the relaxation rates and the system is in the quantum regime, i.e. the limit cycle amplitudes are small. In the semiclassical limit the

energy spectrum becomes continuous, so that the resonances (and therefore the quantized energy spectrum) cannot be resolved. Using numerically exact simulations of the full quantum master equation, we found a second genuine quantum signature: for strong driving close to these resonances the steady-state Wigner distribution exhibits areas of negative density, i.e., the steady state is nonclassical.

This chapter is organized as follows. We describe the models used in this work in Sec. 2.2. This includes the quantum model, the semiclassical model (classical with Gaussian noise), and the classical noiseless model. In Sec. 2.3 the synchronization of the quantum anharmonic self-oscillator to the external drive is investigated. Phase locking and frequency entrainment are described analytically and numerically in subsections 2.3.1 and 2.3.2. A non-classical state with negative Wigner density, appearing for synchronization to a strong drive, is described in subsection 2.3.3. We conclude in Sec. 2.4.

2.2 Models

As mentioned in the previous section, we consider a self-oscillator with anharmonicity in its energy spectrum which is subject to an external drive. For concreteness, we will focus on a vdP self-oscillator with Kerr anharmonicity. Nevertheless, the results we present are generic and can be generalized to other anharmonic self-oscillators. The quantum model for a vdP oscillator which is subject to an external drive was presented in Sec. 1.1.1 and in Sec. 1.1.2. Using it, we find that in the rotating frame of the drive our model system is described by the quantum master equation

$$\dot{\rho} = -i[H_0 + H_1, \rho] + \mathcal{L}\rho, \tag{2.1}$$

with Hamiltonian $H_0 = -\Delta a^\dagger a + K(a^\dagger a)^2$, drive Hamiltonian $H_1 = iE(a - a^\dagger)$, and non-unitary term $\mathcal{L}\rho = G\mathcal{D}[a^\dagger]\rho + \kappa\mathcal{D}[a^2]\rho$, where a and $a^\dagger$ denote the annihilation and creation operators for the oscillator and the Lindblad operator $\mathcal{D}[x]\rho = x\rho x^\dagger - (x^\dagger x\rho + \rho x^\dagger x)/2$. The Hamiltonian H_0 describes a Kerr oscillator with an anharmonic energy spectrum characterized by the Kerr parameter $K > 0$, see Fig. 2.1. The coherent drive has amplitude E and frequency ω_d that is detuned from the natural harmonic frequency of the oscillator ω_m by $\Delta = \omega_d - \omega_m$. The oscillator is also subject to two incoherent processes described by the Lindblad operator D, i.e. linear (one-phonon) anti-damping with rate G and nonlinear (two-phonon) damping with rate κ.

The Hamiltonian of a Kerr anharmonic quantum oscillator is diagonal in the number basis,

$$H|n\rangle = \left[\omega_m a^\dagger a + K(a^\dagger a)^2\right]|n\rangle = \omega_m n + Kn^2.$$

The level spacing between the $(n+1)$-th and n-th energy levels is therefore $\omega_m(n+1-n) + K\left[(n+1)^2 - n^2\right] = \omega_m + (2n+1)K$. Hence the level spacing in Fig. 2.1.

Semiclassical model.– The quantum master equation (2.1) can be transformed into a fully equivalent partial differential equation for the Wigner distribution function $W(\boldsymbol{\alpha}, t)$ [19, 41] (see Sec. 1.3.2), where $\boldsymbol{\alpha} = (\alpha, \alpha^*)$.

To understand how the transformation can be done in practice, we remind the reader of the operator correspondence identities which are proven in Ref. [41] Ch. 4,

$$\begin{aligned} a\rho &\leftrightarrow \left(\alpha + \frac{1}{2}\partial_{\alpha^*}\right) W(\boldsymbol{\alpha}), \\ a^\dagger\rho &\leftrightarrow \left(\alpha^* - \frac{1}{2}\partial_{\alpha}\right) W(\boldsymbol{\alpha}), \\ \rho a &\leftrightarrow \left(\alpha - \frac{1}{2}\partial_{\alpha^*}\right) W(\boldsymbol{\alpha}), \\ \rho a^\dagger &\leftrightarrow \left(\alpha^* + \frac{1}{2}\partial_{\alpha}\right) W(\boldsymbol{\alpha}). \end{aligned} \tag{2.2}$$

Using these, we show how to transform the drive term explicitly,

$$\begin{aligned} -i\left[H_1, \rho\right] &= E\left[\left(a - a^\dagger\right)\rho - \rho\left(a - a^\dagger\right)\right] \\ &\to E\left(\alpha + \frac{1}{2}\partial_{\alpha^*} - \alpha^* + \frac{1}{2}\partial_{\alpha} - \alpha + \frac{1}{2}\partial_{\alpha^*} + \alpha^* + \frac{1}{2}\partial_{\alpha}\right) W(\boldsymbol{\alpha}) \\ &= E\left(\partial_\alpha + \partial_{\alpha^*}\right) W(\boldsymbol{\alpha}). \end{aligned}$$

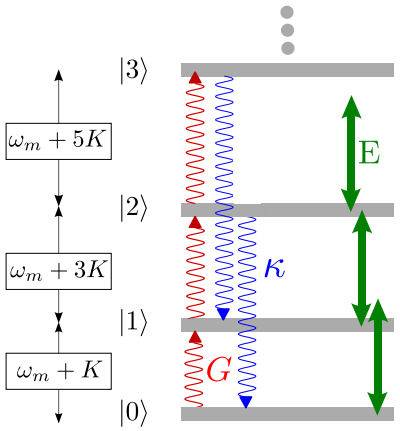

FIGURE 2.1: The first four lowest-lying energy levels of the quantum vdP self-oscillator with Kerr anharmonicity. The Kerr anharmonicity K leads to a level spacing $\omega_m + (2n+1)K$ which is increasing with excitation number n. In this figure the coherent drive (green arrows) is resonant with the transition between the states $|1\rangle$ and $|2\rangle$. The two incoherent processes (wiggly lines) are linear (one-phonon) anti-damping with rate G (red arrows) and nonlinear (two-phonon) damping with rate κ (blue arrows).

As another example, we transform the oscillator term,

$$i\Delta\left[a^\dagger a,\rho\right] \to i\Delta\left[\left(\alpha^* - \frac{1}{2}\partial_\alpha\right)\left(\alpha + \frac{1}{2}\partial_{\alpha^*}\right) - \left(\alpha - \frac{1}{2}\partial_{\alpha^*}\right)\left(\alpha^* + \frac{1}{2}\partial_\alpha\right)\right] W(\boldsymbol{\alpha})$$
$$= -i\Delta\left(\partial_\alpha\alpha - \partial_{\alpha^*}\alpha^*\right) W(\boldsymbol{\alpha}),$$

where in the last equation we have used $\partial_\alpha\alpha = \alpha\partial_\alpha + 1$. Also, please note that the order of operators in the last term reverses, since acting on ρ they operate from the right, whereas on $W(\boldsymbol{\alpha})$, they operate from the left. If needed, one additional example is provided in Sec. 3.2. Continuing in this manner, one obtains the equation of motion for the Wigner function from the master equation, Eq. (2.1).

This fully equivalent differential equation takes the form

$$\dot{W}(\boldsymbol{\alpha},t) = \Lambda W(\boldsymbol{\alpha},t) \equiv$$
$$\left\{-i\Delta\partial_\alpha\alpha + E\partial_\alpha + iK\left[\partial_\alpha\alpha(2|\alpha|^2-1) - \frac{1}{4}\partial_\alpha^2\partial_{\alpha^*}\alpha\right] + \frac{G}{2}(-\partial_\alpha\alpha + \frac{1}{2}\partial_{\alpha^*}\partial_\alpha)\right.$$
$$\left. + \frac{\kappa}{2}\left[2\partial_\alpha\alpha(|\alpha|^2-1) + \partial_{\alpha^*}\partial_\alpha(2|\alpha|^2-1) + \frac{1}{2}\partial_\alpha^2\partial_{\alpha^*}\alpha\right] + \text{h.c.}\right\} W(\boldsymbol{\alpha},t). \tag{2.3}$$

In the last equation, it is visible that both the Kerr anharmonicity K and the vdP nonlinear dissipation rate κ lead to third-order derivatives in α. These are necessary for nonclassical steady-state Wigner densities [106], and increasing the effect of these third-order derivatives may increase the 'quantumness' of the system. However, a larger rate κ is also accompanied with stronger diffusion, as is implied by the presence of the second-order derivatives which are proportional to κ. A larger Kerr term K on the other hand, gives us the opportunity to increase 'quantumness' without adding diffusion.

In the limit of large limit-cycle amplitudes $|\alpha|$, i.e. $G \gg \kappa$, we can neglect the third-order derivatives [72, 97, 132] and get

$$\Lambda_c = \partial_\alpha\left[\left(\frac{\Gamma(|\alpha|)}{2} + i\Omega(|\alpha|)\right)\alpha + E\right] + \partial_\alpha\partial_{\alpha^*}D(|\alpha|) + \text{h.c.}, \tag{2.4}$$

which contains only first- and second-order derivatives corresponding to drift and diffusion, respectively. As illustrated in Fig. 2.2, the drift term consists of an amplitude-dependent damping rate $\Gamma = -G + 2\kappa(|\alpha|^2-1)$, an amplitude-dependent oscillation frequency $\Omega = -\Delta + 2K(|\alpha|^2-1)$ in the frame of the drive, and the drive of strength E. The diffusion is given by $D = \frac{G}{4} + \frac{\kappa}{2}(2|\alpha|^2-1)$.

In the absence of driving, $E = 0$, and using radial coordinates $\alpha = Ae^{i\phi}$, the dynamics of the amplitude A decouples from the dynamics of the phase ϕ in Eq. (2.4). One can then obtain a Wigner distribution function for the amplitude only, $W(A)$. Well within a limit-cycle, we can approximate the distribution $W(A)$ as a Gaussian distribution, similar to Refs. [5, 79, 107]. The mean amplitude A_0 of this limit-cycle is determined

by imposing the condition $\Gamma(A_0) = 0$. It is then found to be $A_0 = \sqrt{1 + G/2\kappa}$. For a strongly peaked Gaussian distribution about A_0, i.e. for $G/\kappa \gg 1$, Ref. [5] describes the analytical derivation of the variance,

$$\sigma_A^2 = \frac{D(A_0)}{\frac{\mathrm{d}\Gamma}{\mathrm{d}A}\big|_{A=A_0}}. \tag{2.5}$$

We therefore obtain $\sigma_A^2 = \frac{3}{8}$, so that the relative deviation σ_A/A_0 is negligible and we can approximate the amplitude-dependent diffusion constant with its value at A_0, i.e. $D \approx (3G + 2\kappa)/4 > 0$. The oscillation frequency Ω is also sensitive to fluctuations in the amplitude A. Using an equivalent of Eq. (2.5), one finds $\sigma_\Omega \propto K A_0 \approx K\sqrt{G/2\kappa}$. Therefore, classically, the range of detuning Δ for which phase locking and frequency entrainment occur becomes larger with increasing K and A_0, as we shall see in Figs. 2.4 (b) and (f).

2.3 Synchronization

To quantify the synchronization in our quantum model, we use the synchronization measure described in Sec. 1.1.2, Eq. (1.10),

$$S = |S|e^{i\theta} = \frac{\langle a \rangle}{\sqrt{\langle a^\dagger a \rangle}} = \frac{\sum_{m=0}^{\infty} \sqrt{m+1}\rho_{m+1,m}}{\sqrt{\langle a^\dagger a \rangle}}. \tag{2.6}$$

We note that the Hamiltonian in Eq. (2.1) is time independent, as it is written in the rotating frame of the external drive. As a consequence, S is also independent of time in steady state. The mean relative phase between the external drive and the self-oscillator

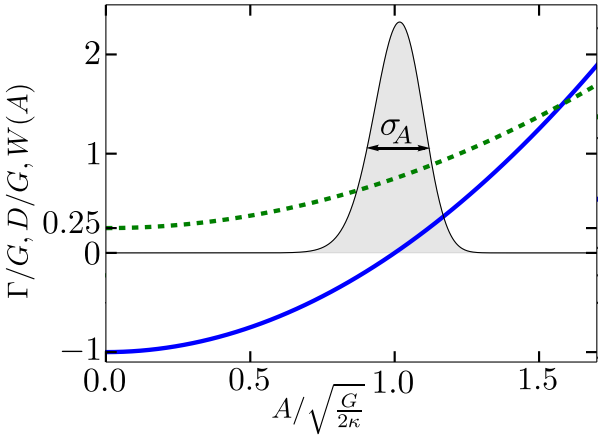

FIGURE 2.2: The amplitude-dependent damping rate Γ (blue solid line) and amplitude-dependent diffusion constant D (green dashed line) in the semiclassical equation (2.4) as a function of the amplitude A. In the limit of large amplitude A, the radial Wigner density $W(A)$ is a Gaussian with variance $\sigma_A^2 = 3/8$ around the zero of Γ, i.e. $\Gamma(A) = 0$.

is measured by θ. The exact value of this θ is not relevant for our purposes. We can therefore use $|S|$ to characterize synchronization in the system (see below and Sec. 1.1.2).

2.3.1 Analytical understanding

In order to find an analytical expression for S, we understand from Eq. (2.6) that we should calculate density matrix elements along the subdiagonal, $\rho_{m+1,m}$. These matrix elements $\rho_{m+1,m}$ in the steady state are a direct result of the external drive term in Eq. (2.1). To see it, we first note that the solution to Eq. (2.1) with $E = 0$ is derived in Ref. [32]. Representing the master equation in the number basis, and then using a generating function to replace an infinite system of difference equations by a single differential equation, Dodonov et al. are able to find the solution

$$\rho_{mm}^{(E=0)} = \frac{(G/\kappa)^m \Phi(1+n, G/\kappa+m, G/\kappa)}{(G/\kappa)_m \Phi(1, G/\kappa, 2G/\kappa)}, \tag{2.7}$$

where $(\cdot)_m$ denotes the Pochhammer symbol, and Φ is Kummer's confluent hypergeometric function. We see that $\rho^{(E=0)}$ is diagonal in the number basis and therefore it is describing limit-cycles without any preferred phase, i.e. their Wigner density is rotationally symmetric, and it depends only on the ratio of relaxation rates G/κ and not the Kerr parameter K. This is indeed expected, as in the absence of an external drive $E = 0$, we should find no synchronization, i.e. $S \propto \sum_m \rho_{m+1,m} = 0$. In the limit of large G/κ [32], corresponding to large mean amplitude, $\rho_{mm}^{(E=0)}$ follows a Gaussian distribution with mean $\langle m \rangle = G/(2\kappa)$ and variance $\sigma_m^2 = 3G/(4\kappa)$. This is consistent with the large-amplitude semiclassical treatment above, as both mean $\langle m \rangle \approx A_0^2$ and Fano factor $\sigma_m^2/\langle m \rangle \approx 4\sigma_A^2$ agree. In the opposite limit $G/\kappa \to 0$, the steady state is approximately $\rho_{mm}^{(E=0)} \to \frac{2}{3}|0\rangle\langle 0| + \frac{1}{3}|1\rangle\langle 1| + \mathcal{O}(G/\kappa)$.

The effect of the external drive E on the matrix elements $\rho_{m+1,m}$ can be analytically obtained in the limit of weak drive strength and large Kerr anharmonicity $E \ll G+\kappa \ll K$. In this limit, the perturbative approach to Markovian open quantum systems can be used [76]. In analogy to standard perturbation theory for Hamiltonians, we decompose the quantum master equation $\dot{\rho} = (\mathcal{L}_0 + \mathcal{L}_1)\rho$ in Eq. (2.1) into an unperturbed operator $\mathcal{L}_0$ and a perturbation $\mathcal{L}_1$, with

$$\begin{aligned} \mathcal{L}_0\rho &= -i[H_0, \rho] + \mathcal{L}\rho, \\ \mathcal{L}_1\rho &= -i[H_1, \rho]. \end{aligned} \tag{2.8}$$

In Ref. [76], the first order correction to the unperturbed steady state $\rho^{(E=0)}$ is found to be

$$\rho^{(1)} = -\mathcal{L}_0^{-1}\mathcal{L}_1\rho^{(E=0)}, \tag{2.9}$$

where $\mathcal{L}_0^{-1}$ is the Moore-Penrose pseudoinverse of $\mathcal{L}_0$ (see supplementary material of Ref. [76] for an explanation of the Moore-Penrose pseudoinverse). We have already found that $\rho^{(E=0)}$ is diagonal. Next, we notice that $\mathcal{L}_1$ couples only neighboring Fock states.

In order to find the first order correction to the matrix elements along the subdiagonal $\rho^{(1)}_{m+1,m}$, we are therefore only left with finding the effect of $\mathcal{L}_0^{-1}$ on the minor diagonals. Here, we exploit the fact that the superoperator $\mathcal{L}_0$ can be decomposed into terms which couple matrix elements along a specific diagonal.

To see why the superoperator $\mathcal{L}_0$ can be decomposed into terms which couple matrix elements along a specific diagonal, we represent $\dot{\rho} = \mathcal{L}_0\rho$ in the number basis,

$$\dot{\rho}_{n,m} = \left[i\Delta(n-m) - iK(n^2-m^2) - \frac{G(n+m+2)}{2} - \frac{\kappa(n^2-n+m^2-m)}{2}\right]\rho_{n,m} + G\sqrt{nm}\rho_{n-1,m-1} + \kappa\sqrt{(n+1)(n+2)(m+1)(m+2)}\rho_{n+2,m+2}. \tag{2.10}$$

Choosing $n = m$, we obtain an equation which couples only diagonal matrix elements. Choosing $n = m+1$, we obtain an equation coupling only subdiagonal matrix elements. Choosing $n = m-k$, we obtain an equation coupling matrix elements along the k-th diagonal.

We can therefore work solely in the subspace of the subdiagonal. In that subspace, and after neglecting terms of the order of G/K and κ/K, we obtain the inverse $\mathcal{L}_0^{-1}$ by inverting its diagonal so that

$$\mathcal{L}_0^{-1}\left|m+1\right\rangle\left\langle m\right| \approx \lambda^{-1}_{m+1,m}\left|m+1\right\rangle\left\langle m\right|, \tag{2.11}$$

with

$$\lambda_{m+1,m} = i\left[\Delta - K(2m+1)\right] - \frac{\Gamma_m}{2}, \tag{2.12}$$

where

$$\Gamma_m = G(2m+3) + 2\kappa m^2. \tag{2.13}$$

Choosing $n = m+1$, we can write Eq. (2.10) in the subspace of the subdiagonal

$$\dot{\rho}_{m+1,m} = \lambda_{m+1,m}\rho_{m+1,m} + G\sqrt{(m^2+m)}\rho_{m,m-1} + \kappa(m+2)\sqrt{(m+3)(m+1)}\rho_{m+3,m+2}.$$

Writing the left-hand side of this equation as a column vector, we notice that the right-hand side of this equation is just the multiplication of a square matrix with a column vector. Neglecting terms of the order of G/K and κ/G, the inverse of the square matrix is easily found by inverting its main diagonal. The result is simply Eq. (2.11).

Using the last obtained results, we finally have obtained the first order correction for the density matrix elements along the subdiagonal, Eq.(2.9),

$$\rho^{(1)}_{m+1,m} = \left(\rho^{(E=0)}_{mm} - \rho^{(E=0)}_{m+1,m+1}\right)\sqrt{m+1}\frac{E}{\lambda_{m+1,m}}\,. \tag{2.14}$$

Plugging this first-order correction into our expression for the synchronization measure, Eq. (2.6), we find

$$S(\rho^{(1)}) = \sum_{m=0}^{\infty}\left(\rho^{(E=0)}_{m,m} - \rho^{(E=0)}_{m+1,m+1}\right)\frac{m+1}{\sqrt{\langle a^\dagger a\rangle}}\frac{E}{\lambda_{m+1,m}}\,. \tag{2.15}$$

Equation (2.15) implies that $S(\rho^{(1)})$ is a coherent sum of resonances at $\Delta = K(2m+1)$ and of width Γ_m. Indeed, it is the the anharmonic discrete energy spectrum of the Kerr oscillator that leads to multiple resonances in the first-order response to an external drive. They can be resolved for large Kerr anharmonicity $K \gg \Gamma_m$. The number of visible resonances depends on the number of non-negligible probabilities $\rho^{(E=0)}_{mm}$ in the unperturbed steady state $\rho^{(E=0)}$. In the quantum limit $G/\kappa \to 0$, the resonances become more pronounced since fewer levels are occupied. In the limit $G/\kappa \to \infty$, the energy spectrum becomes continuous, so that the resonances can no longer be resolved.

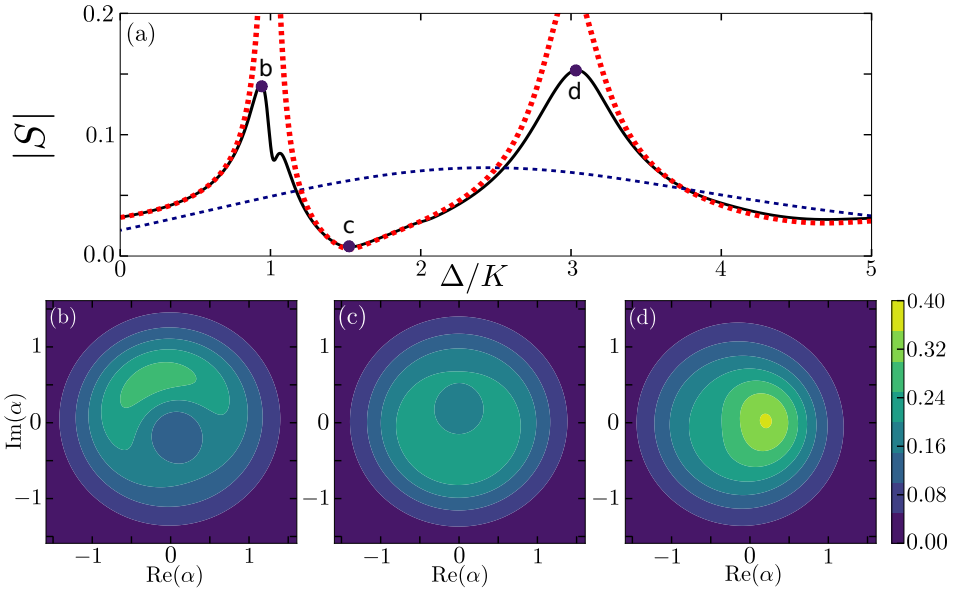

FIGURE 2.3: Synchronization measure $|S|$ and the corresponding Wigner distributions. (a) The phase locking behavior for the quantum system (black solid line) described by the master equation Eq. (2.1) or by Λ (2.3) can be understood with our perturbative expression (2.15) (red bold dotted line). For the parameters of this plot ($\kappa/G = 7$, $E/G = 2.25$, $K/G = 50$) approximately three energy levels have significant occupation, so that two resonances are possible. The blue dashed line shows the results of the corresponding semiclassical model Λ_c (2.4), for which there is only one resonance as expected. The Wigner distributions for the parameters at the two peaks (b), (d) and the minimum (c) illustrate the quantum phase locking behavior of Λ.

2.3.2 Numerical results

Now that we have obtained an analytical insight into the synchronization process of the anharmonic quantum vdP oscillator to an external drive, we are ready to present exact numerical results. The steady-state of Eq. (2.1) is obtained using the steady-state solver of `QuTiP` [60, 61]. We will compare it with the steady-state in the semiclassical approximation, i.e. the steady state of Eq. (2.4). The latter is found by discretizing the Fokker-Planck equation [106].

Figure 2.3 (a) presents the resulting phase-locking measure $|S|$ as a function of the detuning Δ, for system parameters $\kappa = 7G$, $E = 2.25G$ and $K = 50G$. The black solid line describes the quantum prediction, Eq. (2.1). We find that the position of the resonances is very well described by Eq. (2.15) (red bold dotted line). In contrast, the semiclassical model defined by Eq. (2.4) leads to a single, broad resonance (blue dashed line). Figures 2.3 (b)-(d) show how phase locking at the two maxima and the one minimum manifests in the steady-state Wigner distribution $W(\boldsymbol{\alpha})$.

Figure 2.4 presents Contour plots of the synchronization measure $|S|$ as a function of Δ and one more system parameter (κ, E,or K). Figure 2.4 (a) illustrates how more resonances at $\Delta = K(2m+1)$ appear with decreasing κ/G, as more Fock levels become populated, while each individual resonance becomes weaker. The semiclassical approximation depicted in Fig. 2.4 (b) shows only one broad smeared-out resonance, as the energy distribution is continuous classically. Figure 2.4 (c) shows the synchronization tongue, i.e. the synchronization measure as a function of detuning Δ for increasing drive

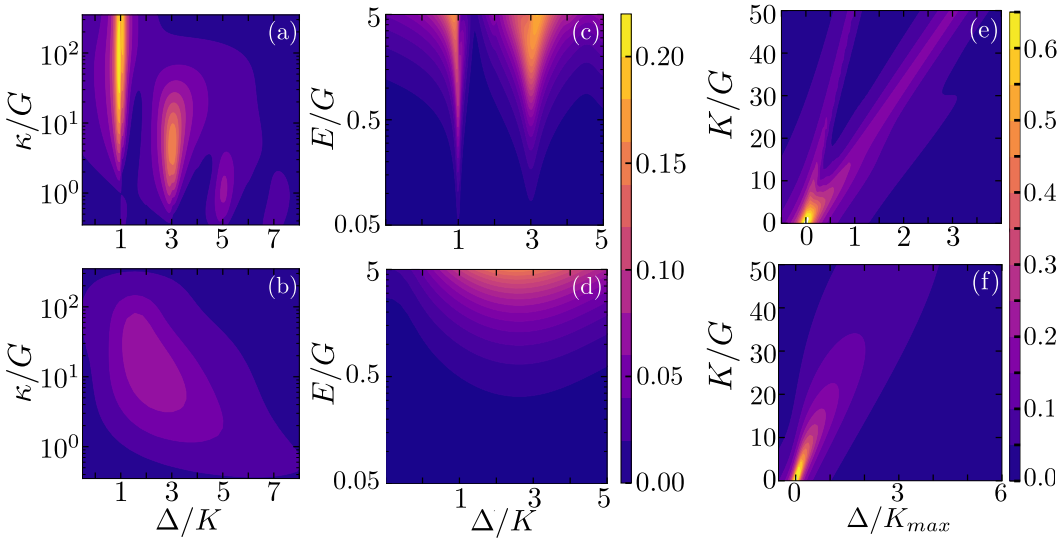

FIGURE 2.4: Behavior of the phase-locking measure $|S|$ for the steady state in the quantum description Λ (a, c, e) and in the semiclassical approximation Λ_c (b, d, f). In (a) and (b) $|S|$ is plotted as a function of Δ and κ for $E = 2.25G$ and $K = 50G$. In (c) and (d) it is plotted as a function of Δ and E for $\kappa = 5G$ and $K = 50G$. In (e) and (f) it is plotted as a function of Δ and K for $\kappa = 5G$, $E = 2.25G$, and $K_{\max} = 50G$.

E. The ratio κ/G is chosen such that three Fock levels have a non-negligible population in steady state resulting in the two resonances for the full quantum description. As expected classically, the tongue is not split in Fig. 2.4 (d), which is showing the solution for Λ_c. Finally, Figures 2.4 (e) and (f) illustrate that in the absence of a Kerr anharmonicity, $K = 0$, there is only one resonance as all energy gaps are identical for harmonic oscillators. For increasing K the resonance splits in the quantum system Fig. 2.4 (e), while the classical resonance Fig. 2.4 (f) broadens.

As discussed in Sec. 1.1.2, synchronization also results in the frequency entrainment of the natural frequency of oscillation to the frequency of the external drive. To discuss this frequency entrainment [134], we use the power spectrum,

$$P(\omega) = \int_{-\infty}^{\infty} e^{i\omega t} \langle a^\dagger(t) a(0) \rangle \mathrm{d}t. \tag{2.16}$$

Numerically simulating $P(\omega)$ using Eq. (2.1), we demonstrate in Fig. 2.5 that for a nonzero Kerr anharmonicity $K \neq 0$ the frequency entrainment shows resonances at detunings $\Delta = (2n+1)K$. These are similar to the resonances in phase locking. The maximum of the power spectrum is shown in red solid line. Indeed, the quantum signature of synchronization can be seen in both phase locking and in the frequency entrainment.

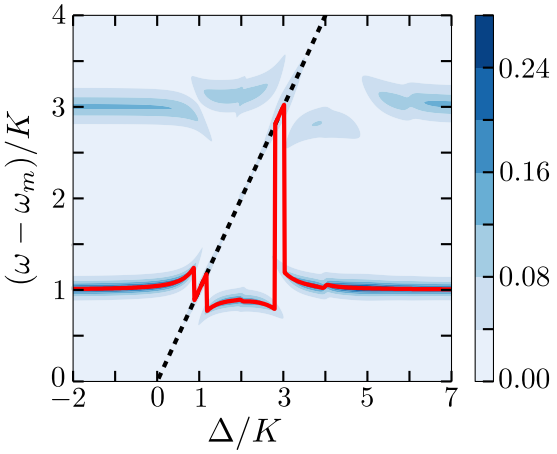

FIGURE 2.5: Power spectrum $P(\omega)$ of the quantum vdP oscillator with Kerr nonlinearity as a function of detuning Δ for $\kappa = 0.8G$, $E = 4.5G$, and $K = 25G$. The red solid line indicates the maximum of the power spectrum, the black dashed line the detuning Δ of the external drive. Around $\Delta \approx K$ and $\Delta \approx 3K$ the two lines match indicating a resonance in frequency entrainment. At $\Delta = 5K$ the spectrum shows a third, smaller response.

2.3.3 Negative Wigner density

A negative Wigner density can only be seen in nonclassical states (see Sec. 1.3.2). For the parameters of Fig. 2.5 the drive is so strong that the dynamics goes beyond first-order perturbation theory and also diagonal matrix elements of the density matrix in steady state are changed. As shown in the inset of Fig. 2.6, for the detuning at the $\Delta = 5K$ resonance the redistribution is from even to odd Fock states, which have negative Wigner density around the origin $\alpha = 0$. Accordingly, the steady-state Wigner distribution shows strong negative density as shown in Fig. 2.6. This is another quantum signature of synchronization. It clearly demonstrates that (quantum-induced) diffusion is insufficient to describe the synchronization dynamics of anharmonic oscillators, since derivatives of higher than second order are required to bring about a negative Wigner density [106] in the phase space formulation of quantum optics. Here, the higher-order derivatives stem from both the Kerr and the vdP nonlinearity, see Eq. (2.3). Interestingly though, in the case of *linear* instead of nonlinear damping, the steady-state Wigner distribution can be calculated analytically [34, 63] and it is always positive, even for $K \neq 0$. Similarly, for vdP oscillators without Kerr term, only positive-valued Wigner densities have been found [72, 134]. These observations suggest that for harmonic driving only the *combination* of a Kerr anharmonicity and a vdP nonlinearity results in a nonclassical steady state.

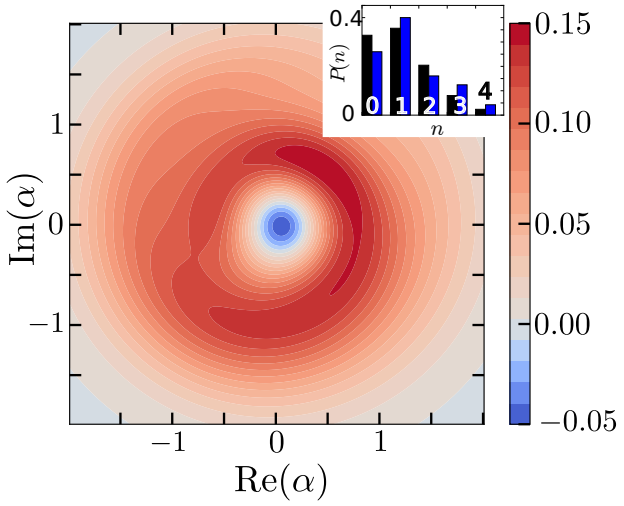

FIGURE 2.6: Steady state for the parameters of Fig. 2.5 and $\Delta = 5K$. This steady state is characterized by a Wigner distribution with negative density. The inset shows the Fock state probabilities $P(n)$ in the presence (right blue bars) and absence of the coherent external drive (left black bars).

2.4 Conclusions

In the work presented in this chapter [77], we have drawn attention to the fact that the different possible oscillation frequencies of a quantum anharmonic self-oscillator, as shown in Fig. 2.1, leads to synchronization behavior which is *qualitatively* different than the synchronization behavior which is expected from a corresponding semiclassical model. This is seen as phase locking that is resonantly enhanced and suppressed due to the quantization, as shown in Fig. 2.3 and in Fig. 2.4. This behavior can be understood with a simple analytical model leading to Eq. (2.15). We have illustrated how the number of expected synchronization resonances increase as more Fock levels become populated, while each individual resonance becomes weaker, in Fig. 2.4 (a). This quantized synchronization behavior is also seen in the power spectrum, as frequency entrainment can switch from unlocked to nearly locked behavior at the same resonances as shown in Fig. 2.5. One more clear signature of nonclassical dynamics is the negative density in the steady-state Wigner distribution displayed in Fig. 2.6, which is in contrast to similar systems [63]. Possible experimental realizations of the model described in this chapter are discussed in Sec. 1.1.1. We expect that the genuine quantum signatures discussed here will be relevant in studies of synchronization in anharmonic oscillator networks (one example for this is provided in Ref. [78]) or anharmonic oscillators coupled to other quantum systems such as qubits.

CHAPTER 3

QUANTUM EFFECTS IN AMPLITUDE DEATH OF COUPLED ANHARMONIC SELF-OSCILLATORS

"Insanity is doing the same thing over and over again, but expecting different results"

Jane Fulton, fictional character (not Albert Einstein)

This chapter is based on our results that were published in

- Ehud Amitai, Martin Koppenhöfer, Niels Lörch, Christoph Bruder
  Quantum effects in amplitude death of coupled anharmonic self-oscillators
  Phys. Rev. E **97**, 052203 (2018)

Coupling two or more self-oscillating systems may stabilize their zero-amplitude rest-state, therefore quenching their oscillation. This phenomenon is termed "amplitude death". Well-known and studied in classical self-oscillators, amplitude death was only recently investigated in quantum self-oscillators [57]. Quantitative differences between the classical and quantum descriptions were found. Here, we demonstrate that for quantum self-oscillators with anharmonicity in their energy spectrum, multiple resonances in the mean phonon number can be observed. This is a result of the discrete energy spectrum of these oscillators, and is not present in the corresponding classical model. Experiments can be realized with current technology and would demonstrate these genuine quantum effects in the amplitude death phenomenon.

3.1 Introduction

As discussed in the previous chapter, the synchronization of quantum oscillators has become a very active research topic in recent years [1, 3, 12, 28, 71, 72, 77, 78, 120, 134, 135, 138, 139, 143]. The quantum van der Pol (vdP) oscillator was proposed as a generic model for a quantum self-oscillator [72, 134], allowing for the investigation of synchronization in the quantum regime. Synchronization of a quantum vdP oscillator to a drive [72, 77, 134, 139], the synchronization of two mutually coupled vdP oscillators [1, 71, 72, 78, 135], and the synchronization of networks of such oscillators [12, 78], were theoretically investigated.

The quantum vdP oscillator model, being a generic model for a quantum self-oscillator, can be used to study other phenomena, different than quantum synchronization [57, 90]. Still, much less effort has been invested in that direction. Recently, the driven quantum vdP oscillator was used to study quantum fluctuations around arbitrary limit-cycles [90], and the quantum amplitude dynamics of two dissipatively coupled quantum vdP oscillators has also been investigated [57]. More specifically, in Ref. [57] the researchers have shown the quantum-analog of the amplitude death phenomenon (see Sec. 1.1.3). They have found quantitative differences when comparing the quantum model with a corresponding semiclassical model.

In the previous chapter, we have found genuine quantum signatures in the synchronization of an anharmonic self-oscillator to an external drive. Two main ingredients were necessary in doing so: (1) The synchronization phenomenon depends on the frequency detuning between the self-oscillator and the synchronizing drive; (2) The Kerr nonlinearity introduces different, discrete frequencies in the energy spectrum of the self-oscillator; These discrete oscillation frequencies were therefore reflected as multiple discrete resonances in the tendency of the anharmonic self-oscillator to synchronize to the external drive. The amplitude death phenomenon, as explained in Sec. 1.1.3, depends on the frequency detuning between two dissipatively-coupled self-oscillators as well. Will anharmonicity in the energy spectrum of the self-oscillators lead to quantized amplitude death? This is the subject of the work [2] presented in this chapter.

To answer our research question, we investigate the amplitude dynamics of two dissipatively coupled quantum vdP oscillators with anharmonicity in their energy spectrum. We report *qualitative* differences in the amplitude death phenomenon between the quantum model and a corresponding semiclassical model. For increasing detuning between the two self-oscillators, we observe a decay in the oscillation amplitude, as expected in amplitude death. Then however, for an even larger detuning, we observe an increase of the oscillation amplitude. We demonstrate that such an increase is the result of the quantized, anharmonic energy spectrum. It is, to the best of our knowledge, the first time that genuine quantum features that go beyond a semi-classical drift-diffusion picture are predicted to exist in the amplitude death phenomenon.

This chapter is organized as follows. We describe the models used in Sec. 3.2. This includes the quantum model, the classical (noiseless) model, and the semiclassical (contains Gaussian noise) model. Section 3.3 contains a description of the effect of the anharmonicity in the energy spectrum on the vdP oscillation amplitude. We show that this anharmonicity leads to strong oscillation-amplitude suppression, however only in the presence of noise. Genuine quantum effects in the amplitude death phenomenon, which are not the result of noise, but stemming from the quantized energy levels of the anharmonic oscillators, are described in Sec. 3.4. Our conclusions are presented in Sec. 3.5.

3.2 Models

As mentioned, the amplitude death phenomenon may occur when two self-oscillators are dissipatively-coupled. We focus on a model consisting of two anharmonic dissipatively-coupled vdP oscillators [57, 72, 135]. The results, nevertheless, are general and apply to other anharmonic self-oscillators as well. Schematics of the energy spectrum of the two quantum vdP oscillators and the non-unitary processes involved in the coupling to the environment are shown in Fig. 3.1. The quantum master equation ($\hbar = 1$) governing the

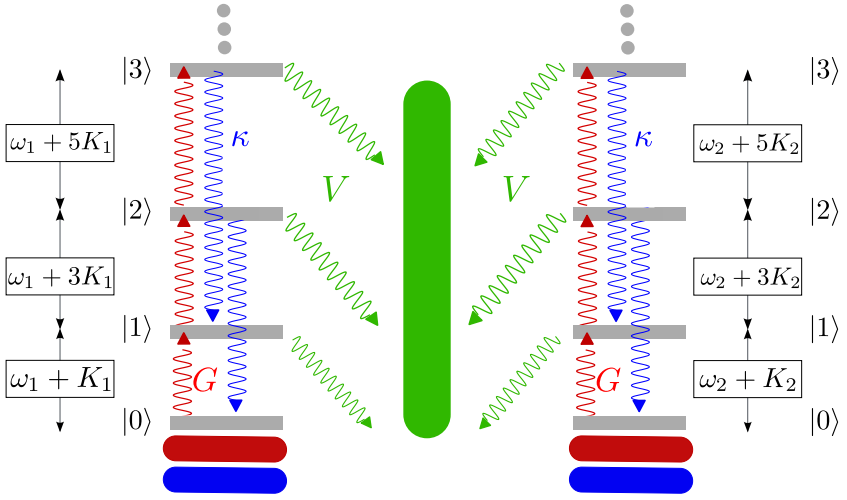

FIGURE 3.1: The four lowest-lying discrete energy levels of the quantum vdP oscillator with Kerr nonlinearity. The Kerr nonlinearity leads to an energy level spacing $\omega_m + (2n+1)K_m$ between the n-th and $(n+1)$-th energy levels (see Sec. 2.2 for explanation). The wiggly lines describe non-unitary processes stemming from coupling the system to Markovian reservoirs (marked by rectangles with rounded corners): The incoherent energy gain with rate G and the incoherent nonlinear energy loss with rate κ of the vdP oscillator are obtained by coupling the individual vdP oscillators to their own Markovian reservoirs. The dissipative coupling with strength V is obtained by coupling the vdP oscillators to a common Markovian reservoir.

time evolution of the density matrix ρ of the two oscillators was derived in Sec. 1.1.3,

$$\dot{\rho} = \sum_{m=1}^{2} \left(-i[H_m, \rho] + G\mathcal{D}[a_m^\dagger]\rho + \kappa\mathcal{D}[a_m^2]\rho \right) + V\mathcal{D}[a_1 - a_2]\rho, \tag{3.1}$$

where a_m and $a_m^\dagger$ are the annihilation and creation operators of the m-th oscillator, and $H_m = \omega_m a_m^\dagger a_m + K_m(a_m^\dagger a_m)^2$ is the Hamiltonian of the m-th Kerr vdP oscillator, with ω_m and K_m being the natural frequency and the Kerr nonlinearity parameter of the m-th oscillator, correspondingly. The non-unitary dynamics are described using Lindblad operators, $\mathcal{D}[x]\rho \equiv x\rho x^\dagger - (x^\dagger x\rho + \rho x^\dagger x)/2$. G and κ describe the rate of energy gain and the rate of nonlinear energy dissipation of the self-oscillators, respectively. V defines the strength of the dissipative coupling. Such a dissipative coupling is obtained by assuming that the two vdP oscillators are coupled to a common Markovian reservoir [89], as schematically shown in Fig. 3.1 and explained in Sec. 1.1.3. In the following, we use `QuTiP` [60, 61] to numerically simulate this master equation, which constitutes our quantum model. The explicit code is shown and explained in Appendix A.1.

In the model described by Eq. (3.1), we have chosen κ and G to be identical for both vdP oscillators. This allows us to simplify our analysis, discarding any difference between the states of the two self-oscillators which may arise as a result of their individual character. This is by no means a crucial choice for observing the noise-induced amplitude death and quantum effects described below. We have maintained the freedom of choosing a non-identical natural frequency, ω_m, as the amplitude death phenomenon depends critically on the frequency detuning between the two self-oscillator. Furthermore, we also allow for non-identical Kerr nonlinearity, K_m, as it helps to elucidate the quantum effects described in Sec. 3.4.

It is known that in the absence of a Kerr nonlinearity, the uncoupled ($V = 0$) vdP oscillators exhibit limit-cycles. We would like to emphasize that this is also true in the presence of a Kerr nonlinearity. This is apparent when examining the steady state density matrix for such a Kerr nonlinear vdP oscillator, which is given by the diagonal $\rho_{nn}^{(V=0)} = (G/\kappa)^n \Phi(1+n, G/\kappa + n, G/\kappa) / \left[(G/\kappa)_n \Phi(1, G/\kappa, 2G/\kappa)\right]$, where $(\cdot)_n$ denotes the Pochhammer symbol and Φ is Kummer's confluent hypergeometric function [32, 77]. $\rho^{(V=0)}$ depends only on G/κ and not on the Kerr parameter K_m. It therefore describes limit-cycles with no preferred phase, just as for the harmonic $K_m = 0$ case.

Classical model.– The equations describing the motion of the classical amplitudes of oscillation, $\alpha_m \equiv \langle a_m \rangle$, can be obtained from Eq. (3.1). Using the Heisenberg equation of motion (EOM) and after employing a mean-field approximation, one obtains for $m \in \{1, 2\}$

$$\dot{\alpha}_m = -i\left(\omega_m + 2K_m|\alpha_m|^2\right)\alpha_m + \frac{G}{2}\alpha_m - \kappa|\alpha_m|^2\alpha_m + \frac{V}{2}(\alpha_{\bar{m}} - \alpha_m), \tag{3.2}$$

where $\bar{m} \neq m$. These last two equations constitute our classical noiseless model. The numerical implementation of a solver for these classical coupled complex-valued differential equations is presented in appendix A.1.

To understand how the classical EOM is obtained in practice, let us take the time-derivative of $\alpha_m = \langle a_m \rangle$,

$$\begin{aligned}\frac{\mathrm{d}}{\mathrm{d}t}\alpha_m = \frac{\mathrm{d}}{\mathrm{d}t}\langle a_m \rangle = \frac{\mathrm{d}}{\mathrm{d}t}\mathrm{Tr}\left\{a_m \rho\right\} = \mathrm{Tr}\left\{a_m \frac{\mathrm{d}}{\mathrm{d}t}\rho\right\} \\ = \mathrm{Tr}\left\{a_m \left[\sum_{n=1}^{2}\left(-i[H_n,\rho] + G\mathcal{D}[a_n^\dagger]\rho + \kappa\mathcal{D}[a_n^2]\rho\right) + V\mathcal{D}[a_1 - a_2]\rho\right]\right\},\end{aligned} \tag{3.3}$$

where we have used Eq. (3.1) in the last equality. The trace over the different terms of the last equation can be straightforwardly taken. As an example, we take the trace over the energy gain term,

$$\begin{aligned}G\sum_{n=1}^{2}\mathrm{Tr}\left\{a_m \mathcal{D}[a_n^\dagger]\rho\right\} &= G\sum_{n=1}^{2}\mathrm{Tr}\left\{a_m\left(a_n^\dagger \rho a_n - \frac{1}{2}a_n a_n^\dagger \rho - \frac{1}{2}\rho a_n a_n^\dagger\right)\right\} \\ &= G\sum_{n=1}^{2}\left(\langle a_n a_m a_n^\dagger\rangle - \frac{1}{2}\langle a_m a_n a_n^\dagger\rangle - \frac{1}{2}\langle a_n a_n^\dagger a_m\rangle\right) \\ &= \frac{G}{2}\sum_{n=1}^{2}\langle a_m\rangle \delta_{m,n} = \frac{G}{2}\alpha_m.\end{aligned} \tag{3.4}$$

Continuing by taking the trace over the remaining terms of Eq. (3.1), one obtains the classical EOM, Eq. (3.2).

Semiclassical model.– To obtain from Eq. (3.1) a semiclassical model which includes Gaussian noise, we describe the system using a partial differential equation for the Wigner distribution function $W(\alpha_1, \alpha_1^*, \alpha_2, \alpha_2^*, t)$ [19, 41, 57],

$$\begin{aligned}\dot{W}(\boldsymbol{\alpha}) = \sum_{m=1}^{2}\Bigg[-\left(\frac{\partial}{\partial\alpha_m}\mu_{\alpha_m} + \text{c.c.}\right) + \frac{1}{2}\left(\frac{\partial^2}{\partial\alpha_m\partial\alpha_m^*}D_{\alpha_m\alpha_m^*} + \frac{\partial^2}{\partial\alpha_m\partial\alpha_{\bar{m}}^*}D_{\alpha_m\alpha_{\bar{m}}^*}\right) \\ + \frac{\kappa - iK_m}{4}\left(\frac{\partial^3}{\partial\alpha_m^*\partial\alpha_m^2}\alpha_m + \text{c.c.}\right)\Bigg] W(\boldsymbol{\alpha}).\end{aligned} \tag{3.5}$$

This phase space representation is completely equivalent to the master equation description, Eq. (3.1). The drift coefficients are given by

$$\mu_{\alpha_m} = \left[-i\left(\omega_m + 2K_m|\alpha_m|^2\right) + \frac{G}{2} - \kappa\left(|\alpha_m|^2 - 1\right) - \frac{V}{2}\right]\alpha_m + \frac{V}{2}\alpha_{\bar{m}}, \tag{3.6}$$

and the diffusion coefficients are given by

$$\begin{aligned} D_{\alpha_m,\alpha_m^*} &= G + 2\kappa(2|\alpha_m|^2 - 1) + V, \\ D_{\alpha_m,\alpha_{\bar{m}}^*} &= -V. \end{aligned} \tag{3.7}$$

The transformation from a master equation to a differential equation for the Wigner function is explained in Sec. 2.2. Here, we show one more example, and transform the non-unitary terms proportional to G. Using the identities given in Eq. (2.2),

$$\begin{aligned} G\sum_{m=1}^{2}\left(a_m^\dagger \rho a_m - \frac{1}{2}a_m a_m^\dagger \rho - \frac{1}{2}\rho a_m a_m^\dagger\right) \rightarrow \\ G\sum_{m=1}^{2}\Bigg[\left(\alpha_m^* - \frac{1}{2}\partial_{\alpha_m}\right)\left(\alpha_m - \frac{1}{2}\partial_{\alpha_m^*}\right) - \frac{1}{2}\left(\alpha_m + \frac{1}{2}\partial_{\alpha_m^*}\right)\left(\alpha_m^* - \frac{1}{2}\partial_{\alpha_m}\right) \\ -\frac{1}{2}\left(\alpha_m^* + \frac{1}{2}\partial_{\alpha_m}\right)\left(\alpha_m - \frac{1}{2}\partial_{\alpha_m^*}\right)\Bigg] W(\boldsymbol{\alpha}) \\ = \frac{G}{2}\sum_{m=1}^{2}\left(\partial_{\alpha_m}\partial_{\alpha_m^*} - \partial_{\alpha_m}\alpha_m - \partial_{\alpha_m^*}\alpha_m^*\right) W(\boldsymbol{\alpha}). \end{aligned}$$

Continuing in this manner, one obtains the EOM for the Wigner function from the master equation Eq. (3.1).

In the classical limit ($|\alpha_m| \gg 1$), we can neglect the third-order derivatives of Eq. (3.5) [19, 72, 97, 132]. By doing so, we obtain the Fokker-Planck equation (FPE) [106],

$$\begin{aligned} \dot{W}(\boldsymbol{\alpha}) = \sum_{m=1}^{2}\Bigg[-\left(\frac{\partial}{\partial\alpha_m}\mu_{\alpha_m} + \text{c.c.}\right) \\ +\frac{1}{2}\left(\frac{\partial^2}{\partial\alpha_m\partial\alpha_m^*}D_{\alpha_m\alpha_m^*} + \frac{\partial^2}{\partial\alpha_m\partial\alpha_{\bar{m}}^*}D_{\alpha_m\alpha_{\bar{m}}^*}\right)\Bigg] W(\boldsymbol{\alpha}). \end{aligned} \tag{3.8}$$

This FPE constitutes our semiclassical model. It can be further transformed into an equivalent Langevin form [57] which can be straightforwardly numerically simulated. The exact numerical code used for the simulation is presented and discussed in appendix A.1.

For the interested reader, we now show how to obtain an equivalent Langevin equation. As is well explained in Ref. [57], we first rewrite the FPE, Eq. (3.8), in

Cartesian coordinates. Using $\alpha_m = x_m + iy_m$, we find

$$\dot{W}(\boldsymbol{X}) = \sum_{m=1}^{2}\Bigg[-\left(\frac{\partial}{\partial x_m}\mu_{x_m} + \frac{\partial}{\partial y_m}\mu_{y_m}\right) + \frac{1}{2}\left(\frac{\partial^2}{\partial x_m^2}D_{x_m x_m} + \frac{\partial^2}{\partial y_m^2}D_{y_m y_m} + \frac{\partial^2}{\partial x_m \partial x_{\bar{m}}}D_{x_m x_{\bar{m}}} + \frac{\partial^2}{\partial y_m \partial y_{\bar{m}}}D_{y_m y_{\bar{m}}}\right)\Bigg] W(\boldsymbol{X}), \tag{3.9}$$

where $\boldsymbol{X} = (x_1, y_1, x_2, y_2)$, the drift vector $\boldsymbol{\mu} = (\mu_{x_1}, \mu_{y_1}, \mu_{x_2}, \mu_{y_2})$ is given by

$$\begin{aligned}\mu_{x_m} &= \left[\omega_m + 2K_m(x_m^2 + y_m^2)\right] y_m \\ &\quad + \left[\frac{G}{2} - \kappa(x_m^2 + y_m^2 - 1) - \frac{V}{2}\right] x_m + \frac{V}{2}x_{\bar{m}},\end{aligned}$$

$$\begin{aligned}\mu_{y_m} &= -\left[\omega_m + 2K_m(x_m^2 + y_m^2)\right] x_m \\ &\quad + \left[\frac{G}{2} - \kappa(x_m^2 + y_m^2 - 1) - \frac{V}{2}\right] y_m + \frac{V}{2}y_{\bar{m}},\end{aligned}$$

and the diffusion matrix is given by

$$\boldsymbol{D} = \frac{1}{2}\begin{bmatrix} \nu_1 & 0 & -V/2 & 0 \\ 0 & \nu_1 & 0 & -V/2 \\ -V/2 & 0 & \nu_2 & 0 \\ 0 & -V/2 & 0 & \nu_2 \end{bmatrix},$$

where $\nu_m = G/2 + \kappa\left[2(x_m^2 + y_m^2) - 1\right] + V/2$.
The Langevin equation corresponding to Eq. (3.9) is

$$\mathrm{d}\boldsymbol{X} = \boldsymbol{\mu}\mathrm{d}t + \boldsymbol{\sigma}\mathrm{d}\boldsymbol{W}_t, \tag{3.10}$$

where $\mathrm{d}\boldsymbol{W}_t$ is the Wiener increment, and the noise strength is obtained via $\boldsymbol{\sigma} = \boldsymbol{U}\sqrt{\boldsymbol{D}'}\boldsymbol{U}^{-1}$, where $\boldsymbol{D}' = \boldsymbol{U}^{-1}\boldsymbol{D}\boldsymbol{U}$ is the diagonalized form of $\boldsymbol{D}$. Writing the different matrices explicitly, we note that the diagonalization of $\boldsymbol{D}$ is done using

$$\boldsymbol{U} = \begin{bmatrix} 0 & u_- & 0 & u_+ \\ u_- & 0 & u_+ & 0 \\ 0 & 1 & 0 & 1 \\ 1 & 0 & 1 & 0 \end{bmatrix},$$

where

$$u_\pm = -\frac{\nu_1 - \nu_2 \pm \sqrt{(\nu_1 - \nu_2)^2 + V^2}}{V}.$$

The diagonalized matrix is then

$$\boldsymbol{D'} = \boldsymbol{U}^{-1}\boldsymbol{D}\boldsymbol{U} = \begin{bmatrix} \lambda_- & 0 & 0 & 0 \\ 0 & \lambda_- & 0 & 0 \\ 0 & 0 & \lambda_+ & 0 \\ 0 & 0 & 0 & \lambda_+ \end{bmatrix},$$

where $\lambda_\pm = (\nu_1 + \nu_2 \pm \sqrt{(\nu_1 - \nu_2)^2 + V^2})/4$. Finally, the noise matrix is given by

$$\begin{aligned} \boldsymbol{\sigma} &= \boldsymbol{U}\sqrt{\boldsymbol{D}}\boldsymbol{U}^{-1} \\ &= \frac{\sqrt{\lambda_+}}{u_+ - u_-} \begin{bmatrix} u_+ - u_-\sqrt{\frac{\lambda_-}{\lambda_+}} & 0 & 1 - \sqrt{\frac{\lambda_-}{\lambda_+}} & 0 \\ 0 & u_+ - u_-\sqrt{\frac{\lambda_-}{\lambda_+}} & 0 & 1 - \sqrt{\frac{\lambda_-}{\lambda_+}} \\ 1 - \sqrt{\frac{\lambda_-}{\lambda_+}} & 0 & u_+\sqrt{\frac{\lambda_-}{\lambda_+}} - u_- & 0 \\ 0 & 1 - \sqrt{\frac{\lambda_-}{\lambda_+}} & 0 & u_+\sqrt{\frac{\lambda_-}{\lambda_+}} - u_- \end{bmatrix}. \end{aligned}$$

3.3 Noise-induced amplitude death

The rest-state of two *harmonic* self-oscillators is always unstable without a coupling between the two oscillators. When the two self-oscillators are dissipatively coupled, the rest-state may become stable, leading to strong amplitude suppression. As explained in Sec. 1.1.3, this depends on the strength of the coupling V, and on the frequency detuning between the two self-oscillators, $\Delta \equiv \omega_2 - \omega_1$. In the classical noiseless case, it is predicted that the rest-state is stable in the regime $G < V < (\Delta^2 + G^2)/(2G)$ [6]. This behavior is seen in Fig. 3.2 (a), which shows the squared amplitude $|\alpha_1|^2 = |\alpha_2|^2$. For two vdP oscillators with an *anharmonic* energy spectrum, the effective oscillation frequency of the individual oscillators, $\tilde{\omega}_m \equiv \omega_m + 2K_m|\alpha_m|^2$ (see Eq. (3.2)), depends on the amplitude of oscillation. This is a direct result of the anharmonicity in their energy spectrum, K_m. In the case that this anharmonicity is identical for both oscillators, $K_1 = K_2 = K$, the effective frequency detuning is identical to the natural frequency detuning,

$$\tilde{\Delta} = \tilde{\omega}_2 - \tilde{\omega}_1 = \omega_2 - \omega_1 + 2K(|\alpha_2|^2 - |\alpha_1|^2) = \Delta, \tag{3.11}$$

since the relation $\alpha_1 = \alpha_2$ holds in this case. We therefore expect that in the classical model, the amplitude of oscillation of the anharmonic Kerr-vdP oscillators is identical to the amplitude of oscillation of the harmonic vdP oscillators, for any specific values of V and Δ. This is indeed the case, as can be seen by comparing Fig. 3.2 (a) with Fig. 3.2 (d), in which the squared amplitude of oscillation $|\alpha_1|^2$ for $K/G = 1$ is shown.

For vdP oscillators in the presence of noise, on the other hand, the anharmonicity drastically changes the oscillation amplitude as compared with the harmonic case. This can be seen both in our semiclassical model, and in the fully quantum description. In

Fig. 3.2 (b), we numerically simulate the semiclassical model, Eq. (3.8), for $K = 0$, and show the long-time limit amplitude squared, $\overline{|\alpha_1|^2}$, which is ensemble-averaged over many independent trajectories. This $\overline{|\alpha_1|^2}$ is shown as a function of both the detuning Δ and the coupling strength V. Oscillations are sustained for small enough Δ, with slightly higher amplitudes than in the noiseless case. This oscillation amplitude is highly suppressed in the regime where amplitude death is expected. Nevertheless, the amplitude of oscillation does not vanish completely, as noise hinders the complete collapse. This agrees with Ref. [57]. In Fig. 3.2 (e), in which $\overline{|\alpha_1|^2}$ is shown for $K/G = 1$, and in contrast to the classical noiseless case, the amplitudes of oscillation are significantly changed. This can be seen by comparing Fig. 3.2 (e) to Fig. 3.2 (b). It is seen that the values of $\overline{|\alpha_1|^2}$ for $V > G$ are significantly lower for the anharmonic case, as compared with the harmonic case.

As mentioned, a similar decrease is seen also in the quantum description. In Fig. 3.2 (c) we show the mean phonon number of the first oscillator $\langle a_1^\dagger a_1 \rangle$ for the harmonic case, as a function of Δ and V. As discussed in Ref. [57], the mean phonon number significantly decreases in the regime where amplitude death is expected classically, but does not vanish

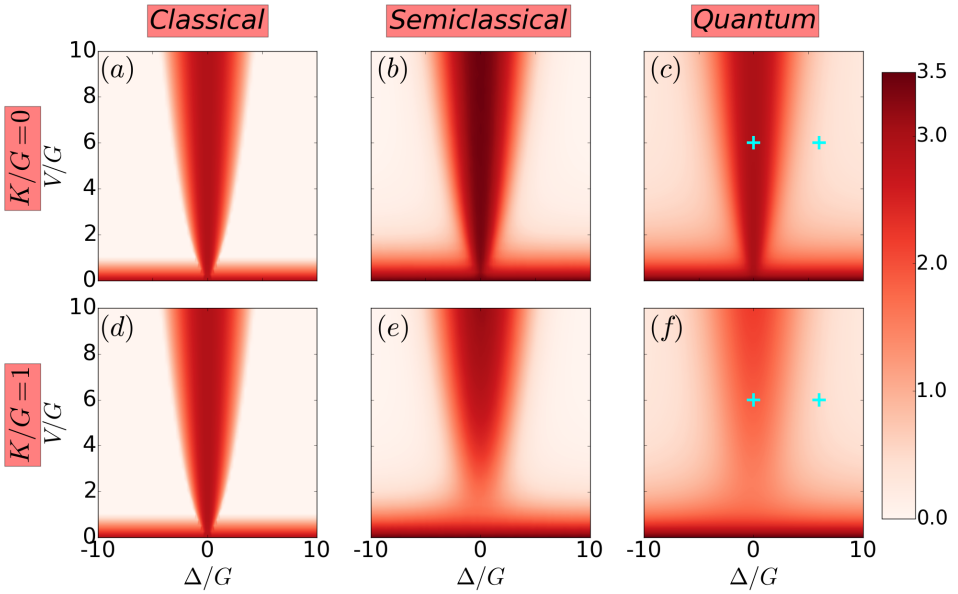

FIGURE 3.2: Amplitude suppression of two coupled self-oscillators for the harmonic and anharmonic cases in the classical, semiclassical, and quantum descriptions. (a) and (d) show the squared amplitude $|\alpha_1|^2$ of the noiseless classical oscillator obtained from Eq. (3.2). (b) and (e) present the long-time limit amplitude squared, $\overline{|\alpha_1|^2}$, obtained from numerically simulating the semiclassical model, Eq. (3.8), and then ensemble-averaging over many independent trajectories. (c) and (f) show the mean phonon number $\langle a_1^\dagger a_1 \rangle$ of the quantum oscillator, Eq. (3.1). The upper plots (a), (b), and (c) correspond to the harmonic case, $K/G = 0$. The lower plots (c), (d) and (e) correspond to the anharmonic case, with $K/G = 1$. A decrease in $\overline{|\alpha_1|^2}$ and $\langle a_1^\dagger a_1 \rangle$ is seen in the anharmonic case, as compared with the harmonic case. The energy loss rate is $\kappa/G = 0.2$ for all plots. Cyan crosses mark the parameters for which the Wigner density functions appearing in Fig. 3.3 were calculated.

completely. Noise prevents the complete collapse. This can also be seen in Fig. 3.3 (a) and Fig. 3.3 (b), in which we plot the Wigner function representation of the steady state of the oscillator before and after amplitude death occurred. The parameters chosen for these Wigner representations are marked by cyan crosses in Fig. 3.2 (c). After amplitude death takes place, the probability distribution is sharply concentrated about the origin of the axis, leading to low phonon expectation values $\langle a_1^\dagger a_1 \rangle$. When nonlinearity is introduced, just as in the semiclassical description, the mean phonon number of the oscillators is significantly changed. This is seen in Fig. 3.2 (f), in which the mean phonon number $\langle a_1^\dagger a_1 \rangle$ is shown for $K/G = 1$. As in the semiclassical description, it is seen that the values of $\langle a_1^\dagger a_1 \rangle$ for $V > G$ are significantly lower for the $K/G = 1$ case, as compared with the $K/G = 0$ case. This is also seen in the Wigner function representation, shown for the nonlinear case in Fig. 3.3 (c) and in Fig. 3.3 (d), for the parameters marked by cyan crosses in Fig. 3.2 (f). Even before amplitude death occurred, the limit-cycle of the oscillator shrank as compared with the harmonic case, Fig. 3.3 (a). The nonlinearity leads therefore to a decrease of $\langle a_1^\dagger a_1 \rangle$ in the quantum case. Note that while Fig. 3.2 and Fig. 3.3 show the average phonon number and Wigner function representation of the first oscillator, almost identical figures are obtained for the second oscillator (see Fig. 3.7 (d) and discussion in the end of Sec. 3.4).

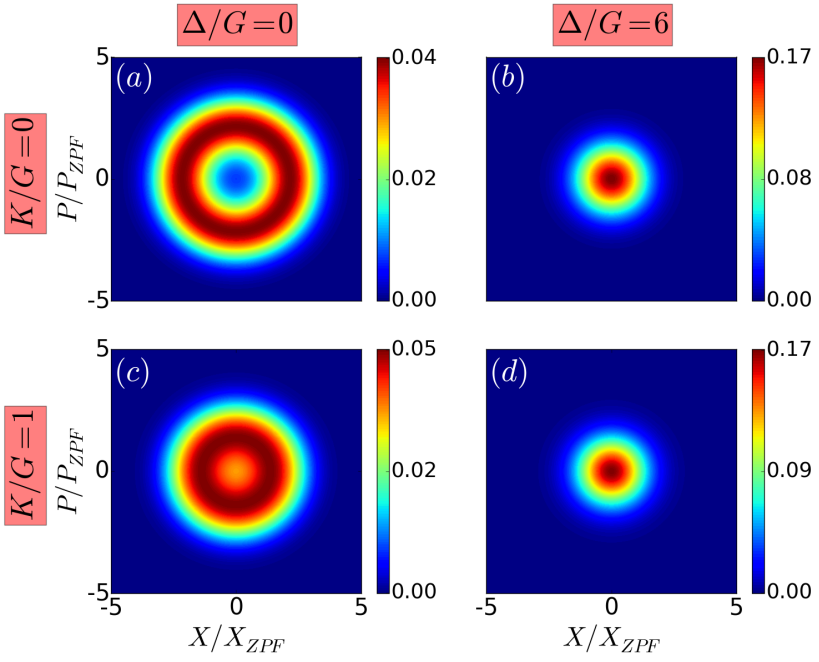

FIGURE 3.3: Wigner density function for the steady state of the oscillator before and after amplitude death occurred, for both the harmonic case and the nonlinear case. (a) and (b) correspond to the cyan crosses marked in Fig. 3.2 (c), while (c) and (d) match the cyan crosses shown in Fig. 3.2 (f). The suppression of oscillation amplitude in the presence of a Kerr nonlinearity is clearly visible by comparing (a) and (c). The limit-cycle shrinks, resulting in a decrease of $\langle a_1^\dagger a_1 \rangle$. The Wigner distributions are all rotationally symmetric, having no preferred phase. In all plots, $\kappa/G = 0.2$ and $V/G = 6$.

The underlying cause for this decrease, seen in the semiclassical model and in the quantum description, is noise. When noise is present, the amplitude of the self-oscillator fluctuates, as is implied by the existence of a diffusion constant, Eq. (3.7). The effective frequency of the oscillators with Kerr nonlinearity, $\tilde{\omega}_m$, depends on this fluctuating amplitude of oscillation. For that reason, the frequency is now a fluctuating quantity as well. The bigger the anharmonicity K is, the larger the frequency fluctuations become. This implies that when noise is present in the system, the spread of values for $\tilde{\Delta}$ is wider than the spread of values of the effective detuning for harmonic self-oscillators, Δ. Therefore, increasing K has a similar effect as increasing the effective detuning between the two self-oscillators. As the dissipative coupling is sensitive to the detuning, we see the effect of increasing K as a decrease in $\langle a_1^\dagger a_1\rangle$ ($\langle a_2^\dagger a_2\rangle$) , for $V > G$. For $V \ll G$, on the other hand, the dissipative term plays only a minor role. Therefore, increasing K does not significantly change the occupation number $\langle a_1^\dagger a_1\rangle$ ($\langle a_2^\dagger a_2\rangle$).

In Fig. 3.4 (a), we numerically simulate the quantum master equation, Eq.(3.1), and show the decrease of $\langle a_1^\dagger a_1\rangle$ for increasing K, for different coupling V values. In Fig. 3.4 (b), we numerically simulate the semiclassical model, Eq. (3.8), and show the long-time limit amplitude squared, $\overline{|\alpha_1|}$, which is ensemble averaged over many independent trajectories. Indeed, both noisy models show this decrease, and only quantitative differences can be seen when comparing the two. The noiseless classical model cannot account for this amplitude suppression. We therefore conclude that this amplitude suppression, or average occupation number reduction, is noise-induced.

For very large values of K/G, this noise-induced amplitude suppression can balance the amplitude growth induced by the linear energy gain G. This allows us to set $\kappa = 0$ for these cases, while still keeping the self-oscillators in a quantum parameter regime (see Sec. 3.4). For smaller values of K/G, a finite κ is required to keep the oscillators in a quantum parameter regime.

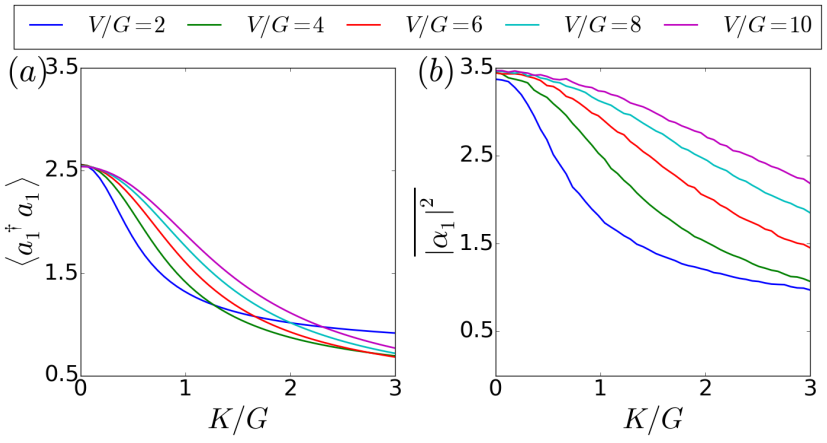

FIGURE 3.4: (a) Average occupation number, $\langle a_1^\dagger a_1\rangle$, as a function of K. (b) Average oscillation amplitude squared, $\overline{|\alpha_1|^2}$, as a function of K. In both noisy models, a noticeable decrease in the oscillation amplitude is seen for increasing K. Other parameters used in both plots are $(\kappa, \Delta) = (0.2, 0.0) \times G$.

3.4 Quantum effects – amplitude revival

In a quantum parameter regime, the anharmonicity leads to genuine quantum effects in the amplitude death phenomenon, which cannot be modeled using a classical or semiclassical model. They are the result of the quantized, discrete energy spectrum of the oscillators (see Fig. 3.1). The Kerr anharmonicity K_m leads to an energy level spacing $\omega_m + (2n+1)K_m$ between the n-th and the $(n+1)$-th Fock levels of the anharmonic quantum vdP oscillators. There are therefore several discrete frequencies relevant for each oscillator. As the amplitude death phenomenon depends on the detuning between the frequencies of the oscillators, we can expect this discreteness to be reflected in the mean phonon number $\langle a_m^\dagger a_m \rangle$ of each oscillator.

To see an example of this, consider one quantum anharmonic vdP oscillator to have a Kerr nonlinearity K_1, while the second vdP oscillator is harmonic, i.e. $K_2 = 0$. In a very quantum parameter regime, in which only the lowest three energy levels of each oscillator are populated, just three frequencies are relevant: The transition frequencies between the populated energy levels of the first oscillator, $\omega_1 + K_1$ and $\omega_1 + 3K_1$, and the transition frequency of the second oscillator, ω_2. The effective detuning between the two oscillators could therefore be minimized at two discrete values, $\tilde{\Delta} = \omega_2 - \omega_1 - K_1 = 0$ and $\tilde{\Delta} = \omega_2 - \omega_1 - 3K_1 = 0$. At these values for which the effective detuning is minimized, we

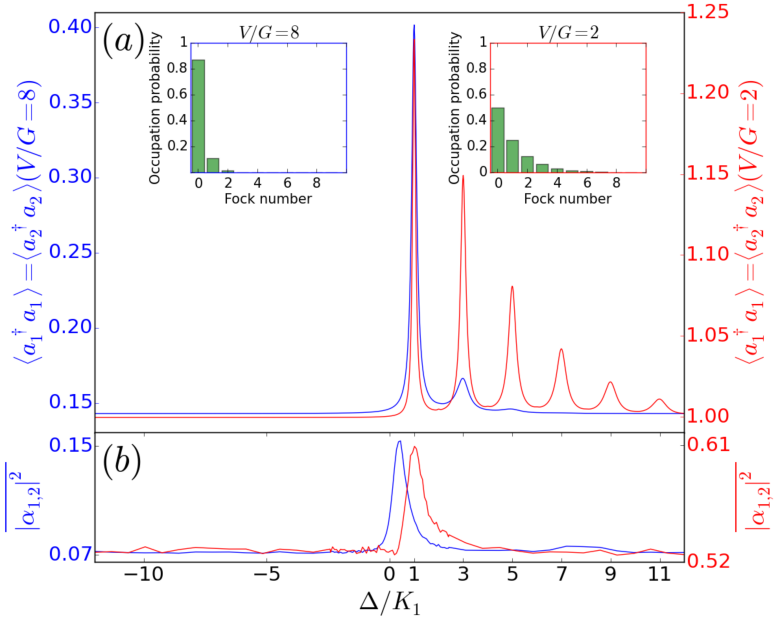

FIGURE 3.5: Average occupation number $\langle a_1^\dagger a_1 \rangle = \langle a_2^\dagger a_2 \rangle$ and average oscillation amplitude squared $\overline{|\alpha_1|^2} = \overline{|\alpha_2|^2}$ are shown as a function of the detuning in (a) and (b) for an anharmonic vdP oscillator with $K_1/G = 50$ coupled to a harmonic ($K_2/G = 0$) vdP oscillator. Blue curves correspond to $V/G = 8$, while the red curves correspond to $V/G = 2$. The Fock basis probability distributions for both these coupling strengths are shown in the insets. The individual dissipation rate is $\kappa/G = 0$.

expect to see a revival of the oscillation amplitude. In Fig. 3.5 (a), the blue curve depicts $\langle a_1^\dagger a_1\rangle = \langle a_2^\dagger a_2\rangle$ obtained by numerically simulating the master equation, Eq. (3.1), for the example just described (the Fock level probability distribution is shown in the left inset). The peaks in the mean phonon number are clearly visible. The red curve in Fig. 3.5 (a) depicts the peaks in $\langle a_1^\dagger a_1\rangle = \langle a_2^\dagger a_2\rangle$ for a smaller V, i.e. for a parameter regime in which more Fock levels are populated (see right inset). Indeed, the peaks are seen for $\Delta = (2n+1)K$, with n being a nonnegative integer. The average oscillation amplitude squared, $\overline{|\alpha_1|^2} = \overline{|\alpha_2|^2}$, predicted by the semiclassical model, is shown in Fig. 3.5 (b). Indeed, only one peak is seen in both cases, as the energy distribution is continuous in the semiclassical case. One can furthermore observe a mismatch in the peak location between the two cases. This is a classical effect, caused by the fact that the frequency of the nonlinear oscillator depends on the amplitude of oscillation, $\tilde{\omega}_1 = \omega_1 + 2K_1|\alpha_1|^2$. The peak appears for $\omega_2 = \tilde{\omega}_1$, i.e. for $\Delta = 2K_1|\alpha_1|^2$. Smaller values of V correspond to a larger amplitude of oscillation, and therefore the peak for $V/G = 2$ appears to the right of the peak for $V/G = 8$.

One can also consider the case for which both the vdP oscillators are anharmonic. An example is shown in Fig. 3.6 (a), in which the occupation number $\langle a_1^\dagger a_1\rangle = \langle a_2^\dagger a_2\rangle$ of both oscillators is plotted as a function of the detuning Δ, for equal Kerr nonlinearities $K_1 = K_2 \equiv K$. The blue curve corresponds to strong dissipative coupling V for which

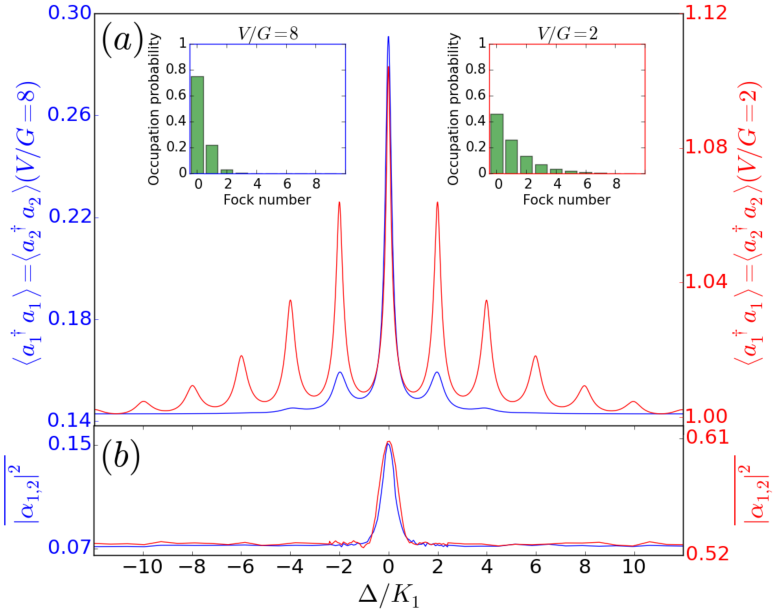

FIGURE 3.6: Average occupation number $\langle a_1^\dagger a_1\rangle = \langle a_2^\dagger a_2\rangle$ and average oscillation amplitude squared $\overline{|\alpha_1|^2} = \overline{|\alpha_2|^2}$ are shown as a function of the detuning in (a) and (b) for two coupled anharmonic ($K_1/G = K_2/G = 50$) vdP oscillators. Blue curves correspond to $V/G = 8$, while the red curves correspond to $V/G = 2$. The Fock basis probability distributions for both these coupling strengths are shown in the insets. The individual dissipation rate is $\kappa/G = 0$.

only the first three low-lying Fock levels are populated (left inset), while the red curve corresponds to smaller V, for which more Fock levels have non-negligible population (right inset). We now expect phonon number peaks for $\Delta = 2nK$, with n being an integer. These correspond to resonances between the transition frequencies of the two anharmonic oscillators, for the non-negligibly populated Fock states. The blue and red curves shown in Fig. 3.6 (b), present the single peak which is predicted by the semiclassical model. Contrary to Fig. 3.6 (b), and because both oscillators are nonlinear with $K_1 = K_2$, both peaks appear at the same detuning $\Delta = 0$.

In the previously described examples, we set $\kappa/G = 0$. The energy gain G was balanced by the dissipative coupling V. This was indeed possible because we have used large Kerr parameters K_1 or K_2, which therefore, as explained in Sec. 3.3, made the dissipative coupling more effective. For small values of K_1 and K_2, a finite value of κ needs to be introduced in order to keep the system in the quantum parameter regime.

Fig. 3.7 (a) illustrates that in the absence of Kerr anharmonicity, i.e. $K_1 = K_2 \equiv K = 0$, the two oscillators have a high phonon number only for $\Delta = 0$. As $|\Delta|$ is increased, the oscillation-amplitude is strongly suppressed. For larger values of K, the oscillation

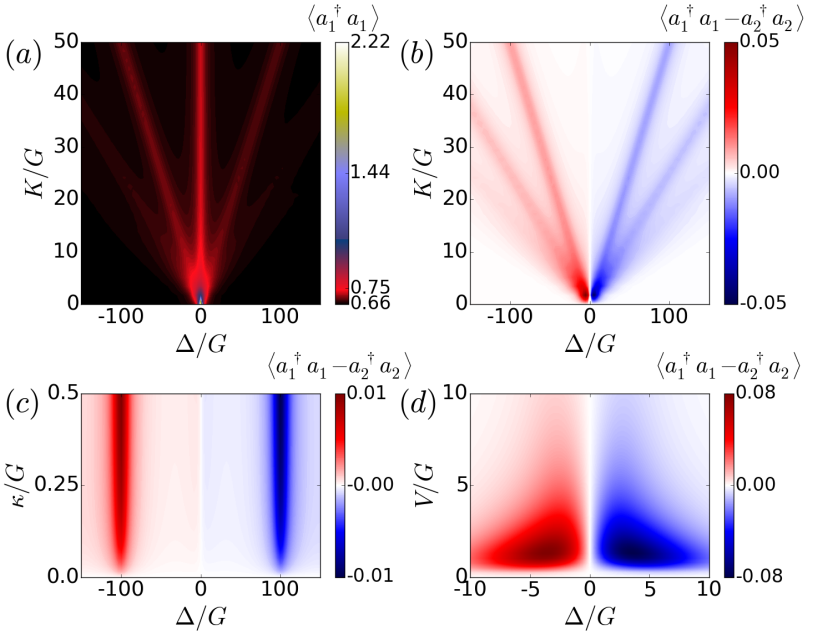

FIGURE 3.7: (a) The average occupation number $\langle a_1^\dagger a_1 \rangle$ as a function of Δ and K. Peaks in the occupation number at $K = \pm 2\Delta$ are clearly present. (b) The difference in occupation number between the two oscillators, $\langle a_1^\dagger a_1 - a_2^\dagger a_2 \rangle$. The oscillation revival is more apparent in the m-th oscillator, if it involves its lowest frequency $\omega_m + K$. Other parameters are $(\kappa, V)/G = (0.25, 2)$ in both plots. (c) The average occupation number difference, $\langle a_1^\dagger a_1 - a_2^\dagger a_2 \rangle$, as a function of Δ and κ. Other parameter are $(K, V)/G = (50, 2)$. The difference becomes more pronounced as κ is increased. (d) $\langle a_1^\dagger a_1 - a_2^\dagger a_2 \rangle$ for parameters corresponding to Fig. 3.2 (f), $(K, \kappa)/G = (1, 0.2)$.

amplitudes becomes much smaller, as the dissipative coupling is more effective. Still, for $\Delta = 0$, we have a peak in the phonon number. As we increase $|\Delta|$, the phonon number decreases. Once $|\Delta|$ gets closer to the resonance condition $|\Delta| = 2K$, the phonon number increases again.

In Fig. 3.7 (a), a dissipation rate of $\kappa/G = 0.25$ was chosen. It is needed to balance the energy gain G for the lower values of K. This value of κ introduces a small asymmetry between negative and positive detuning Δ. In Fig. 3.7 (b) the difference of the phonon number between the two oscillators, $\langle a_1^\dagger a_1 - a_2^\dagger a_2 \rangle$, is shown. We can see that for negative detunings, the phonon number peaks are more pronounced for oscillator 1. For positive detunings, the opposite is true. To understand this effect, we need to consider the frequency resonances relevant to a corresponding phonon number peak. For $\Delta > 0$ ($\Delta < 0$) and $K > 0$, the resonances involve the lowest possible transition frequency of the second (first) oscillator, with higher transition frequencies of the first (second) oscillator. As κ is influencing energy levels higher than the ground state, its effect is less detrimental on the oscillator for which the lowest possible frequency is relevant. We therefore expect that if the relations $K > 0$ and $\kappa > 0$ holds, such an asymmetry occurs. In Fig. 3.7 (c), the difference $\langle a_1^\dagger a_1 - a_2^\dagger a_2 \rangle$ is plotted as a function of the detuning Δ and of κ (other parameters are (V, K)/G=(2, 50)). It is indeed seen that $\langle a_1^\dagger a_1 - a_2^\dagger a_2 \rangle = 0$ for $\kappa = 0$. As κ is increasing, so is the difference $\langle a_1^\dagger a_1 - a_2^\dagger a_2 \rangle$. In Fig. 3.7 (d) we show the difference $\langle a_1^\dagger a_1 - a_2^\dagger a_2 \rangle$ for the parameters corresponding to Fig. 3.2 (f).

3.5 Conclusions

In the work presented in this chapter, we studied theoretically the amplitude death phenomenon for two coupled quantum vdP oscillators with Kerr anharmonicity in their energy spectrum. We have shown that the anharmonicity leads to smaller oscillation amplitudes in the quantum model, an effect which we have shown to be the result of noise. Furthermore, we have found in the quantum description *qualitative* differences as compared with the semiclassical model. Peaks in the mean phonon number of the oscillators are seen when the frequency detunings match resonances between the relevant energy transition frequencies. They describe quantized amplitude death, and then oscillation revival. As the source for these peaks is the quantized nature of the energy levels, they cannot be accounted for in a semiclassical model. To the best of our knowledge, this is the first time true quantum effects are discussed in the context of the amplitude death phenomenon. As explained in Sec. 1.1.3, a system of dissipatively-coupled quantum vdP oscillators with Kerr nonlinearities can be implemented using current technology. Realizing this experiment is therefore possible, and will demonstrate a new quantum effect in the amplitude dynamics of nonlinear coupled oscillators.

CHAPTER 4

SYNCHRONIZATION OF AN OPTOMECHANICAL SYSTEM TO AN EXTERNAL DRIVE

"Hell is other people"

Mr. Garcin, fictional character in "No Exit" (often misinterpreted)

This chapter is based on our results that were published in

- Ehud Amitai, Niels Lörch, Andreas Nunnenkamp, Stefan Walter, and Christoph Bruder
  Synchronization of an optomechanical system to an external drive
  Phys. Rev. A **95**, 053858 (2017)

Optomechanical systems driven by an effective blue detuned laser can exhibit self-sustained oscillations of the mechanical oscillator. These self-oscillations are a prerequisite for the observation of synchronization. Here, we study the synchronization of the mechanical oscillations to an external reference drive. We study two cases of reference drives: (1) An additional laser applied to the optical cavity; (2) A mechanical drive applied directly to the mechanical oscillator. Starting from a master equation description, we derive a microscopic Adler equation for both cases, valid in the classical regime in which the quantum shot noise of the mechanical self-oscillator does not play a role. Furthermore, we numerically show that, in both cases, synchronization arises also in the quantum regime. The optomechanical system is therefore a good candidate for the study of quantum synchronization.

4.1 Introduction

In this thesis so far, we have tried to illuminate genuine quantum effects in the quantum synchronization and amplitude death phenomena, which should be common to all self-oscillators with nonlinearity in their energy spectrum. We have therefore used the van der Pol (vdP) model, capturing the basic, generic characteristics of self-oscillators [10, 99]. The aim of the research presented in this chapter, however, is to deepen our understanding of synchronization in an already established, specific experimental platform, which is able to operate in a quantum parameter regime.

The topic of synchronization of self-oscillators operating in the quantum regime has attracted a considerable amount of interest in recent years [1, 12, 28, 42, 55, 71, 72, 77, 78, 82, 108, 134, 135, 138, 139, 143, 144, 151]. As mentioned previously, there has been extensive research done on the paradigmatic example of a vdP oscillator [1, 12, 71, 72, 77, 78, 134, 135, 139]. Studies of quantum synchronization in specific platforms have been conducted as well. Among these platforms are micromasers [28], atomic ensembles [108, 143], interacting quantum dipoles [151], trapped ions [55, 72], and optomechanical systems [82, 139, 144].

In an optomechanical system electromagnetic cavity modes are coupled to mechanical motion. In its most basic setup, an optomechanical system is made of a single laser-driven cavity mode which couples to a single mechanical mode via, e.g., radiation pressure [8]. The dynamics of the system crucially depends on the frequency of the laser driving the cavity. A laser field tuned to the red side of the cavity frequency is used for back-action cooling as well as for state transfer [22, 96, 125], while resonant driving is used, e.g., for position sensing [101]. When blue detuned, the laser drive can induce a parametric instability, leading in turn to self-sustained oscillations of the mechanical oscillator. For a more detailed explanation, the reader is referred to Sec. 1.1.4. These self-sustained oscillations have been studied in both the classical and the quantum regimes [5, 79, 85, 87, 102, 107]. In its self-oscillatory state, the mechanical oscillator may exhibit synchronization when coupled to an external drive (an additional external drive, in contrast to the laser driving the self-oscillations), to another optomechanical system, or as part of an array of optomechanical systems, as was theoretically shown in the classical regime [48, 53]. Synchronization of an optomechanical system to an external drive [119], of two optomechanical systems [148] and even of small arrays of up to seven such systems [147], had been demonstrated experimentally. In the quantum regime the synchronization of two optomechanical systems has been studied theoretically [139], as well as the synchronization of an array of such systems [82] within a mean-field approach.

In our work [3], presented in this chapter, we theoretically study the synchronization of the mechanical self-oscillator to an external reference drive. We examine two different reference drives: (1) An additional laser applied to the optical cavity. Under an appropriate rotating-wave approximation, this may also be implemented by modulating the power of the laser inducing the mechanical self-oscillations, as was experimentally

done in Ref. [119]; (2) A mechanical drive applied directly onto the mechanical oscillator, which could for instance be realized with a piezoelectric element attached to the mechanical oscillator.

For both cases, our starting point of the analysis is the microscopic master equation. We then use the laser theory for optomechanical limit-cycles [79] to derive an equation of motion (EOM) for the phase space distribution of the mechanical self-oscillator. We show that in both cases, in a relevant parameter regime, the Adler equation emerges from the EOM. The Adler equation is a differential equation for the phase difference between the self-oscillator and the reference drive, known to describe synchronization. For the optical reference drive, this is the first time a microscopically derived Adler equation is discussed. For the mechanical reference drive, it reproduces a result which was first shown in Ref. [48]. We then continue to show numerically, for both cases, that in the quantum parameter regime an "Arnold tongue" exists, a standard signature of synchronization [10, 99]. This suggests the optomechanical system is a good candidate for the study of synchronization in the quantum regime.

This chapter is organized as follows: We describe the system under investigation, composed of an optomechanical system and an additional reference drive in Sec. 4.2. Section 4.3 contains the analytical derivation of the microscopic Adler equations. A major part of this derivation is done by applying the laser theory for optomechanical limit-cycles [79] to this problem. In Sec. 4.4 we demonstrate numerically that synchronization is expected also in a quantum parameter regime. We conclude in Sec. 4.5.

4.2 The system

The standard Hamiltonian of an optomechanical system in which the position of the mechanical oscillator parametrically modulates the frequency of an electromagnetic cavity is given in a frame rotating with the frequency of the laser drive (see Sec. 1.1.4 for a derivation), ω_L, by [8]

$$H = \omega_m b^\dagger b - \Delta a^\dagger a - g_0 a^\dagger a \left(b + b^\dagger\right) - iE_L \left(a - a^\dagger\right), \tag{4.1}$$

where $a^\dagger$ and a are the creation and annihilation operators of photons in the cavity, $b^\dagger$ and b are the creation and annihilation operators of phonons in the mechanical resonator, ω_m is the mechanical frequency of oscillation, $\Delta = \omega_L - \omega_c$ is the detuning from cavity resonance at ω_c of the driving field with strength E_L, g_0 is the single photon coupling constant, and we have set $\hbar = 1$. A schematic figure of the system is shown in Fig. 4.1. The frame rotating with laser drive ω_L is obtained by applying the unitary transformation $\hat{U} = \exp\left(i\omega_L t a^\dagger a\right)$, which generates the Hamiltonian $\hat{U} H_{\text{old}} \hat{U}^\dagger - i\hat{U}\partial\hat{U}^\dagger/\partial t$.

The dissipation of the two oscillators (the mechanical resonator and the optical cavity) can be described via the master equation (see Sec. 1.3.1 for a quick derivation),

$$\frac{\mathrm{d}\rho}{\mathrm{d}t} = -i\left[H,\rho\right] + \mathcal{L}_m\rho + \mathcal{L}_c\rho, \tag{4.2}$$

with the Lindblad operators

$$\mathcal{L}_m\rho = \gamma_m(n_{\mathrm{th}}+1)\mathcal{D}[b]\rho + \gamma_m n_{\mathrm{th}}\mathcal{D}[b^\dagger]\rho, \tag{4.3}$$

and

$$\mathcal{L}_c\rho = \gamma_c\mathcal{D}[a]\rho, \tag{4.4}$$

where γ_m and γ_c are the amplitude damping rates of the mechanical oscillator and the electromagnetic cavity correspondingly, n_{th} is the mean phonon number in thermal equilibrium, and $D[x]\rho = x\rho x^\dagger - \left(\rho x^\dagger x + x^\dagger x\rho\right)/2$ is the standard Lindblad superoperator.

In this work we would like to study the synchronization of the mechanical element of the optomechanical system to an external drive. We consider two cases:

Case (1): Optical laser drive. – We introduce an additional optical laser reference field, with frequency ω_e^{op} given in a frame rotating with frequency ω_L, and strength E_e^{op}, by adding the term

$$H^{\mathrm{op}} = -iE_e^{op}\left(e^{i\omega_e^{op}t}a - e^{-i\omega_e^{op}t}a^\dagger\right) \tag{4.5}$$

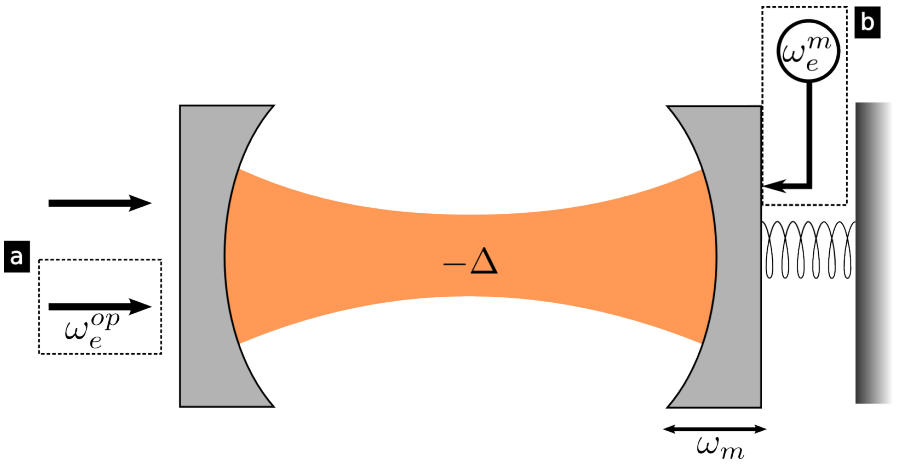

FIGURE 4.1: Schematics of a generic optomechanical system. In a rotating frame with frequency ω_L, obtained by applying the unitary transformation $\hat{U} = \exp\left(i\omega_L t a^\dagger a\right)$, the cavity with frequency $-\Delta$ is driven by a time-independent laser, depicted by the black arrow to the left of the cavity. In the self-oscillatory regime of the mechanical oscillator with natural frequency ω_m, the mechanical oscillator may synchronize to an additional optical drive with frequency ω_e^{op} as depicted in dashed box (a), or to a mechanical drive with frequency ω_e^m as depicted in dashed box (b). Note that ω_e^{op} is given in the rotating frame, while the application of $\hat{U}$ leaves both ω_e^m and ω_m identical in both frames.

to the Hamiltonian appearing in Eq. (4.2). This is depicted in dashed box (a) in Fig. 4.1. This Hamiltonian can be realized by an additional optical laser, or, if the mechanical frequency ω_m is large enough such that a rotating-wave approximation can be used, by periodically modulating the power of the optical laser causing the mechanical self-oscillations, as seen in Ref. [119].

Case (2): Mechanical drive. – A mechanical reference drive with frequency ω_e^m and strength E_e^m can be applied directly onto the mechanical oscillator, e.g., by introducing a piezoelectric component as depicted in dashed box (b) in Fig. 4.1. In analogy to case (1), we add the term

$$H^{\mathrm{m}} = -iE_e^m \left(e^{i\omega_e^m t} b - e^{-i\omega_e^m t} b^\dagger \right) \tag{4.6}$$

to the Hamiltonian appearing in Eq. (4.2).

Self-oscillations in the optomechanical system.- An optomechanical system driven by an effective blue-detuned laser may give rise to self-sustained oscillations in the mechanical oscillator (an explanation is provided in Sec. 1.1.4) [5, 79, 85, 87, 102, 107]. These self-oscillations are a prerequisite for studying synchronization, as is discussed in Sec. 1.1. They can be illustrated in phase space via the Wigner function phase space distribution. A Wigner function representation for a specific self-sustained oscillation in the mechanical oscillator is shown in Fig. 4.2 (a).

Under the influence of a reference drive, the mechanical self-oscillator may develop a phase-preference as it tends towards locking onto the phase of the drive. For an additional optical laser drive, as in case (1), the Wigner representation for a mechanical

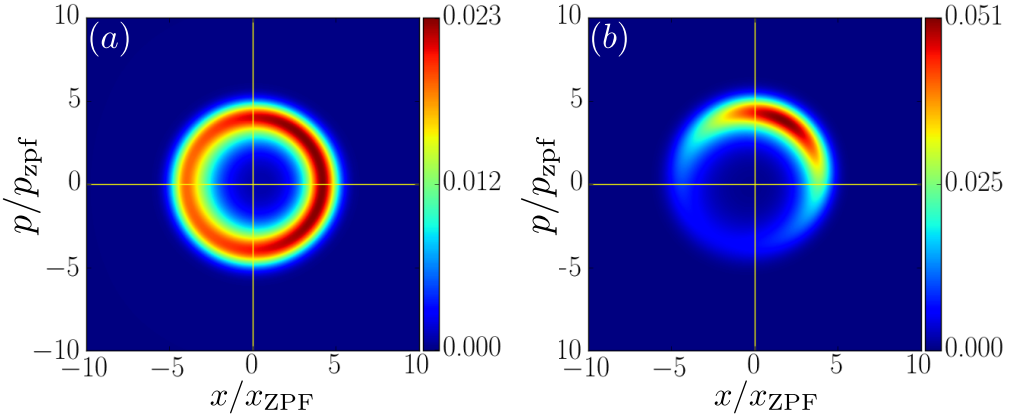

FIGURE 4.2: Wigner function representation of (a) self-sustained oscillations in the mechanical oscillator and of (b) tendency towards phase-locking of the mechanical oscillator to the phase of a synchronizing reference drive. The parameters used for both plots are $(g_0, \gamma_c, \gamma_m, E_L, \Delta, n_{\mathrm{th}}) = (0.3, 0.3, 0.015, 0.4, 0, 0) \times \omega_m$, where the parameters of the external optical drive in (b) are $(E_e^{op}, \omega_e^{op}) = (0.08, 0.98) \times \omega_m$.

self-oscillator showing such phase-preference is shown in Fig. 4.2 (b)[1].

4.3 Classical Synchronization: Analytical approach

In the following section, it is our goal to derive an analytical description for the synchronization of the mechanical self-oscillator to a reference drive, in a classical parameter regime. To do so, we apply the laser theory for optomechanical limit-cycles [79] to the current problem, Eq. (4.2), in which an additional reference drive, Eq. (4.5) or Eq. (4.6), is influencing the optomechanical limit-cycle. This approach is based on the assumption that the dynamics of the cavity adiabatically follows the dynamics of the mechanical oscillator. It allows us to obtain an EOM for the phase space distribution of the self-oscillator, $F(r,\phi)$, where r and ϕ are the mechanical phase space variables representing the radius and the phase of the self-oscillator. This derivation of the EOM is rather lengthy[2], and it is brought in the following two subsections. In Sec. 4.3.1 we derive the EOM for the mechanical self-oscillator where an additional optical reference drive is present. Section 4.3.2 relays on the previous section, and describes the case in which an additional mechanical drive is present. The fact that these equations actually describe synchronization is shown in Sec. 4.3.3.

4.3.1 Derivation of EOM – optical laser drive

The master equation describing the standard driven optomechanical system with an additional optical drive is given in Eq. (4.2), together with Eq. (4.5). It can also be written as

$$\dot{\rho} = \left(\mathcal{L}_m + \mathcal{L}_c + \mathcal{L}_{\rm int}\right)\rho, \tag{4.7}$$

where

$$\mathcal{L}_m\rho = -i[\omega_m b^\dagger b, \rho] + \gamma_m\left(n_{\rm th}+1\right)D[b]\rho + \gamma_m n_{\rm th} D[b^\dagger]\rho, \tag{4.8}$$

$$\mathcal{L}_c\rho = -i\left[-\Delta a^\dagger a - i\left(E(t)a - E^*(t)a^\dagger\right), \rho\right] + \gamma_c D[a]\rho, \tag{4.9}$$

$$\mathcal{L}_{\rm int}\rho = -i\left[-g_0 a^\dagger a(b+b^\dagger), \rho\right], \tag{4.10}$$

where we have defined $E(t) = E_L + E_e^{op} e^{i\omega_e^{op} t}$. Now we shall use the Haake-Lewenstein laser theory ansatz [47]. This will allow us to use a different adiabatic reference state of the cavity field for each point in the phase space of the mechanical oscillator. It is done

[1] The influence of the reference drive, ideally, should not change the amplitude of the self-oscillator. In practice however, there is some influence. In this work we make sure that the reference drive does not change the amplitude of the unsynchronized limit-cycle by more than 10%

[2] A shorter version of the derivation, not able to account for diffusion of the self-oscillator, but sufficient to understand synchronization, is shown in our work [3]. We choose to show here the full derivation, in order to be of help for future researchers interested in the noise properties of the mechanical self-oscillator.

by switching to a phase space representation for the mechanical degree of freedom, and then transferring the parametric dependence on the mechanical state from the cavity detuning to the drive field.

Haake-Lewenstein laser theory ansatz

The density matrix appearing in the master equation, Eq. (4.7), is describing both the electromagnetic cavity and the mechanical self-oscillator. We would like to transform it into a fully equivalent equation for $\chi(\beta,\beta^*)$, which is a density operator for the cavity field and a quasi-probability distribution for the mechanical oscillator. Formally it is done by using the correspondence rules [41]

$$b\rho \to (\beta + q\partial_{\beta^*})\chi(\beta,\beta^*), \tag{4.11}$$
$$b^\dagger\rho \to (\beta^* - p\partial_{\beta})\chi(\beta,\beta^*), \tag{4.12}$$

where $p \in [0,1]$ and $q = 1-p$. These rules corresponds to the Glauber-Sudarshan P distribution for $p=1$, to the Wigner representation for $p=1/2$, and to the Husimi Q representation for $p=0$. The translated EOM is then

$$\dot{\chi}(\beta,\beta^*,t) = (\mathcal{L}_m + \mathcal{L}_c + \mathcal{L}_{\rm int})\,\chi(\beta,\beta^*,t), \tag{4.13}$$

with

$$\mathcal{L}_m\chi = \left(\frac{\gamma_m}{2} + i\omega_m\right)(\partial_\beta\beta + \partial_{\beta^*}\beta^*)\,\chi + \gamma_m\left(n_{\rm th} + q^2 + pq\right)\partial^2_{\beta^*\beta}\chi, \tag{4.14}$$
$$\mathcal{L}_c\chi = \left[i\left(\Delta + 2g_0\,{\rm Re}(\beta)\right)a^\dagger a - \left(E(t)a - E^*(t)a^\dagger\right),\chi\right] + \gamma_c D[a]\chi, \tag{4.15}$$
$$\mathcal{L}_{\rm int}\chi = -ig_0\left[(q\partial_\beta - p\partial_{\beta^*})\,\chi a^\dagger a - (q\partial_{\beta^*} - p\partial_\beta)\,a^\dagger a\chi\right]. \tag{4.16}$$

We notice that the cavity detuning depends parametrically on the state of the mechanical oscillator. We would like to transform that dependence from the cavity detuning, to the driving field $E(t)$. This can be done using the semipolaron transformation,

$$\tilde{\chi}(\beta,\beta^*,t) = e^{i\theta(\beta,\beta^*)a^\dagger a}\chi(\beta,\beta^*,t)e^{-i\theta(\beta,\beta^*)a^\dagger a}, \tag{4.17}$$

with

$$\theta(\beta,\beta^*) = \eta\,{\rm Im}(\beta), \qquad \eta = \frac{2g_0}{\omega_m}. \tag{4.18}$$

After switching to a frame rotating with the mechanical frequency ω_m, the Liouvillians appearing in Eq. (4.13) take the form

$$\mathcal{L}_m\chi = \frac{\gamma_m}{2}(\partial_\beta\beta + \partial_{\beta^*}\beta^*)\,\chi + \gamma_m\left(n_{\rm th} + q^2 + pq\right)\partial^2_{\beta^*\beta}\chi, \tag{4.19}$$
$$\mathcal{L}_c\chi = i\left[\Delta a^\dagger a + K(a^\dagger a)^2 + i\left(\tilde{E}(t)a - \tilde{E}^*(t)a^\dagger\right),\chi\right] + \gamma_c D[a]\chi, \tag{4.20}$$
$$\mathcal{L}_{\rm int}\chi = -ig_0\left[\left(e^{i\omega_m t}q\partial_\beta - e^{-i\omega_m t}p\partial_{\beta^*}\right)\chi a^\dagger a - \left(e^{-i\omega_m t}q\partial_{\beta^*} - e^{i\omega_m t}p\partial_\beta\right)a^\dagger a\chi\right], \tag{4.21}$$

where the Kerr nonlinearity is $K = g_0^2/\omega_m$, and the driving field now contains a parametric dependence with respect to the mechanical phase space,

$$\tilde{E}(t) = \left(E_L + E_e^{op} e^{i\omega_e^{op} t}\right) e^{i\theta(\beta,\beta^*,t)} = \left(E_L + E_e^{op} e^{i\omega_e^{op} t}\right) \sum_{n=-\infty}^{\infty} J_n(-\eta r) e^{in(\omega_m t - \phi)}, \tag{4.22}$$

where we have written $\beta = re^{i\phi}$ using the radius r and the phase ϕ, and J_n are the Bessel functions of the first kind of the n'th order. We will use the shorthand notation $J_n := J_n(-\eta r)$.

Cavity reference state

Eventually, our goal is to adiabatically eliminate the cavity dynamics. This will then allow us to obtain an effective Fokker-Planck equation (FPE), describing only the motion of the mechanical mirror. We therefore assume that the cavity dynamics, with a dominant time scale γ_c, is fast compared with all other time scales in $\mathcal{L}_m$ and $\mathcal{L}_{\text{int}}$. Then, the cavity dynamics is dominated by $\mathcal{L}_c$, while the effect of $\mathcal{L}_{\text{int}}$ is neglected,

$$\dot{\rho}_c = \mathcal{L}_c \rho_c. \tag{4.23}$$

The equation describes a cavity with Kerr nonlinearity, which is driven by two amplitude and phase modulated fields, $\tilde{E}(t)$. The last equation can be solved for a cavity reference state that we could later use in the adiabatic elimination. As explained in more detail in Ref. [79], an approximate solution to Eq. (4.23) can be found in 2 cases: (1) For a cavity which is driven by a strong drive to a state of large mean amplitude, $|\alpha(t)| \gg 1$, or (2) for a cavity which is driven by a weak drive and stays close to its ground state, $|\alpha(t)| \ll 1$. In both these cases, we switch to a displaced frame using the operator $D(\alpha) = \exp(\alpha a^\dagger - \alpha a)$. The displacement cavity field $\alpha(t)$ is chosen such that terms in the dominant order in α are canceled from the transformed master equation. That means that in the first case, for $|\alpha(t)| \gg 1$, we choose α such that terms up to third order in α are canceled, and we neglect terms up to first order in α. In the second case, for $|\alpha(t)| \ll 1$, we choose α such that terms up to first order in α cancel, and we neglect terms of third order in α. In the displaced frame, Eq. (4.23) is transformed to

$$\begin{aligned}\dot{\rho}_c =& \gamma_c D[a]\rho_c + i\Big\{ i\left[\left(\dot{\alpha} + \left(\gamma_c/2 - i\Delta - 2iK|\alpha|^2\right)\alpha - \tilde{E}\right)a^\dagger - \text{h.c.}\right] \\ &+ \left(\Delta + 4K|\alpha|^2\right)a^\dagger a + K\left[\frac{(a^\dagger a)^2}{2} + \alpha^2 (a^\dagger)^2 + (\alpha^* a + \alpha a^\dagger) a^\dagger a + \text{h.c.}\right], \rho_c \Big\}.\end{aligned} \tag{4.24}$$

Displaced frame for $|\alpha(t)| \gg 1$.- In order to eliminate terms of third order in α in Eq. (4.24), we require that $\alpha(t)$ is the long-time solution of

$$\dot{\alpha}(t) = -\left\{\frac{\gamma_c}{2} - i\left[\Delta + 2K|\alpha(t)|^2\right]\right\}\alpha(t) + \tilde{E}(\beta, \beta^*, t). \tag{4.25}$$

As a result of the driving field $\tilde{E}$, Eq. (4.22), we expect the solution to be of the form

$$\alpha(\beta,\beta^*,t)=\sum_{n=-\infty}^{\infty}\left[\alpha_n^l(\beta,\beta^*)e^{in\omega_m t}+\alpha_n^e(\beta,\beta^*)e^{i(n\omega_m+\omega_e^{op})t}\right]. \tag{4.26}$$

Placing this form of solution into Eq. (4.25), one sees that the effective detuning experienced by the cavity will be dominantly given by the DC component of $|\alpha(t)|^2$, such that it is useful to define an effective detuning,

$$\Delta_{\text{eff}}(\beta,\beta^*)=\Delta+2K\sum_n\left[|\alpha_n^l|^2+|\alpha_n^e|^2+\alpha_n^l(\alpha_{n-1}^e)^*+(\alpha_{n+1}^l)^*\alpha_n^e\right], \tag{4.27}$$

where we have assumed $\omega_e^{op}=\omega_m+\epsilon$, where $\epsilon\ll\omega_e^{op},\omega_m$. This assumption is satisfied when studying synchronization about the $\omega_e^{op}=\omega_m^{\text{eff}}$ peak (see Fig. 4.5). If one is interested in describing the synchronization peak about another external frequency, $\omega_e^{op}=\omega_m^{\text{eff}}/2$ for example, this assumption should be adjusted (in this example the new assumption should be $\omega_e^{op}=\omega_m/2+\epsilon$). We seek an approximate solution to Eq. (4.25) by assuming a fixed effective detuning Δ_{eff}. We then find,

$$\alpha_n^l=\frac{E_L}{h_n}J_n\left(-\eta r\right)e^{-in\phi}, \tag{4.28}$$

$$\alpha_n^e=\frac{E_e^{op}}{h_{n+1}}J_n\left(-\eta r\right)e^{-in\phi}, \tag{4.29}$$

$$h_n=\frac{\gamma_c}{2}+i(n\omega_m-\Delta_{\text{eff}}), \tag{4.30}$$

where we have again used $\omega_e^{op}=\omega_m+\epsilon$. The Liouvillians describing the dynamics of the mechanical oscillator, cavity, and the interaction, are given in this rotating (with frequency ω_m), displaced (with amplitude $\alpha(t)$) frame as

$$\mathcal{L}_m\chi=\frac{\gamma_m}{2}\left[\partial_\beta\beta+(\bar{n}+q^2+pq)\partial^2_{\beta\beta^*}+\text{h.c.}\right]\chi-ig_0\left(\partial_\beta e^{i\omega_m t}-\text{h.c.}\right)|\alpha|^2\chi, \tag{4.31}$$

$$\mathcal{L}_c\chi=-i\left\{-(\Delta+4K|\alpha|^2)a^\dagger a-K[\alpha^2(a^\dagger)^2+\text{h.c.}],\chi\right\}+\gamma_c D[a]\chi, \tag{4.32}$$

$$\begin{aligned}\mathcal{L}_{\text{int}}\chi=&-ig_0\left(qe^{i\omega_m t}\partial_\beta-pe^{-i\omega_m t}\partial_{\beta^*}\right)\chi(\alpha^*a+\alpha a^\dagger)\\&+ig_0\left(qe^{-i\omega_m t}\partial_{\beta^*}-pe^{i\omega_m t}\partial_\beta\right)(\alpha^*a+\alpha a^\dagger)\chi.\end{aligned} \tag{4.33}$$

As seen by comparing Eq. (4.25) to Eq. (4.32), the Kerr nonlinearity induces a different effective detuning for the mean field α than for the fluctuations. We therefore further define the effective detuning for the fluctuations,

$$\tilde{\Delta}_{\text{eff}}(\beta,\beta^*)=\Delta+4K\sum_n\left[|\alpha_n^l|^2+|\alpha_n^e|^2+\alpha_n^l(\alpha_{n-1}^e)^*+(\alpha_{n+1}^l)^*\alpha_n^e\right]. \tag{4.34}$$

Displaced frame for $|\alpha(t)|\ll 1$.- In this limit, we restrict our analysis to the lowest two Fock states. Then, operators consisting of three creation or annihilation operators in Eq. (4.24) can be replaced with just one operator, e.g. $a^\dagger a^\dagger a\to a^\dagger$. Also, $(a^\dagger a)^2\to a^\dagger a$.

We then continue by canceling terms of first order in α. It is done by requiring that $\alpha(t)$ solves

$$\dot{\alpha}(t) = \left[i(\Delta + K) - \frac{\gamma_c}{2}\right]\alpha(t) + \tilde{E}(t). \tag{4.35}$$

In this limit, we can then see that the effective detuning is simply $\Delta_K = \Delta + K$. The Liouvillians describing the dynamics of the cavity and the interaction in this limit, and in the rotating, displaced frame are

$$\mathcal{L}_c\chi = -i\left\{-(\Delta + K)a^\dagger a - K[\alpha^2(a^\dagger)^2 + \text{h.c.}], \chi\right\} + \gamma_c D[a]\chi \tag{4.36}$$

$$\begin{aligned}\mathcal{L}_{\text{int}}\chi = &-ig_0\left(qe^{i\omega_m t}\partial_\beta - pe^{-i\omega_m t}\partial_{\beta^*}\right)\chi(\alpha^* a + \alpha a^\dagger + a^\dagger a) \\ &+ ig_0\left(qe^{-i\omega_m t}\partial_{\beta^*} - pe^{i\omega_m t}\partial_\beta\right)(\alpha^* a + \alpha a^\dagger + a^\dagger a)\chi,\end{aligned} \tag{4.37}$$

with the equation for the mechanical part $\mathcal{L}_m F$ being identical to Eq. (4.31). We see that in this limit of $|\alpha(t)| \ll 1$, and in contrast to the limit of $|\alpha(t)| \gg 1$, there is no need to distinguish between the effective detuning seen by the mean field and the effective detuning seen by the fluctuations.

By comparing the Liouvillians of the two limits, one notices the following differences: (1) The solution $\alpha(t)$ differs only by the effective detuning; (2) The cavity Liouvillians, $\mathcal{L}_c\chi$, differ only by the effective detuning for the fluctuations; (3) There are two additional terms in $\mathcal{L}_{\text{int}}\chi$ as given in Eq. (4.37) as compared with the expression given in Eq. (4.33). However, these two terms are further on neglected in the adiabatic elimination. For that reason, switching between the two limits is easily obtained via the transformation $\Delta_{\text{eff}}, \tilde{\Delta}_{\text{eff}} \leftrightarrow \Delta_K$. We can therefore continue and discuss only the results for $|\alpha(t)| \gg 1$, since the results in the opposite limit $|\alpha(t)| \ll 1$ follow in complete analogy.

Adiabatic elimination of the cavity

After obtaining the reference state for $\alpha(t)$, we can finally eliminate the cavity in second order perturbation theory. As in [79], we ignore $\mathcal{L}_m$ for now, and reinclude it later. In the optical Fock basis, we define $\chi_{ij} \equiv \langle i|\,\chi\,|j\rangle$. We would now aim for the differential equations of χ_{ij}. As the creation and annihilation operators in Eqs. (4.31)-(4.33) refer to the fluctuations, we will not allow for indices $i, j > 1$. We then find

$$\dot{\chi}_{00} = \gamma_c\chi_{11} + ig_0\left[(qe^{-i\omega_m t}\partial_{\beta^*} - pe^{i\omega_m t}\partial_\beta)\alpha^*\chi_{10} - e^{i\omega_m t}\partial_\beta|\alpha|^2\chi_{00} - \text{h.c.}\right], \tag{4.38}$$

$$\begin{aligned}\dot{\chi}_{10} = &\left(i\tilde{\Delta}_{\text{eff}} - \frac{\gamma_c}{2}\right)\chi_{10} + ig_0\left\{\left[e^{-i\omega_m t}\partial_{\beta^*} + (e^{-i\omega_m t}\partial_{\beta^*} - e^{i\omega_m t}\partial_\beta)|\alpha|^2\right]\chi_{10}\right. \\ &\left.+(qe^{-i\omega_m t}\partial_{\beta^*} - pe^{i\omega_m t}\partial_\beta)\alpha\chi_{00} - (qe^{i\omega_m t}\partial_\beta - pe^{-i\omega_m t}\partial_{\beta^*})\alpha\chi_{11}\right\},\end{aligned} \tag{4.39}$$

$$\dot{\chi}_{11} = -\gamma_c\chi_{11} + ig_0\left[(qe^{-i\omega_m t}\partial_{\beta^*} - pe^{i\omega_m t}\partial_\beta)\alpha\chi_{01} - e^{i\omega_m t}\partial_\beta\left(1 + |\alpha|^2\right)\chi_{11} - \text{h.c.}\right]. \tag{4.40}$$

We now adiabatically eliminate χ_{10} to first order in g_0. We note that χ_{11} is already of order g_0^2 and its contribution is therefore neglected, and we anticipate χ_{10} to be of order

g_0, and therefore its contribution can be neglected as well.

$$\begin{aligned}\chi_{10}(t) &= ig_0\int_0^\infty \mathrm{d}\tau e^{(i\tilde{\Delta}_{\mathrm{eff}}-\gamma_c/2)\tau}\left(qe^{-i\omega_m(t-\tau)}\partial_{\beta^*}-pe^{i\omega_m(t-\tau)}\partial_\beta\right)\alpha(t-\tau)\chi_{00}(t)\\ &= ig_0\sum_n\Bigg[q\partial_{\beta^*}e^{i(n-1)\omega_m t}\frac{\alpha_n^l}{\tilde{h}_{n-1}}-p\partial_\beta e^{i(n+1)\omega_m t}\frac{\alpha_n^l}{\tilde{h}_{n+1}}\\ &\qquad +q\partial_{\beta^*}e^{i\left[(n-1)\omega_m+\omega_e^{op}\right]t}\frac{\alpha_n^e}{\tilde{h}_{n-1}^e}-p\partial_\beta e^{i\left[(n+1)\omega_m+\omega_e^{op}\right]t}\frac{\alpha_n^e}{\tilde{h}_{n+1}^e}\Bigg]\chi_{00}(t),\end{aligned}\tag{4.41}$$

where we have used the form of $\alpha(t)$ given in Eq. (4.26), and defined $\tilde{h}_n\equiv\gamma_c/2+i(n\omega_m-\tilde{\Delta}_{\mathrm{eff}})$ and $\tilde{h}_n^e\equiv\gamma_c/2+i(n\omega_m+\omega_e^{op}-\tilde{\Delta}_{\mathrm{eff}})$.

Obtaining the FPE

Finally, we will use the differential equations for the optical Fock basis elements of $\chi(\beta,\beta^*,t)$, Eqs. (4.38)-(4.41), and obtain an EOM for the phase space distribution $F(\beta,\beta^*,t)$, i.e. a FPE. This is done by noticing that the derivative of the phase space distribution is given by $\dot{F}=\mathrm{Tr}(\dot{\chi})\approx\dot{\chi}_{00}+\dot{\chi}_{11}$, where the trace is of course taken over the optical Fock basis. Keeping only the leading order terms in g_0,

$$\dot{F}=ig_0\partial_{\beta^*}e^{-i\omega_m t}|\alpha(t)|^2\chi_{00}+ig_0\left[\partial_{\beta^*}e^{-i\omega_m t}-\partial_\beta e^{i\omega_m t}\right]\alpha^*(t)\chi_{10}+\mathrm{h.c.}.\tag{4.42}$$

Using the form of $\alpha(t)$ given in Eq. (4.26), and our expressions for χ_{00} and χ_{10} given in Eqs. (4.38) and (4.41), we find

$$\begin{aligned}\dot{F} &= \sum_n ig_0\partial_{\beta^*}\left[\alpha_n^l(\alpha_{n-1}^l)^*+\alpha_n^l(\alpha_{n-2}^e)^*e^{-i\epsilon t}+\alpha_n^e(\alpha_n^l)^*e^{i\epsilon t}\right]F\\ &-g_0^2\sum_n\Bigg\{q\partial_{\beta^*}^2\frac{\alpha_n^l(\alpha_{n-2}^l)^*}{\tilde{h}_{n-1}}-p\partial_{\beta\beta^*}^2\frac{\alpha_n^l(\alpha_n^l)^*}{\tilde{h}_{n+1}}+q\partial_{\beta^*}^2e^{i\epsilon t}\frac{\alpha_n^e(\alpha_{n-1}^l)^*}{\tilde{h}_n}\\ &-p\partial_{\beta\beta^*}^2e^{i\epsilon t}\frac{\alpha_n^e(\alpha_{n+1}^l)^*}{\tilde{h}_{n+2}}+q\partial_{\beta^*}^2e^{-i\epsilon t}\frac{\alpha_n^l(\alpha_{n-3}^e)^*}{\tilde{h}_{n-1}}-p\partial_{\beta\beta^*}^2e^{-i\epsilon t}\frac{\alpha_n^l(\alpha_{n-1}^e)^*}{\tilde{h}_{n+1}}\\ &-q\partial_{\beta\beta^*}^2\frac{\alpha_n^l(\alpha_n^l)^*}{\tilde{h}_{n-1}}+p\partial_\beta^2\frac{\alpha_n^l(\alpha_{n+2}^l)^*}{\tilde{h}_{n+1}}-q\partial_{\beta\beta^*}^2e^{i\epsilon t}\frac{\alpha_n^e(\alpha_{n+1}^l)^*}{\tilde{h}_n}\\ &+p\partial_\beta^2e^{i\epsilon t}\frac{\alpha_n^e(\alpha_{n+3}^l)^*}{\tilde{h}_{n+2}}-q\partial_{\beta\beta^*}^2e^{-i\epsilon t}\frac{\alpha_n^l(\alpha_{n-1}^e)^*}{\tilde{h}_{n-1}}+p\partial_\beta^2e^{-i\epsilon t}\frac{\alpha_n^l(\alpha_{n+1}^e)^*}{\tilde{h}_{n+1}}\Bigg\}F\\ &+\mathrm{h.c.},\end{aligned}\tag{4.43}$$

where we have neglected terms proportional to $\propto(E_e^{op})^2$, kept only DC terms, and have used $\omega_e^{op}=\omega_m+\epsilon$, where $\omega_e^{op},\omega_m\gg\epsilon$. This allowed us to neglect fast oscillating terms while keeping only these terms oscillating with ϵt, and to send $h_n^e\to h_{n+1}$. The last EOM for F can be used to obtain FPEs for the different known phase space density functions, such as the Glauber-Sudarshan P distribution, the Wigner representation, and to the

Husimi Q representation. We now choose a specific phase space representation. To better relate to previous works [5, 79, 107], we will use the Wigner density function. We therefore place $q = p = 1/2$ in the last equation. This leads to

$$\begin{aligned}\dot{W}(\beta,\beta^*) = {} & ig_0 \sum_n \partial_{\beta^*}\left[\alpha_n^l(\alpha_{n-1}^l)^* + \alpha_n^l(\alpha_{n-2}^e)^* e^{-i\epsilon t} + \alpha_n^e(\alpha_n^l)^* e^{i\epsilon t}\right] W(\beta,\beta^*) \\ & + \sum_n \frac{g_0^2\gamma_c}{2|\tilde{h}_{n+1}|^2}\left\{\partial_{\beta^*}^2\left[-(\alpha_n^l)^*\alpha_{n+2}^l - e^{-i\epsilon t}\alpha_{n+2}^l(\alpha_{n-1}^e)^* - e^{i\epsilon t}(\alpha_n^l)^*\alpha_{n+1}^e\right]\right. \\ & \left. + \partial_{\beta\beta^*}^2\left[\frac{|\alpha_n^l|^2}{2} + \frac{|\alpha_{n+2}^l|^2}{2} + e^{i\epsilon t}(\alpha_{n+2}^l)^*\alpha_{n+1}^e + e^{i\epsilon t}(\alpha_n^l)^*\alpha_{n-1}^e\right]\right\} W(\beta,\beta^*) \\ & + \text{h.c.}.\end{aligned} \tag{4.44}$$

In describing limit-cycles and synchronization, it is more natural to work using polar coordinates. We therefore transform Eq. (4.44) to a polar coordinate system. A more detailed account of the transformation is given in Ref. [79]. The FPE for the Wigner density function $W(r,\phi)$ in the polar coordinate system is then given by

$$\dot{W}(r,\phi) = \left[-\partial_r\mu_r - \partial_\phi\mu_\phi + \partial_{rr}^2 D_{rr} + \partial_{r\phi}^2 D_{r\phi} + \partial_{\phi\phi}^2 D_{\phi\phi}\right] W(r,\phi), \tag{4.45}$$

where the drift coefficients are given by

$$\begin{aligned}\mu_\phi = {} & \frac{g_0 E_L}{r}\sum_n \left\{E_L \,\mathrm{Re}\left[\frac{J_n J_{n-1}}{h_n h_{n-1}^*}\right]\right. \\ & \left. + E_e^{op}\,\mathrm{Re}\left[\frac{e^{-i(\phi+\epsilon t)}J_n J_{n-2}}{h_n h_{n-1}^*}\right] + E_e^{op}\,\mathrm{Re}\left[\frac{e^{i(\phi+\epsilon t)}J_{n-1}J_{n-1}}{h_n h_{n-1}^*}\right]\right\},\end{aligned} \tag{4.46}$$

$$\begin{aligned}\mu_r = {} & -\frac{\gamma_m}{2}r + \sum_n g_0 E_L\left\{E_L\,\mathrm{Im}\left[\frac{J_n J_{n-1}}{h_n h_{n-1}^*}\right]\right. \\ & \left. + E_e^{op}\,\mathrm{Im}\left[\frac{e^{-i(\phi+\epsilon t)}J_n J_{n-2}}{h_n h_{n-1}^*}\right] + E_e^{op}\,\mathrm{Im}\left[\frac{e^{i(\phi+\epsilon t)}J_{n-1}J_{n-1}}{h_n h_{n-1}^*}\right]\right\}.\end{aligned} \tag{4.47}$$

In obtaining the last expressions, we have neglected terms $\propto 1/r$ in the equation for μ_r and terms $\propto 1/r^2$ in the equation for μ_ϕ, and have reincluded the effect due to Eq. (4.19).

The diffusion coefficients are given by

$$D_{\phi\phi} = \frac{\gamma_m(2n_{\rm th}+1)}{8r^2} + \sum_n \frac{\gamma_c g_0^2 E_L^2}{4r^2|\tilde{h}_{n+1}|}\left\{\frac{J_n^2}{2|h_n|^2} + \frac{J_{n+2}^2}{2|h_{n+2}|^2} + \mathrm{Re}\left[\frac{J_{n+2}J_n}{h_n h_{n+2}^*}\right]\right.$$
$$\left. + \frac{E_e^{op} J_n(J_{n+1}+J_{n-1})}{E_L|h_n|^2}\cos(\phi+\epsilon t) + \frac{E_e^{op}}{E_L}\mathrm{Re}\left[\frac{e^{i(\phi+\epsilon t)}J_{n+2}J_{n-1} + e^{-i(3\phi+\epsilon t)}J_n J_{n+1}}{h_n h_{n+2}^*}\right]\right\}, \tag{4.48}$$

$$D_{r\phi} = -\sum_n \frac{\gamma_c g_0^2 E_L^2}{2r|\tilde{h}_{n+1}|}\left\{\mathrm{Im}\left[\frac{J_{n+2}J_n}{h_n h_{n+2}^*}\right] + \frac{E_e^{op}}{E_L}\mathrm{Im}\left[\frac{e^{i(\phi+\epsilon t)}J_{n+2}J_{n-1} + e^{-i(3\phi+\epsilon t)}J_n J_{n+1}}{h_n h_{n+2}^*}\right]\right\}, \tag{4.49}$$

$$D_{rr} = \frac{\gamma_m(2n_{\rm th}+1)}{8} + \sum_n \frac{\gamma_c g_0^2 E_L^2}{4|\tilde{h}_{n+1}|}\left\{\frac{J_n^2}{2|h_n|^2} + \frac{J_{n+2}^2}{2|h_{n+2}|^2} - \mathrm{Re}\left[\frac{J_{n+2}J_n}{h_n h_{n+2}^*}\right]\right.$$
$$\left. + \frac{E_e^{op} J_n(J_{n+1}+J_{n-1})}{E_L|h_n|^2}\cos(\phi+\epsilon t) - \frac{E_e^{op}}{E_L}\mathrm{Re}\left[\frac{e^{i(\phi+\epsilon t)}J_{n+2}J_{n-1} + e^{-i(3\phi+\epsilon t)}J_n J_{n+1}}{h_n h_{n+2}^*}\right]\right\}. \tag{4.50}$$

In the limit of $E_e^{op} \to 0$, one retrieves the known expression from [79].

4.3.2 Derivation of EOM – mechanical drive

In this section we would like to present the derivation of the EOM for the Wigner density function describing the mechanical self-oscillator when an external mechanical drive is applied. The master equation describing our system is given in Eq. (4.2), together with Eq. (4.6). It can be written as (to be compared with Eq. (4.7))

$$\dot{\rho} = (\mathcal{L}_m + \mathcal{L}_c + \mathcal{L}_{\rm int})\,\rho, \tag{4.51}$$

where

$$\mathcal{L}_m\rho = -i[\omega_m b^\dagger b - iE_e^{op}\left(e^{i\omega_e^m t}b - e^{-i\omega_e^m t}b^\dagger\right),\rho] + \gamma_m\left(n_{\rm th}+1\right)D[b]\rho + \gamma_m n_{\rm th}D[b^\dagger]\rho, \tag{4.52}$$

$$\mathcal{L}_c\rho = -i\left[-\Delta a^\dagger a - i\left(a - a^\dagger\right),\rho\right] + \gamma_c D[a]\rho, \tag{4.53}$$

$$\mathcal{L}_{\rm int}\rho = -i\left[-g_0 a^\dagger a(b+b^\dagger),\rho\right]. \tag{4.54}$$

In applying the laser theory for optomechanical limit-cycles for this case, we take steps completely analogous to those taken in the section. As the mechanical reference drive acts directly on the mechanical self-oscillator, it does not appear in the solution for $\alpha(t)$ nor in the elimination of the electromagnetic cavity. This fact makes calculations more straightforward in the present case, and we do not explicitly present them here. The EOM obtained has the same form as Eq. (4.45), with drift coefficients which are given

by

$$\mu_\phi = \sum_n \frac{g_0 E_L^2}{r} \mathrm{Re}\left[\frac{J_n J_{n-1}}{h_n h_{n-1}^*}\right] - \frac{E_e^m}{r} \sin\left[(\omega_e^m - \omega_m)t + \phi\right], \tag{4.55}$$

$$\mu_r = -\frac{\gamma_m}{2} r + \sum_n g_0 E_L^2 \,\mathrm{Im}\left[\frac{J_n J_{n-1}}{h_n h_{n-1}^*}\right] + E_e^m \cos\left[(\omega_e^m - \omega_m)t + \phi\right]. \tag{4.56}$$

As in the previous case, we have neglected terms $\propto 1/r$ in the equation for μ_r and terms $\propto 1/r^2$ in the equation for μ_ϕ. The reference field E_e^m does not enter the expressions for the diffusion. The diffusion coefficients are therefore given in Eqs. (4.48)-(4.50), with $E_e^{op} = 0$. In the limit of $E_e^m \to 0$, one retrieves the known expressions from [79].

4.3.3 The Adler equation

Case (1): Optical laser drive. – The FPE, Eq. (4.45), describes the dynamics of the mechanical oscillator and, in an appropriate parameter regime, will therefore describe the synchronization of the mechanical oscillator onto the optical reference drive. In a classical parameter regime in which the noise described by the diffusion terms is negligible, we can omit the diffusion terms appearing in Eq. (4.45). Now, the onset of synchronization is characterized by the locking of the phase of the mechanical oscillator to the phase of the optical drive, while the radius of oscillation stays approximately constant. For that reason, we can neglect the term describing the drift of the radius, μ_r, while focusing on the drift of the phase, Eq. (4.46). We are therefore left with

$$\dot{W}(\phi) = -\partial_\phi \mu_\phi W(\phi), \tag{4.57}$$

from which we recognize that $\mu_\phi = \dot{\phi}$. Let us therefore focus on μ_ϕ, Eq. (4.46), which completely determines the time evolution of ϕ. The first term is the known amplitude-dependent optomechanical frequency shift $\delta\omega$ (see Ref. [5]). Using it, we obtain

$$\mu_\phi = \dot{\phi} = -\delta\omega + \frac{g_0 E_L E_e^{op}}{r} \sum_n \mathrm{Re}\left[\frac{e^{-i(\phi+\epsilon t)} J_n J_{n-2} + e^{i(\phi+\epsilon t)} J_{n-1} J_{n-1}}{h_n h_{n-1}^*}\right]. \tag{4.58}$$

In the sideband-resolved regime and with detuning close to the mechanical frequency, i.e., $\gamma_c/2 \ll \Delta_{\mathrm{eff}} \approx \omega_m$, terms with h_1 in the denominator are close to resonance. For that reason, we will keep only the terms with $n = 1, 2$. We then find

$$\dot{\phi} = -\delta\omega + E_e^{op,\mathrm{eff}} \sin(\phi + \epsilon t), \tag{4.59}$$

where we have shifted ϕ by a constant and defined the effective drive strength as

$$E_e^{op,\mathrm{eff}} = \frac{g_0 E_L E_e^{op}}{r\omega_m^2 \left(1 + \frac{\gamma_c^2}{4\omega_m^2}\right)} \sqrt{(J_2 + J_0)^2 J_0^2 + \frac{4\omega_m^2}{\gamma_c^2}(J_2 J_0 - 2J_1^2 - J_0^2)^2}. \tag{4.60}$$

Adding the frequency difference ϵ to both sides of Eq. (4.59), we obtain the Adler equation

$$\dot{\delta\phi} = (\omega_e^{op} - \omega_m^{\text{eff}}) + E_e^{op,\text{eff}} \sin(\delta\phi), \tag{4.61}$$

where the effective mechanical frequency is $\omega_m^{\text{eff}} \equiv \omega_m + \delta\omega$, and we have defined $\delta\phi \equiv \phi + \epsilon t$. Note that $\delta\phi = (\phi - \omega_m t) + \omega_e^{op} t$ is just the difference of phase of the mechanical oscillator (in a frame rotating with ω_m) to the phase of the external drive.

The Adler equation describes the synchronization of the mechanical self-oscillator to the reference drive, as shown in Fig. 4.3, in which we plot $\overline{\sin\delta\phi}$ as a function of $(\omega_e^{op} - \omega_m^{\text{eff}})$ for different drive strengths, where the overline refers to time-averaging. For $|\omega_e^{op} - \omega_m^{\text{eff}}| < E_e^{op,\text{eff}}$, the solution to Eq. (4.61) is $\dot{\delta\phi} = 0$. Therefore phase-locking takes place. For $|\omega_e^{op} - \omega_m^{\text{eff}}| \gg E_e^{op,\text{eff}}$, $\sin(\delta\phi)$ time-averages to zero. The optomechanical parameters chosen in Fig. 4.3 can be readily obtained in a wide range of experiments [8, 21, 66]. In Ref. [66] a mechanical resonator of frequency $\omega_m/(2\pi) = 9.7(\text{kHz})$ was studied, while in Ref. [21] a mechanical resonator of frequency $\omega_m/(2\pi) = 3.9(\text{GHz})$ was studied. In both, the parameters of the optomechanical system were similar to those given in Fig. 4.3.

We can further test this derived Adler equation by comparing it with the numerical prediction, which can be obtained by integrating the optomechanical EOMs for the

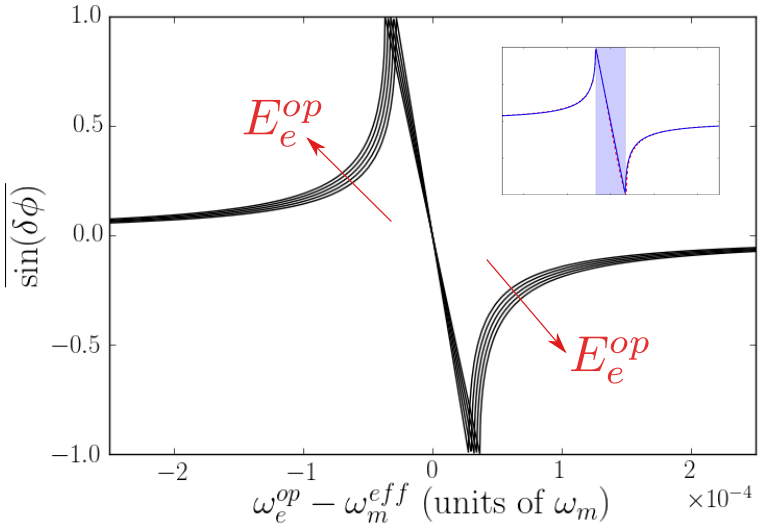

FIGURE 4.3: The main plot shows synchronization of the mechanical self-oscillator to an optical reference drive. The analytically calculated time-average $\overline{\sin(\delta\phi)}$ as a function of $(\omega_e^{op} - \omega_m^{\text{eff}})$ for different values of E_e^{op}, from 0.13 to 0.17. The inset compares the analytical solution (blue) with the numerical simulation (red dashed) for $E_e^{op} = 0.15$. It shows excellent agreement. Colored region indicates the synchronization region, $\mathrm{d}\delta\phi/\mathrm{d}t = 0$. The parameters of the optomechanical system are taken in the classical regime, $(g_0, \gamma_c, \gamma_m, E_L, \Delta, n_{\text{th}}) = (0.015, 0.5, 0.0001, 1.0, 1.0, 0) \times \omega_m$.

cavity field α and the mechanical field β [5]

$$\begin{aligned}\dot{\alpha} &= i\Delta\alpha + ig_0(\beta+\beta^*)\alpha - \frac{\gamma_c}{2}\alpha + E_L + E_e^{op}e^{-i\omega_e^{op}t},\\ \dot{\beta} &= ig_0|\alpha|^2 - i\omega_m\beta - \frac{\gamma_m}{2}\beta.\end{aligned} \tag{4.62}$$

The result is shown in the inset of Fig. 4.3. The synchronization region is indicated by the colored region. There is a very good agreement between the prediction of the derived microscopic equation and the numerical simulation.

Case (2): Mechanical drive. - Analogously to *case (1)*, in a classical parameter regime in which noise plays a negligible role, we omit the diffusion terms of the FPE. Then, focusing only on the drift of the phase since the amplitude is assumed constant, and taking identical steps to those shown in *case (1)*, one reaches an Adler equation,

$$\dot{\delta\phi} = (\omega_e^m - \omega_m^{\text{eff}}) + E_e^{m,\text{eff}}\sin(\delta\phi), \tag{4.63}$$

where the effective drive strength is

$$E_e^{m,\text{eff}} = \frac{E_e^m}{r}. \tag{4.64}$$

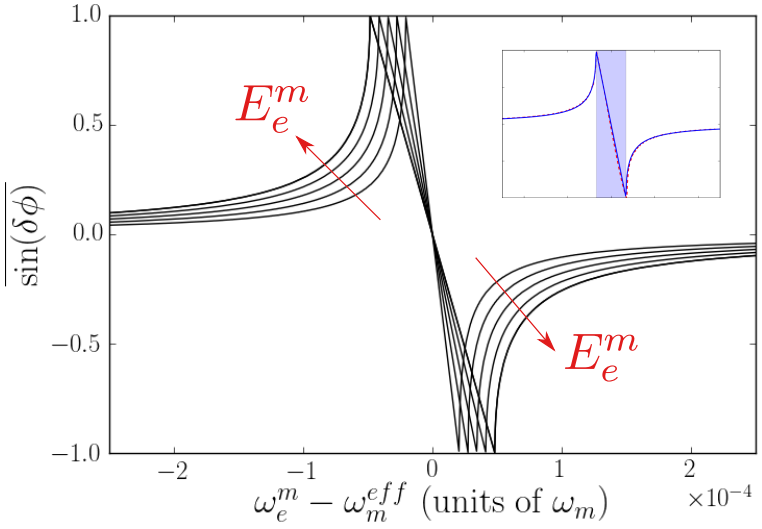

FIGURE 4.4: The main plot shows synchronization of the mechanical self-oscillator to a mechanical reference drive. The analytically calculated time-average $\overline{\sin(\delta\phi)}$ as a function of $(\omega_e^m - \omega_m^{\text{eff}})$ for different values of E_e^m, from 0.003 to 0.007. The inset compares the analytical solution (blue) with the numerical simulation (red dashed) for $E_e^m = 0.005$. It shows excellent agreement. Colored region indicates the synchronization region, $\mathrm{d}\delta\phi/\mathrm{d}t = 0$. The parameters of the optomechanical system are taken in the classical regime, $(g_0, \gamma_c, \gamma_m, E_L, \Delta, n_{\text{th}}) = (0.01, 0.3, 0.0001, 1.0, 1.0, 0) \times \omega_m$.

This form of the Adler equation agrees with [48]. In Fig. 4.4 we plot $\overline{\sin\delta\phi}$ as a function of $(\omega_e^{op} - \omega_m^{\text{eff}})$ for different drive strengths, where the overline refers to time-averaging. We can further test this analytical equation by comparing it with the classical numerical prediction, which can be obtained by integrating the EOMs [5]

$$\begin{aligned}\dot{\alpha} &= i\Delta\alpha + ig_0(\beta+\beta^*)\alpha - \frac{\gamma_c}{2}\alpha + E_L,\\ \dot{\beta} &= ig_0|\alpha|^2 - i\omega_m\beta - \frac{\gamma_m}{2}\beta + E_e^m e^{-i\omega_e^m t}.\end{aligned} \tag{4.65}$$

The comparison is seen in the inset of Fig. 4.4. A very good agreement is found between the analytical Adler equation and the numerical simulation.

4.4 Quantum synchronization: Numerical demonstration

The optomechanical system is theoretically suggested to demonstrate synchronization also in a quantum parameter regime, in which $g_0 \ll \omega_m$ does not hold anymore. In that parameter regime, the quantum shot noise plays an important role, and cannot be neglected as in the previous section. The quantum synchronization of two such systems was theoretically studied in Ref. [138]. In this section we show numerically that the mechanical self-oscillator is expected to synchronize to a reference drive in the quantum parameter regime.

Synchronization of a self-oscillator to an external drive is the development of phase preference for the self-oscillator as it tends towards phase-locking to the phase of the external drive. As shown in Fig. 4.2, this phase preference is easily seen in the phase space distribution of the mechanical oscillator. To quantify the emergence of synchronization using the information stored in the phase space distribution, we use the synchronization measure that was used in Ch. 2 and in Ch. 3,

$$S = \frac{|\langle b\rangle|}{\sqrt{\langle b^\dagger b\rangle}}, \tag{4.66}$$

where the bracket $\langle\ldots\rangle$ denotes averaging over the phase space distribution. A brief discussion regarding S can be found in Sec. 1.1.2.

Note that in the optomechanical system, the self-oscillations developing in the mechanical oscillator are centered around some point in phase space, β_c, which is generally different than the origin. This is seen in Fig. 4.2 (a). This deviation from the origin influences the synchronization measure, Eq. (4.66). This can be easily corrected and accounted for. To do so, we move to a displaced frame by using the displacement operator $D(-\beta_c) = \exp(-\beta_c b^\dagger + \beta_c b)$. For the rest of this work, we will be working in the appropriate displaced frame.

The problem of an optomechanical system with an additional reference drive, Eq. (4.2) with either Eq. (4.5) or Eq. (4.6), contains a time-dependent Hamiltonian. For that

reason, a steady state does not emerge. However, in the late-time dynamics, the system evolves into a state which is periodic in time with periodicity $\tau \equiv 2\pi/\omega_e^i$, where i denotes the optical- or the mechanical-reference drive. This is true in the synchronized state and outside the synchronized state, and it is the result of the periodic time dependence of the Hamiltonian. For that reason, in the late-time dynamics the synchronization measure S is a function of time with the same periodicity, $S(t) = S(t+\tau)$. The variation of S over the time scale τ in the late-time dynamics is relatively small, and is of order $S \sim 0.01$ at maximum. To conveniently discuss synchronization, we use $\bar{S}$, defined as the time-average of S over a period τ.

Numerical Results

To numerically study synchronization of the mechanical self-oscillator to an external drive, we use `QuTiP` [60, 61].

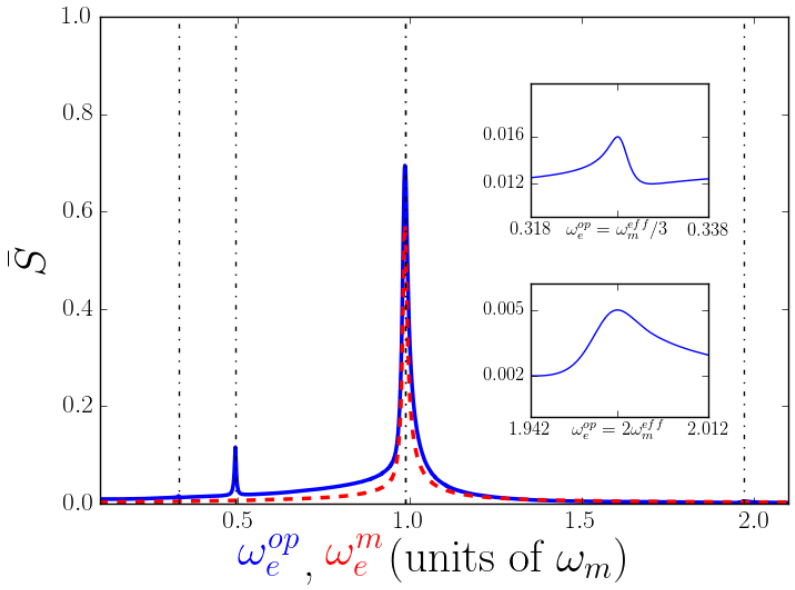

FIGURE 4.5: The time-averaged synchronization measure $\bar{S}$ as a function of the external drive frequency, shown in blue for an optical drive with $E_e^{op}/\omega_m = 0.08$ and in a red dashed line for a mechanical drive with $E_e^{m}/\omega_m = 0.008$. For the mechanical drive there is only one synchronization peak at $\omega_e^m = \omega_m^{\text{eff}}$, while the optical drive leads to multiple synchronization peaks at $\omega_e^{op} = \{\omega_m^{\text{eff}}/3, \omega_m^{\text{eff}}/2, \omega_m^{\text{eff}}, 2\omega_m^{\text{eff}}\}$. The black dotted lines are plotted at these frequencies. The synchronization peaks at $\omega_e^{op} = \{\omega_m^{\text{eff}}/3, 2\omega_m^{\text{eff}}\}$ are hardly noticeable in the scale of the figure, and are therefore shown in the two insets. Optomechanical parameters are the same as in Fig. 4.2.

Case (1): Optical laser drive. In Fig. 4.5, the time-averaged synchronization measure $\bar{S}$ is plotted in blue as a function of the frequency of the reference drive, ω_e^{op}. A main synchronization peak appears about an effective mechanical frequency, ω_m^{eff}, slightly shifted from ω_m. This shift of the mechanical frequency is known [5, 107] to be the result of the average dynamics of the electromagnetic cavity. Synchronization peaks at other frequencies are found as well: A synchronization peak about $\omega_e^{op} = \omega_m^{\text{eff}}/2$ is clearly visible, and in the insets of Fig. 4.5 we zoom in on the very small synchronization peaks at $\omega_e^{op} = \{\omega_m^{\text{eff}}/3, 2\omega_m^{\text{eff}}\}$. These synchronization peaks are known in the literature as high-order synchronization [10, 99]. While in principle high-order synchronization is always present when synchronizing a self-oscillator to a reference drive, it is in practice very difficult (if not impossible) to detect. The presence of a reference drive which contains many frequency components in its oscillation can enhance the synchronization peaks [10]. As was shown in the theoretical previous section, the effective drive of the mechanical self-oscillator, Eq. (4.22), indeed contains multiple frequencies. For that reason, and in contrast to case (2), we can observe the smaller synchronization peaks. We can also notice an asymmetry in the synchronization peak with respect to the reference field's frequency. This can be also be seen in Figs. 4.6 and 4.7. While there is no reason to expect perfect symmetry, it is visible that the case of an optical reference drive is more asymmetric. This is due to the high-order synchronization peaks.

In Fig. 4.6 we focus on the synchronization peak for $\omega_e^{op} = \omega_m^{\text{eff}}$. This corresponds to the maximal synchronization peak shown in Fig. 4.5. The synchronization measure $\bar{S}$

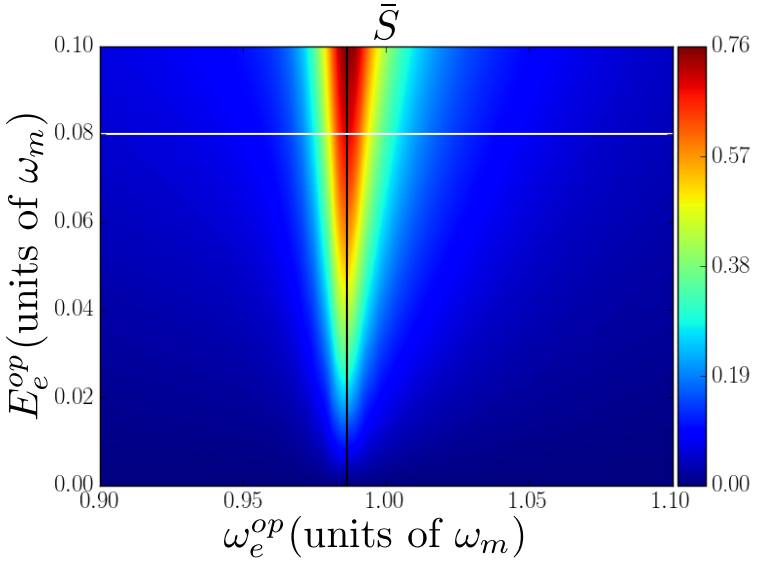

FIGURE 4.6: Arnold Tongue: The synchronization measure $\bar{S}$ is plotted as a function of the drive frequency and strength for the optical case. $\bar{S}$ has the typical shape of an Arnold tongue. The black lines marks the optomechanical effective frequency $\omega_e^{op} = \omega_m^{\text{eff}}$. The horizontal white lines mark the cut along which Fig. 4.5 is plotted. Optomechanical parameters are the same as in Fig. 4.2.

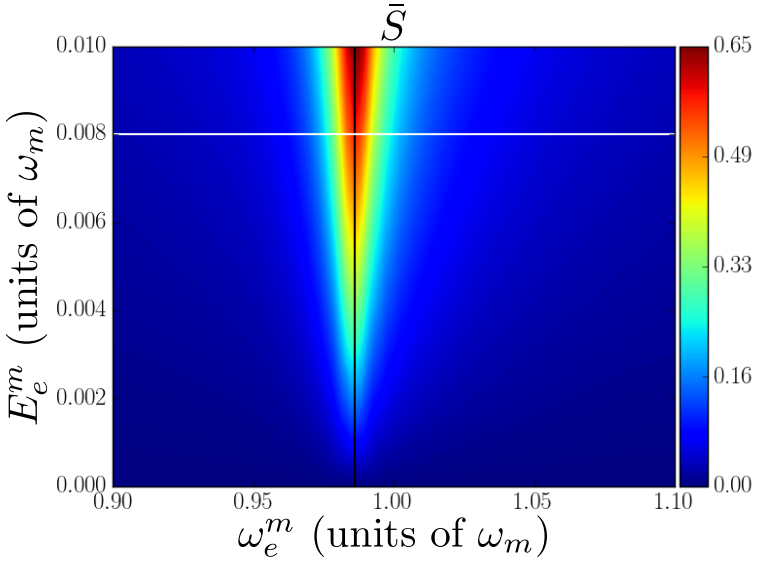

FIGURE 4.7: Arnold Tongue: The synchronization measure $\bar{S}$ is plotted as a function of the drive frequency and strength for the mechanical case. As in the optical case, $\bar{S}$ has the shape of an Arnold tongue. The black lines marks the optomechanical effective frequency $\omega_e^m = \omega_m^{\text{eff}}$. The horizontal white lines mark the cut along which Fig. 4.5 is plotted. Optomechanical parameters are the same as in Fig. 4.2.

is plotted as a function of both E_e^{op} and ω_e^{op}. Indeed, the "Arnold tongue" is present, a signature for synchronization.

Case (2): Mechanical drive. - The reference drive synchronizes the mechanical oscillator at frequency $\omega_e^m = \omega_m^{\text{eff}}$. This is shown by the red dashed curve in Fig. 4.5. In contrast to the optical case, no high-order synchronization is seen. Indeed, as the mechanical drive is acting directly on the mechanical self-oscillator, its influence is harmonic. Therefore high-order synchronization is not detected [10, 99].

In Fig. 4.7 we focus on this synchronization peak. In this figure we vary both the external frequency ω_e^m and the strength of the external drive, E_e^m, and the "Arnold tongue" is clearly observed.

4.5 Conclusions

In the work presented in this chapter, we have filled a gap in the study of synchronization of an optomechanical system. Starting from the microscopic master equation, we have analytically derived Adler equations describing the synchronization of the mechanical self-oscillator to a reference drive, in a classical parameter regime. This was done for two different reference drives, an optical one and a mechanical one (as was shown in Ref. [48]). We also show numerically that synchronization in a quantum parameter regime is expected, therefore suggesting the optomechanical system as a good candidate

for the study of quantum synchronization. In the context of this thesis, this work provides a theoretical description of the synchronization phenomenon, in both the classical and quantum parameter regimes, in a known experimental platform.

We hope that the results presented in this work can be used for future research. This may include using the FPE obtained, Eq. (4.45), and the corresponding diffusion coefficients, to explore noise-reduction. This noise reduction could perhaps be obtained in the radial direction, stabilizing the amplitude of the self-oscillator. Alternatively, it could perhaps be obtained in the tangential direction, reducing phase noise and increasing the synchronization signal in the quantum noisy regime.

CHAPTER 5

NONLOCAL QUANTUM STATE ENGINEERING WITH THE COOPER PAIR SPLITTER BEYOND THE COULOMB BLOCKADE REGIME

"The end justifies the means"

Was not said in Nicolo Machiavelli's "The Prince"

This chapter is based on our results that were published in

- Ehud Amitai, Rakesh P. Tiwari, Stefan Walter, Thomas L. Schmidt, and Simon E. Nigg
  Nonlocal quantum state engineering with the Cooper pair splitter beyond the Coulomb blockade regime
  Phys. Rev. B **93**, 075421 (2016)

A Cooper pair splitter consists of two quantum dots side-coupled to a conventional superconductor. Usually, the quantum dots are assumed to have a large charging energy compared to the superconducting gap, in order to suppress processes other than the coherent splitting of Cooper pairs. In this work, in contrast, we investigate the limit in which the charging energy is smaller than the superconducting gap. This allows us, in particular, to study the effect of a Zeeman field comparable to the charging energy. We find analytically that in this parameter regime the superconductor mediates an interdot tunneling term with a spin symmetry determined by the Zeeman field. Together with electrostatically tunable quantum dots, we show that this makes it possible to engineer a spin triplet state shared between the quantum dots. Compared to previous works, we thus extend the capabilities of the Cooper pair splitter to create entangled nonlocal electron pairs.

5.1 Introduction

In the context of this thesis, the following chapter is somewhat off topic. There is no relation to self-oscillators, quantum or classical, and therefore also no relation to synchronization or amplitude death. Still, it has become a standard for PhD candidates to try and tackle off-topic problems, if they find the problem interesting. Here, we present our published research [4] regarding quantum state engineering with a Cooper pair splitter (CPS) system, in which we propose a scheme to generate entangled non-local electronic triplet states.

Entanglement [117] is arguably one of the most fundamental aspects of quantum mechanics and is an essential resource for emerging quantum technologies. Non-local entanglement manifests itself in correlations between spatially separated parts of a quantum system that defy any classical explanation. A natural way to explore this phenomenon is by creating EPR pairs of particles, named after the influential Einstein-Podolsky-Rosen paper [36], which violate Bell's inequalities [7, 13, 43, 49, 118]. These EPR pairs are the basis for many applications of quantum information theory, such as quantum computation [31], quantum teleportation [14], and quantum communication [129].

The preparation of EPR pairs of photons is well established in the field of quantum optics and has already been applied in quantum teleportation and quantum communication [14, 129]. However, preparing an *electronic* EPR pair has proved to be rather difficult. Still, a solid state source of electronic EPR pairs is highly desirable. For example, (on-demand) generation of electronic EPR pairs would greatly facilitate the construction of quantum repeaters that are essential ingredients of a future quantum network (quantum internet) [64]. One promising approach makes use of the natural occurrence of singlet pairs of electrons in the ground state of conventional s-wave superconductors. By coupling such a superconductor to two spatially separated quantum dots (QDs), individual Cooper pairs can split and the two electrons from a pair tunnel to a different QD each. Because this process is coherent the resulting state of the two QDs is a non-local entangled singlet EPR pair. This process is dominant if both the superconducting gap Δ and the Coulomb repulsion of electrons on one QD, characterized by the on-site interaction strength $U > 0$, are large compared with the single electron tunneling rate between the superconductor and the QDs. Such devices are usually called *Cooper pair splitters* and were first proposed in Refs. [25, 75, 104] and realized experimentally in Refs. [27, 50, 52]. In these experiments, measurements of the current and current noise flowing out of the QDs have confirmed the spatial separation of the electrons from a Cooper pair. Theoretical analysis of the branching currents and their crossed correlations was done in [23, 103], and the subgap transport was studied in [37]. Only recently, measurements of the Josephson current flowing between superconducting contacts through two parallel QDs have demonstrated that the pairs are indeed entangled [29]. CPSs can also be used to probe the symmetry of the order parameter in unconventional superconductors [121, 127], as a model system exhibiting unconventional

pairing [122], to entangle mechanical resonators [133], or to engineer Majorana bound states which are not topologically protected [74].

Typical theoretical treatments of the CPS assume an infinite charging energy for each QD, making it energetically impossible for two electrons to occupy the same QD. This is known as the *Coulomb blockade approximation* and is valid as long as the QDs have a relatively large charging energy compared to other relevant energy scales in the device such as the superconducting gap and the thermal energy. In the present work we explore the opposite regime of a small charging energy compared with the superconducting gap. We show that by leveraging a combination of effects due to Coulomb repulsion, finite Zeeman magnetic field, and electrostatic tuning of the system, it is possible to prepare also non-local triplet states with zero spin in the CPS system. This is particularly interesting for solid state quantum information processing, where information is encoded in the spin degree of freedom of electrons trapped in semiconductor QD structures [31].

This chapter is organized as follows: We begin by summarizing the main results obtained in this research in Sec. 5.2. In Sec. 5.3 we describe the model we have used for the CPS system. In Sec. 5.4 we introduce the effective low-energy Hamiltonian, obtained for zero-temperature and a small charging energy in the QDs compared with the superconducting gap. Section 5.5 introduces a scheme for the generation of a non-local triplet state on the two QDs. The scheme is then explored both numerically and theoretically. We comment on possible experimental schemes to verify the successful generation of the non-local triplet state and conclude in Sec. 5.6.

5.2 Summary of the main results

For simplicity, we restrict ourselves to the zero-temperature limit and consider the coherent dynamics on time scales that are assumed to be much shorter than the coherence time of the system. Employing a Schrieffer-Wolff (SW) transformation [116], we integrate out the degrees of freedom of the superconductor and derive an effective low-energy model for the dynamics of the QDs [see Eqs. (5.10) to (5.13)].

As expected, but in contrast to the case of infinite charging energy, this effective low-energy model contains a term that allows two electrons to tunnel to the same QD. This term competes with the Cooper pair splitting process and thus reduces its efficiency. However, this suppression is of order Γ_0/U, where Γ_0 is the bare Cooper pair splitting rate and can thus be made small by reducing the tunneling strength between the superconductor and the QDs at the cost of increasing the duration of singlet generation $\sim 1/\Gamma_0$.

More interestingly, we also find that for finite on-site Coulomb repulsion on the QDs, the superconductor induces an effective inter-dot interaction term. In the presence of an (in-plane) magnetic field that lifts the spin degeneracy via the Zeeman effect by Δ_Z, the spin symmetry of this new term can be altered and the part which is anti-symmetric

under spin exchange can be made to dominate over the zero-field symmetric part. This effect together with electrostatic tuning of the QD levels can be used to generate a nonlocal triplet state with zero spin on the two QDs with high fidelity. We investigate this triplet generation scheme in detail both numerically and, within a simplified model, also analytically. We find that in a regime where $\Gamma_0 \ll U \ll \Delta_Z \ll \Delta$, the triplet fidelity that can be achieved is approximately given by

$$\mathcal{F}_T \approx 1 - \left(\frac{U}{\Delta_Z}\right)^2 - 8\left(\frac{\Gamma_0}{U}\right)^2, \tag{5.1}$$

which takes its optimal value $\mathcal{F}_T \approx 1 - 2^{5/2}\Gamma_0/\Delta_Z$ for $U = 2^{3/4}\sqrt{\Gamma_0\Delta_Z}$. This simple and intuitive fidelity formula can be used for a quick estimate of parameters for a given CPS realization. A more general expression for the fidelity, which relaxes some of the above strong inequality constraints, is derived in Sec. 5.5.

5.3 Description of the physical system and model

The system we consider is depicted schematically in Fig. 5.1. It consists of a conventional BCS (Bardeen-Cooper-Schrieffer) superconductor tunnel-coupled to two otherwise isolated QDs. We assume the coupling is local, which is justified in the limit where the superconducting coherence length is much larger than the distance between the two points on the superconductor from which the electrons tunnel onto the QDs [40, 91, 104]. We assume that only one orbital energy level per QD is relevant. This approximation essentially requires sufficiently small QDs with large level spacings. This is typical for

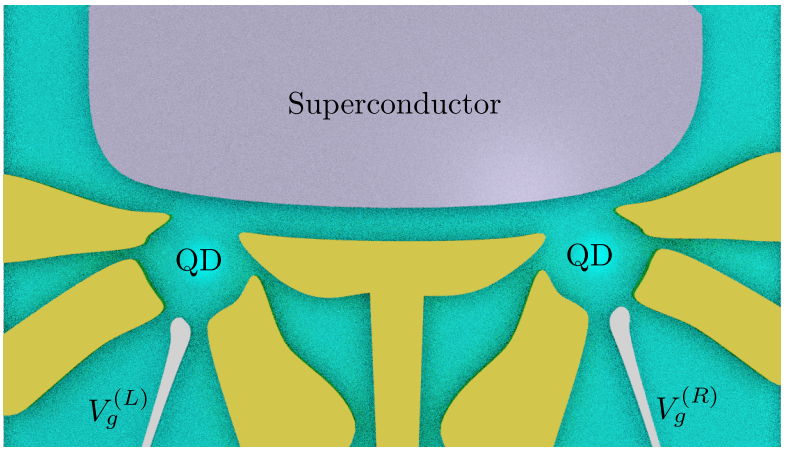

FIGURE 5.1: Schematics of the CPS system. Such a system can for example be realized by deposition of a superconductor [wide (purple) structure on the top] on top of a patterned 2DEG at the interface of a semiconductor heterostructure. The 2DEG is electrostatically depleted underneath the superconductor and underneath the gates defining the QDs (yellow structures). Further gates (elongated thin gray structures) can be used to electrostatically control the potential of the QDs.

QDs from the III-V semiconductors, for which the relevant level would be a state from the heavy-hole band [46]. States in the light-hole and conduction bands can be safely ignored due to their larger detuning from the chemical potential of the superconductor as compared to the coupling strength. We consider the zero-temperature limit where Bogoliubov quasi-particles are absent in the system. The Coulomb repulsion between two electrons of opposite spins on one QD is accounted for by the on-site energies U_L (left QD) and U_R (right QD). The chemical potentials μ_L and μ_R of the two QDs can be tuned electrostatically by a gate. Finally we also allow for an (in-plane) magnetic field to be applied to the system. This leads to a Zeeman splitting Δ_Z of the QD levels. The full system is modeled by the Hamiltonian

$$H = H_{\mathrm{BCS}} + H_{\mathrm{QDs}} + K, \tag{5.2}$$

where

$$H_{\mathrm{BCS}} = \sum_{\sigma\in\{+,-\}} \sum_{k} E_k \alpha^\dagger_{k\sigma}\alpha_{k\sigma} \tag{5.3}$$

describes the BCS superconductor via the Bogoliubov quasi-particle operators $\alpha_{k\sigma}$ of momentum k and spin σ, and energies E_k. The Hamiltonians of the QDs are given by

$$H_{\mathrm{QDs}} = \sum_{\lambda\in\{L,R\}} \sum_{\sigma} \epsilon_{\lambda\sigma} c^\dagger_{\lambda\sigma} c_{\lambda\sigma} + \sum_{\lambda\in\{L,R\}} U_\lambda n_{\lambda+} n_{\lambda-}. \tag{5.4}$$

Here $c_{\lambda\sigma}$ is a fermionic annihilation operator for an electron with spin σ in QD λ. The corresponding number operator is denoted by $n_{\lambda\sigma} = c^\dagger_{\lambda\sigma} c_{\lambda\sigma}$, and the energy levels are given by

$$\epsilon_{\lambda\sigma} = \mu_\lambda + \sigma\Delta_Z/2. \tag{5.5}$$

Finally, the coupling between the QDs and the superconductor is given by the tunneling Hamiltonian

$$K = \sum_{\lambda} w_\lambda \sum_{k\sigma} \left(c_{\lambda\sigma} d^\dagger_{k\sigma} + \mathrm{h.c.} \right), \tag{5.6}$$

where the tunnel matrix elements w_λ are assumed to be spin and momentum independent and $d_{k\sigma}$ represents the fermionic annihilation operator for an electron with energy ξ_k in the superconductor. In this tunneling Hamiltonian the superconductor is coupled only to the relevant orbital energy level of the QDs (as previously explained).

The electron operators are related to the Bogoliubov operators in the usual fashion:

$$d_{k+} = u_k \alpha_{k,+} + v_k \alpha^\dagger_{-k,-}, \qquad d_{-k,-} = u_k \alpha_{-k,-} - v_k \alpha^\dagger_{k,+}, \tag{5.7}$$

with $u_k = (1/\sqrt{2})\sqrt{1+\xi_k/E_k}$, $v_k = (1/\sqrt{2})\sqrt{1-\xi_k/E_k}$ and $E_k = \sqrt{\Delta^2+\xi_k^2}$.

5.4 Effective low-energy model

Since we are interested in a system where the tunnel coupling between the QDs and the superconductor is small compared with both the superconducting gap and the on-site charging energy of the QDs, we proceed in this section to derive an effective low-energy Hamiltonian. This model will form the basis of our investigation of the CPS beyond the Coulomb blockade regime.

The first-order process described by the tunneling Hamiltonian K is basically the tunneling of a quasi-particle from the superconductor to one of the QDs or the conjugate process. However, as we are working in the limit of zero-temperature, quasi-particles are not present. It is therefore useful to distinguish between the "high-energy subspace", which contains quasi-particle excitations, from the "low-energy subspace", which contains states with no quasi-particles. Transitions between states in the low-energy subspace can occur via virtual excursions to the high-energy subspace. This picture suggests the use of the SW transformation [116]. The SW transformation eliminates the first-order tunneling term from the Hamiltonian, at the expense of introducing all higher orders. By keeping only the leading order terms (second order in w_λ), one obtains an effective low-energy Hamiltonian. This procedure effectively integrates out the degrees of freedom of the superconductor and allows for a clearer understanding of the CPS dynamics.

The SW transformation [116] is a unitary transformation, $U \equiv e^S$. After transforming H, Eq. (5.2), we obtain

$$\tilde{H} = e^S H e^{-S} = H + [S, H] + \frac{1}{2!}[S, [S, H]] + \ldots + \frac{1}{n!}[S\,[S, [\ldots [S, H]\ldots]]] + \ldots$$

We choose the generator S of the canonical transformation such that it eliminates the perturbation to first-order in w_λ, i.e.

$$[S, H_{\mathrm{BCS}} + H_{\mathrm{QDs}}] = -K. \tag{5.8}$$

Then, the transformed Hamiltonian becomes,

$$\tilde{H} = H_{\mathrm{BCS}} + H_{\mathrm{QDs}} + \frac{1}{2}[S, K] + \mathcal{O}(w_\lambda^3).$$

Keeping terms up to second order in w_λ/Δ, we find our low-energy Hamiltonian,

$$H_{\mathrm{LE}} = H_{\mathrm{BCS}} + H_{\mathrm{QDs}} + H_{\mathrm{SW}},$$

where we have defined $H_{\rm SW} \equiv [S,K]/2$. The solution of Eq. (5.8) is given by [110]

$$S = \sum_{\lambda}\sum_{k}\sum_{\sigma} w_{\lambda k}\left[\left(\frac{1-n_{\lambda\bar{\sigma}}}{E_k-\epsilon_{\lambda,\sigma}}+\frac{n_{\lambda\bar{\sigma}}}{E_k-\epsilon_{\lambda,\sigma}-U_\lambda}\right)u_k\alpha^\dagger_{k\sigma}c_{\lambda\sigma}\right.$$
$$\left.+\sigma\left(\frac{1-n_{\lambda\sigma}}{E_k+\epsilon_{\lambda,\bar{\sigma}}}+\frac{n_{\lambda\sigma}}{E_k+\epsilon_{\lambda,\bar{\sigma}}+U_\lambda}\right)v_k\alpha_{k\sigma}c_{\lambda\bar{\sigma}}\right]-\text{h.c.},$$

as can be easily verified by substitution. Using this generator, one can calculate $H_{\rm SW}$. This can be done quite generally, for different values of $\Delta, \Delta_Z, U_\lambda$ and k_BT (as long as one keeps in mind that keeping the leading order term in the SW transformation is justified for $\Delta \gg k_BT$). However, as we are interested in the regime where the superconducting gap Δ is much larger than the thermal energy, we furthermore assume that the superconductor is at zero-temperature (i.e. we eliminate the quasi-particle $\alpha_{k\sigma}$ degrees of freedom by taking the expectation value of $H_{\rm SW}$ in a state with no quasi-particles). After integrating out the k dependence using the assumption $\Delta > U_\lambda + \Delta_Z/2$, one obtains an effective low-energy Hamiltonian,

$$H_{\rm LE} = H_{\rm QDs} + H_S + H_P + H_D, \tag{5.9}$$

where $H_{\rm QDs}$ is the QDs Hamiltonian appearing in Eq. (5.4), and the other terms are given by

$$\frac{H_S}{\Gamma_{LR}} = \left(\frac{2-n_{L-}-n_{R+}}{\sqrt{1-\left(\frac{\Delta_Z}{2\Delta}\right)^2}}+\frac{n_{L-}}{\sqrt{1-\left(\frac{\Delta_Z/2+U_L}{\Delta}\right)^2}}+\frac{n_{R+}}{\sqrt{1-\left(\frac{\Delta_Z/2-U_R}{\Delta}\right)^2}}\right)c^\dagger_{L+}c^\dagger_{R-}$$
$$-\left(\frac{2-n_{R-}-n_{L+}}{\sqrt{1-\left(\frac{\Delta_Z}{2\Delta}\right)^2}}+\frac{n_{L+}}{\sqrt{1-\left(\frac{\Delta_Z/2-U_L}{\Delta}\right)^2}}+\frac{n_{R-}}{\sqrt{1-\left(\frac{\Delta_Z/2+U_R}{\Delta}\right)^2}}\right)c^\dagger_{L-}c^\dagger_{R+}+\text{h.c.},$$

$$\frac{H_D}{\Gamma_{LR}} = \left(\frac{2-n_{L-}-n_{R-}}{\sqrt{\left(\frac{2\Delta}{\Delta_Z}\right)^2-1}}+\frac{n_{L-}}{\sqrt{\left(\frac{\Delta}{\Delta_Z/2+U_L}\right)^2-1}}+\frac{n_{R-}}{\sqrt{\left(\frac{\Delta}{\Delta_Z/2+U_R}\right)^2-1}}\right)c_{L+}c^\dagger_{R+}$$
$$-\left(\frac{2-n_{L+}-n_{R+}}{\sqrt{\left(\frac{2\Delta}{\Delta_Z}\right)^2-1}}+\frac{\text{sgn}\left(\frac{\Delta_Z}{2}-U_R\right)n_{R+}}{\sqrt{\left(\frac{\Delta}{\Delta_Z/2-U_R}\right)^2-1}}+\frac{\text{sgn}\left(\frac{\Delta_Z}{2}-U_L\right)n_{L+}}{\sqrt{\left(\frac{\Delta}{\Delta_Z/2-U_L}\right)^2-1}}\right)c_{L-}c^\dagger_{R-}+\text{h.c.},$$

$$H_P{=}\Gamma_{RR}\left(\frac{1}{\sqrt{1-\left(\frac{\Delta_Z}{2\Delta}\right)^2}}+\frac{\pi+2\tan^{-1}\left(\frac{\frac{\Delta_Z/2+U_R}{\Delta}}{\sqrt{1-\left(\frac{\Delta_Z/2+U_R}{\Delta}\right)^2}}\right)}{2\pi\sqrt{1-\left(\frac{\Delta_Z/2+U_R}{\Delta}\right)^2}}+\frac{\pi-2\tan^{-1}\left(\frac{\frac{\Delta_Z/2-U_R}{\Delta}}{\sqrt{1-\left(\frac{\Delta_Z/2-U_R}{\Delta}\right)^2}}\right)}{2\pi\sqrt{1-\left(\frac{\Delta_Z/2-U_R}{\Delta}\right)^2}}\right)c^\dagger_{R+}c^\dagger_{R-}$$

$$+\Gamma_{LL}\left(\frac{1}{\sqrt{1-\left(\frac{\Delta_Z}{2\Delta}\right)^2}}+\frac{\pi+2\tan^{-1}\left(\frac{\frac{\Delta_Z/2+U_L}{\Delta}}{\sqrt{1-\left(\frac{\Delta_Z/2+U_L}{\Delta}\right)^2}}\right)}{2\pi\sqrt{1-\left(\frac{\Delta_Z/2+U_L}{\Delta}\right)^2}}+\frac{\pi-2\tan^{-1}\left(\frac{\frac{\Delta_Z/2-U_L}{\Delta}}{\sqrt{1-\left(\frac{\Delta_Z/2-U_L}{\Delta}\right)^2}}\right)}{2\pi\sqrt{1-\left(\frac{\Delta_Z/2-U_L}{\Delta}\right)^2}}\right)c^\dagger_{L+}c^\dagger_{L-}+\text{h.c.},$$

where we have defined $\Gamma_{ij} = \pi\rho_0\omega_i\omega_j/2$, with $i,j \in [L,R]$, and where ρ_0 is the normal state density of states at the Fermi energy of the superconductor. In the last equation, H_S contains the standard Cooper pair splitting process which, in contrast to the Cooper pair splitting described using the Coulomb blockade approximation, depends now on the occupation of the QDs via the number operators. H_D describes an effective inter-dot tunneling processes which is mediated via the superconductor, and H_p describes the tunneling of a Cooper pair onto a single QD. The processes described in H_P and in H_D are obviously not accounted for in the standard Coulomb blockade approximation. Assuming $w_L = w_R = w$ and $U_L = U_R = U$, one can obtain the reduced form of the low-energy Hamiltonian which we shall use further below, Eq. (5.10). In the zero-field limit these expressions further simplify and are provided here for completeness. They read:

$$H_S^{\Delta_Z\to 0} = \frac{\Gamma_0}{2}\left[\left(2-n_{L-}-n_{R+}+\frac{n_{L-}+n_{R+}}{\sqrt{1-\left(\frac{U}{\Delta}\right)^2}}\right)c^\dagger_{L+}c^\dagger_{R-}\right.$$
$$\left.-\left(2-n_{L+}-n_{R-}+\frac{n_{L+}+n_{R-}}{\sqrt{1-\left(\frac{U}{\Delta}\right)^2}}\right)c^\dagger_{L-}c^\dagger_{R+}\right]+\text{h.c.}$$

$$H_P^{\Delta_Z\to 0} = \frac{\Gamma_0}{2}\left(1+\frac{1+\frac{2}{\pi}\tan^{-1}\left(\frac{1}{\sqrt{\left(\frac{\Delta}{U}\right)^2-1}}\right)}{\sqrt{1-\left(\frac{U}{\Delta}\right)^2}}\right)\sum_{\alpha=L,R}c^\dagger_{\alpha+}c^\dagger_{\alpha-}+\text{h.c.}$$

$$H_D^{\Delta_Z\to 0} = \frac{\Gamma_0}{2}\frac{1}{\sqrt{\left(\frac{\Delta}{U}\right)^2-1}}\sum_{\sigma=\pm}\left(n_{L\sigma}+n_{R\sigma}\right)c_{L\bar{\sigma}}c^\dagger_{R\bar{\sigma}}+\text{h.c.},$$

where $\Gamma_0 = \pi\rho_0|\omega|^2$. Further insight into the effective Hamiltonian, Eq. (5.9), can be gained by examining the limiting case of an infinite superconducting gap. In that limit, important for transport processes involving Andreev reflection, effective Hamiltonians for proximised QDs have already been introduced in the

literature [33, 37, 122]. Taking this limit in Eq. (5.9), one obtains

$$H_{\mathrm{LE}}^{\Delta\to\infty} = \frac{H_{\mathrm{QDs}}}{2} + 2\Gamma_{LR} c_{L+}^\dagger c_{R-}^\dagger - 2\Gamma_{LR} c_{L-}^\dagger c_{R+}^\dagger + 2\Gamma_{RR} c_{R+}^\dagger c_{R-}^\dagger + 2\Gamma_{LL} c_{L+}^\dagger c_{L-}^\dagger + \mathrm{h.c.}$$

This result agrees with [122] for example.

After employing the SW transformation, we shall now consider a left-right symmetric system, i.e. $w_L = w_R = w$ and $U_L = U_R = U$. Note that the chemical potentials of the left and right QDs can still differ from each other. The expression for the corresponding effective low-energy Hamiltonian is given by

$$H_{\mathrm{LE}} = H_{\mathrm{QDs}} + H_S + H_P + H_D, \tag{5.10}$$

where H_{QDs} is given in Eq. (5.4), and the other terms are given by

$$\begin{aligned} H_S = {} & \frac{\Gamma_0}{2}\left(\frac{2-n_{L-}-n_{R+}}{\sqrt{1-\left(\frac{\Delta_Z}{2\Delta}\right)^2}} + \frac{n_{L-}}{\sqrt{1-\left(\frac{U+\Delta_Z/2}{\Delta}\right)^2}} + \frac{n_{R+}}{\sqrt{1-\left(\frac{U-\Delta_Z/2}{\Delta}\right)^2}}\right) c_{L+}^\dagger c_{R-}^\dagger \\ & - \frac{\Gamma_0}{2}\left(\frac{2-n_{L+}-n_{R-}}{\sqrt{1-\left(\frac{\Delta_Z}{2\Delta}\right)^2}} + \frac{n_{L+}}{\sqrt{1-\left(\frac{U-\Delta_Z/2}{\Delta}\right)^2}} + \frac{n_{R-}}{\sqrt{1-\left(\frac{U+\Delta_Z/2}{\Delta}\right)^2}}\right) c_{L-}^\dagger c_{R+}^\dagger + \mathrm{h.c.}, \end{aligned} \tag{5.11}$$

$$H_P = \Gamma_P\left(c_{R+}^\dagger c_{R-}^\dagger + c_{L+}^\dagger c_{L-}^\dagger\right) + \mathrm{h.c.}, \tag{5.12}$$

$$\begin{aligned} H_D = {} & \frac{\Gamma_0}{2}\left(\frac{n_{L-}+n_{R-}}{\sqrt{\left(\frac{\Delta}{U+\Delta_Z/2}\right)^2-1}} + \frac{2-n_{L-}-n_{R-}}{\sqrt{\left(\frac{2\Delta}{\Delta_Z}\right)^2-1}}\right) c_{L+} c_{R+}^\dagger \\ & + \frac{\Gamma_0}{2}\left(\frac{\mathrm{sgn}(U-\Delta_Z/2)(n_{L+}+n_{R+})}{\sqrt{\left(\frac{\Delta}{U-\Delta_Z/2}\right)^2-1}} - \frac{2-n_{L+}-n_{R+}}{\sqrt{\left(\frac{2\Delta}{\Delta_Z}\right)^2-1}}\right) c_{L-} c_{R-}^\dagger + \mathrm{h.c.}. \end{aligned} \tag{5.13}$$

Here we have defined the bare resonant Cooper pair splitting rate $\Gamma_0 = \pi\rho_0|w|^2$, with the normal state density of states at the Fermi energy of the superconductor ρ_0, and

where

$$\Gamma_P = \frac{\Gamma_0}{2}\left[\frac{1}{\sqrt{1-\left(\frac{\Delta_Z}{2\Delta}\right)^2}} + \frac{\frac{1}{2}+\frac{1}{\pi}\tan^{-1}\left(\frac{U+\Delta_Z/2}{\sqrt{\Delta^2-(U+\Delta_Z/2)^2}}\right)}{\sqrt{1-\left(\frac{U+\Delta_Z/2}{\Delta}\right)^2}} + \frac{\frac{1}{2}+\frac{1}{\pi}\tan^{-1}\left(\frac{U-\Delta_Z/2}{\sqrt{\Delta^2-(U-\Delta_Z/2)^2}}\right)}{\sqrt{1-\left(\frac{U-\Delta_Z/2}{\Delta}\right)^2}}\right] \tag{5.14}$$

is the pair tunneling rate. Each of the above terms describes a different physical process: H_S describes the Cooper pair splitting, which now depends on the occupancies of the QDs via the number operators $n_{\lambda\sigma}$. H_P describes the pair-tunneling to the same QD. In addition, the superconductor is found to mediate an effective interaction between the two QDs as described by H_D. The latter term has been derived previously in the infinite-U limit [91]. However, since double occupancy is strictly forbidden, this term does not contribute to the dynamics in the latter case. As we show next, for finite U, this term is relevant and can be utilized to generate a non-local triplet state on the two QDs. Equations (5.10) to (5.13) represent the main technical result of the work presented in this chapter. This effective model is a valid low-energy approximation as long as $\Gamma_0, \Delta_Z/2, U \ll \Delta$.

5.5 Triplet generation for finite onsite repulsion and Zeeman field

In this section we present a scheme to generate a non-local triplet state on the two QDs with finite on-site repulsion and in the presence of a finite Zeeman field. This scheme is illustrated in Fig. 5.2. The central ingredient of this scheme is the inter-dot tunneling term H_D in the regime where $U < \Delta_Z/2$. In this case, when H_D acts on a state where one of the QDs is empty while the other is doubly occupied it can be simplified to

$$H_D = \Gamma_+\left(c_{L+}c^\dagger_{R+} + c_{L-}c^\dagger_{R-}\right) + \Gamma_-\left(c_{L+}c^\dagger_{R+} - c_{L-}c^\dagger_{R-}\right) + \text{h.c.}, \tag{5.15}$$

with

$$\Gamma_+ = \frac{\Gamma_0}{4}\left(\frac{1}{\sqrt{\left(\frac{\Delta}{U+\Delta_Z/2}\right)^2-1}} - \frac{1}{\sqrt{\left(\frac{\Delta}{U-\Delta_Z/2}\right)^2-1}}\right), \tag{5.16}$$

$$\Gamma_- = \frac{\Gamma_0}{4}\left(\frac{1}{\sqrt{\left(\frac{\Delta}{U+\Delta_Z/2}\right)^2-1}} + \frac{1}{\sqrt{\left(\frac{\Delta}{U-\Delta_Z/2}\right)^2-1}}\right) + \left(\frac{\Delta_Z}{2\Delta}\right)\frac{\Gamma_S}{2}, \tag{5.17}$$

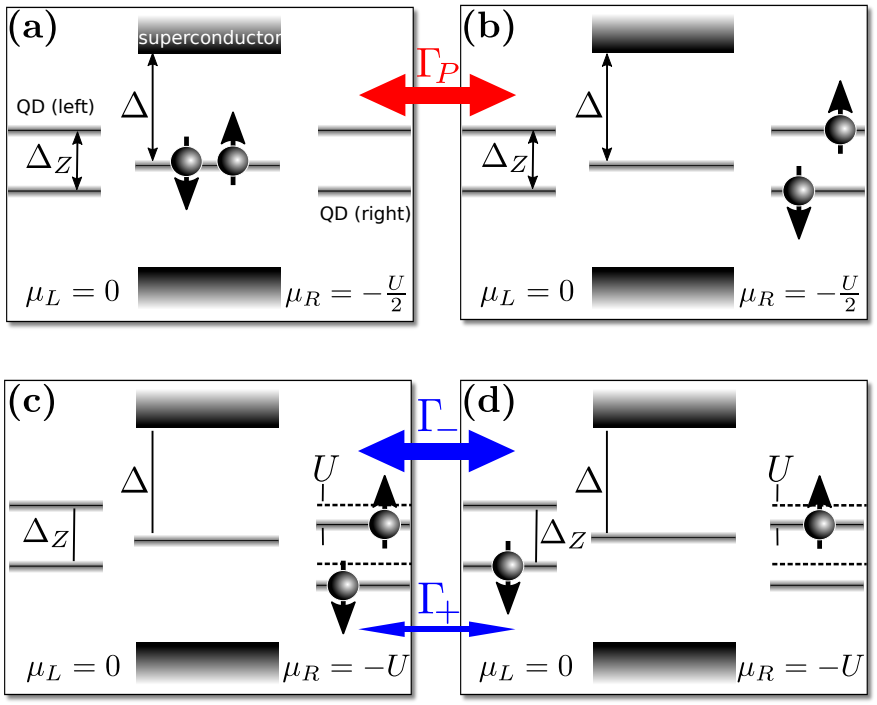

FIGURE 5.2: Schematics of the dominant processes for generating the non-local triplet state $|T\rangle = (|+\rangle_L |-\rangle_R + |-\rangle_L |+\rangle_R)/\sqrt{2}$. Panel (a) shows the initial state right after switching the potential of the right QD to $\mu_R = -U/2$. Both QDs are unoccupied and electrons form CPs in the superconductor. A magnetic field lifts the spin-degeneracy of the QD levels by Δ_Z. Panel (b) shows the state where a CP has been transferred to the right QD at time T_1. The rate for this process is given by Γ_P, Eq. (5.14). Panel (c) shows the state right after time T_1 when the potential of the right QD has been switched to $-U$. Taking into account the chemical potential and the charging energy, we see that now the energy levels are shifted by $-U$. Panel (d) shows the state after an electron from the right QD (here the down spin electron) has been transferred to the left QD at time $T_1 + T_2$. This process is driven by the inter-dot tunneling term. If $U \ll \Delta_Z/2$, the latter is dominated by the spin anti-symmetric term with rate Γ_-, Eq. (5.17), as compared with the spin symmetric term with rate Γ_+, Eq. (5.16). The same processes but with the spin states interchanged are equally likely and their amplitudes add coherently resulting in the generation of a triplet state.

$$\Gamma_S = \frac{\Gamma_0}{\sqrt{1 - \left(\frac{\Delta_Z}{2\Delta}\right)^2}}. \tag{5.18}$$

The terms proportional to Γ_+ are symmetric under spin exchange and induce non-local singlet pairs, while the terms proportional to Γ_- are anti-symmetric under spin exchange and induce non-local triplet pairs. The last two observations are the basis for our non-local triplet state generating scheme:

- We shall prepare a state where one QD is empty and the other is doubly occupied. To do so, we take advantage of the Coulomb repulsion and the gate tunability

of the energy levels of the QDs. Specifically, if the charging energy is such that $U/2 \gg \Gamma_0$ and if we initially detune say the right QD by $\mu_R = -U/2$, then the Cooper pair splitting term H_S and the inter-dot tunneling term H_D are detuned off resonance and hence suppressed while the pair tunneling term to the right QD in $H_P = \Gamma_P \left(c^\dagger_{R+} c^\dagger_{R-} + c^\dagger_{L+} c^\dagger_{L-} \right)$ is made resonant [see Fig. 5.2, panels (a) and (b)]. Hence after half a Rabi period T_1 (to be calculated below) the right QD will be doubly occupied and the left QD will be empty.

- At time T_1, the right QD is then quickly detuned further to $\mu_R = -U$. This detunes the pair tunneling term off resonance and hence suppresses it while making the inter-dot term resonant [see Fig. 5.2, panels (c) and (d)]. After another half a Rabi period of T_2 (to be calculated below), a state with a large non-local triplet population is generated on the two QDs.

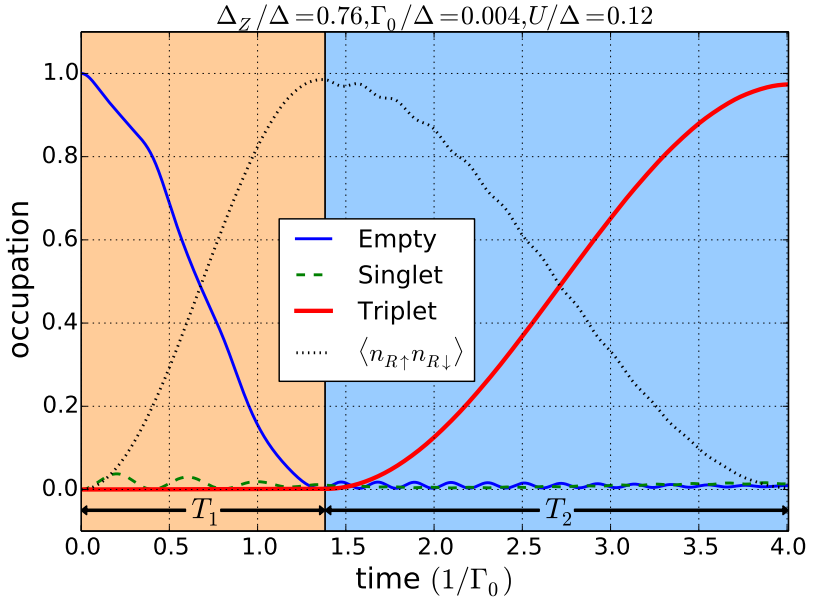

FIGURE 5.3: Dynamics of the triplet state generation for $U/\Delta = 0.12$, $\Delta_Z/\Delta = 0.76$ and $\Gamma_0/\Delta = 0.004$. The two shaded areas of the graph correspond to the two stages of the protocol described in the text and are separated by the switching of the potential of the right QD from $-U/2$ to $-U$, (see also Fig. 5.2). In the first stage, population is transferred from the vacuum (solid (blue) line) to the doubly occupied state of the right QD (dotted (black) line). In the second stage, population is transferred from the doubly occupied state to the non-local triplet (solid thick (red) line). A maximal triplet fidelity of 97% is reached at time $T_1 + T_2$. Note also the presence of a small oscillatory population of the non local singlet state (dashed (green) line).

5.5.1 Numerical results

Using the scheme just described, we have numerically solved the Schrödinger equation with the full Hamiltonian (5.10). The results are illustrated in Fig. 5.3, where it is shown that a triplet state with 97% fidelity can be obtained for parameters satisfying $\Gamma_0 \ll U \ll \Delta_Z \ll \Delta$. In the simulation, we assume a chemical potential switching time fast compared to T_1 and T_2.

Figure 5.4 shows how the maximal triplet fidelity depends on the on-site interaction strength and Zeeman field. The general trend is well captured by the analytic approximation (5.1) (see upper panel of Fig. 5.4 for a direct comparison). It is noteworthy that for small values of U, the fidelity suppression is somewhat stronger than predicted by Eq. (5.1). This together with the weak oscillations of the fidelity as a function of U can be attributed to higher order terms, neglected in the analytic approximation, which is shown in the following Sec. 5.5.2.

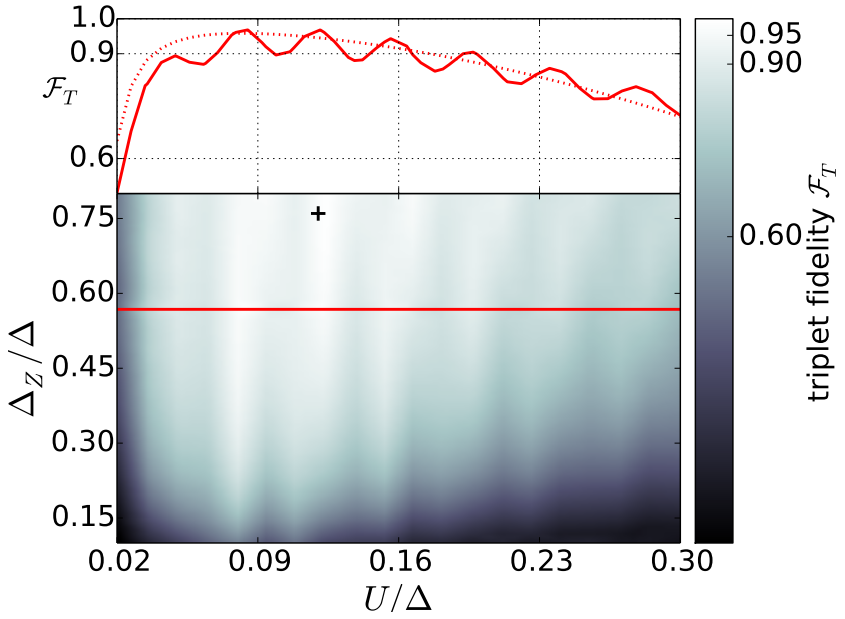

FIGURE 5.4: The contour plot shows the fidelity of the triplet state generation as a function of on-site interaction strength U and Zeeman field Δ_Z for $\Gamma_0/\Delta = 0.004$. The (black) cross indicates the parameters used in the plot of Fig. 5.3. The solid (red) line in the upper panel shows the fidelity for a fixed value of $\Delta_Z = 0.56$ indicated by the solid (red) line in the contour plot. In the regime where $\Gamma_0 \ll U \ll \Delta_Z \ll \Delta$, the triplet fidelity is well approximated by the analytic expression $\mathcal{F}_T \approx 1 - (U/\Delta_Z)^2 - 8(\Gamma_0/U)^2$ (dotted (red) line). Weak oscillations of the fidelity as a function of U are clearly visible.

5.5.2 Analytical treatment

In the following, we introduce and analytically solve a simplified model for the dynamics of the triplet state generation scheme. We motivate this model using Fig. 5.3, which shows the population dynamics in the parameter regime suitable for triplet generation. The crucial observation is that in each of the two stages of the scheme, only three states are significantly populated. More specifically, in stage I, these states are (i) the vacuum $|V\rangle = |0\rangle_L |0\rangle_R$, (ii) the doubly occupied state of the right QD $|D\rangle = c^\dagger_{R+} c^\dagger_{R-} |V\rangle$, and (iii) the non local singlet state $|S\rangle = (c^\dagger_{L+} c^\dagger_{R-} - c^\dagger_{L-} c^\dagger_{R+})/\sqrt{2}\,|V\rangle$. In stage II the three states are (i) the doubly occupied state $|D\rangle$, (ii) the non local triplet state $|T\rangle = (c^\dagger_{L+} c^\dagger_{R-} + c^\dagger_{L-} c^\dagger_{R+})/\sqrt{2}\,|V\rangle$, and (iii) the non local singlet $|S\rangle$. This fact suggests that we can approximately neglect the occupation of all other states and project the system onto three dimensional subspaces in both stages I and II and match the solutions at the interface (i.e. at time T_1). We proceed by treating the two stages separately.

Stage I: In the subspace $\{|V\rangle, |D\rangle, |S\rangle\}$ the Hamiltonian is given by

$$H_{\mathrm{I}} = \begin{pmatrix} 0 & \Gamma_{\mathrm{P}} & \sqrt{2}\Gamma_{\mathrm{S}} \\ \Gamma_{\mathrm{P}} & 0 & \sqrt{2}\Gamma_{+} \\ \sqrt{2}\Gamma_{\mathrm{S}} & \sqrt{2}\Gamma_{+} & -U/2 \end{pmatrix},$$

where the matrix elements are defined in terms of the rates given in Eqs. (5.14), (5.16) and (5.18), and the factors of $\sqrt{2}$ appear because of the normalization of the singlet state. We now make use of the fact that in stage I, the QDs are tuned such that the vacuum state and the doubly occupied state are resonant with each other while the singlet is off resonance by $U/2 \gg \Gamma_S, \Gamma_+, \Gamma_P$. To carry out the degenerate perturbation theory, we switch to a new basis given by the states

$$\begin{aligned} |0\rangle &\equiv \frac{1}{\sqrt{2}} \left(|V\rangle + |D\rangle \right), \\ |1\rangle &\equiv \frac{1}{\sqrt{2}} \left(|V\rangle - |D\rangle \right), \\ |2\rangle &\equiv |S\rangle . \end{aligned}$$

In this new basis, the Hamiltonian takes the form

$$H = \begin{pmatrix} \Gamma_{\mathrm{P}} & 0 & \Gamma_{\mathrm{S}} + \Gamma_{+} \\ 0 & -\Gamma_{\mathrm{P}} & \Gamma_{\mathrm{S}} - \Gamma_{+} \\ \Gamma_{\mathrm{S}} + \Gamma_{+} & \Gamma_{\mathrm{S}} - \Gamma_{+} & -U/2 \end{pmatrix}.$$

Treating the off-diagonal terms as perturbation, we find the corrections to the states $|0\rangle, |1\rangle$ and $|2\rangle$ and the corresponding eigenenergies up to second order:

$$
\begin{aligned}
|\tilde{0}\rangle &= \frac{|V\rangle + |D\rangle}{\sqrt{2}} + \frac{\Gamma_\mathrm{S} + \Gamma_+}{U/2 + \Gamma_\mathrm{P}} |S\rangle, \\
|\tilde{1}\rangle &= \frac{|V\rangle - |D\rangle}{\sqrt{2}} + \frac{\Gamma_\mathrm{S} - \Gamma_+}{U/2 - \Gamma_\mathrm{P}} |S\rangle, \\
|\tilde{2}\rangle &= |S\rangle + \sqrt{2}\left(\frac{\Gamma_\mathrm{S} U/2 - \Gamma_+\Gamma_\mathrm{P}}{\Gamma_\mathrm{P}^2 - (U/2)^2} |V\rangle + \frac{\Gamma_+ U/2 - \Gamma_\mathrm{S}\Gamma_\mathrm{P}}{\Gamma_\mathrm{P}^2 - (U/2)^2} |D\rangle\right) \\
\tilde{E}_0 &= \Gamma_\mathrm{P} + \frac{(\Gamma_\mathrm{S} + \Gamma_+)^2}{U/2 + \Gamma_\mathrm{P}}, \\
\tilde{E}_1 &= -\Gamma_\mathrm{P} + \frac{(\Gamma_\mathrm{S} - \Gamma_+)^2}{U/2 - \Gamma_\mathrm{P}}, \\
\tilde{E}_2 &= -\frac{U}{2} - \frac{(\Gamma_\mathrm{S} + \Gamma_+)^2}{U/2 + \Gamma_\mathrm{P}} - \frac{(\Gamma_\mathrm{S} - \Gamma_+)^2}{U/2 - \Gamma_\mathrm{P}}.
\end{aligned}
$$

Assuming that at time $t = 0$ the system is in the vacuum state $|V\rangle$, we can approximate the state at time t as

$$
|\psi(t)\rangle = \sum_{n=0}^{2} e^{-i\tilde{E}_n t/\hbar} \langle \tilde{n}|V\rangle |\tilde{n}\rangle .
$$

Hence the probability that the right QD is doubly occupied at time t (equivalent to the fidelity of the doubly occupied state) is found to be

$$
\begin{aligned}
\mathcal{F}_D^{(\mathrm{I})}(t) = |\langle D|\psi(t)\rangle|^2 = \frac{1}{1 + \frac{8\Gamma_\mathrm{S}^2}{U^2}} \Bigg\{ & \sin^2\left[t\left(\Gamma_\mathrm{P} + \frac{4\Gamma_\mathrm{S}\Gamma_+}{U}\right)\right] \\
& - \frac{16\Gamma_\mathrm{S}\Gamma_+}{U^2} \sin(\Gamma_\mathrm{P} t) \sin\left[t\left(\frac{U}{2} + 6\frac{\Gamma_\mathrm{S}^2 + \Gamma_+^2}{U}\right)\right]\Bigg\}. \quad (5.19)
\end{aligned}
$$

The term on the first line of this equation describes the leading order suppression of the fidelity due to the off-resonant transitions between the vacuum and the singlet while the second line describes higher order corrections ($\sim \mathcal{O}\left(\Gamma_S\Gamma_+/U^2\right)$). Physically, the latter describe the second order process where a non local singlet is first created out of the vacuum and then transferred to a doubly occupied state by the action of the spin-symmetric part of the inter-dot tunneling Hamiltonian. Because the amplitude of this process adds coherently, it leads to small amplitude oscillations of the fidelity at a frequency of the order of charging energy U. Neglecting these small oscillations and expanding to leading order, we obtain the estimates for the optimal double occupancy time

$$
T_1 \approx \frac{\pi}{2}\left(\Gamma_P + \frac{4\Gamma_S\Gamma_+}{U}\right)^{-1}, \quad (5.20)
$$

as well as the maximal fidelity of double occupancy

$$
\mathcal{F}_D \approx 1 - 8(\Gamma_S/U)^2. \quad (5.21)
$$

Using the perturbative approach, we note also that the probability for the system to be found in the vacuum state $|V\rangle$ at time t is

$$\mathcal{F}_V^{(\mathrm{I})}(t) = \frac{1}{1+\frac{8\Gamma_\mathrm{S}^2}{U^2}}\left\{\cos^2\left[t\left(\Gamma_\mathrm{P}+\frac{4\Gamma_\mathrm{S}\Gamma_+}{U}\right)\right]+\frac{16\Gamma_\mathrm{S}^2}{U^2}\cos\left(\Gamma_\mathrm{P}t\right)\cos\left[t\left(\frac{U}{2}+6\frac{\Gamma_\mathrm{S}^2+\Gamma_+^2}{U}\right)\right]\right\}, \tag{5.22}$$

and the probability for the system to be found in the singlet state $|S\rangle$ at time t is given by

$$\mathcal{F}_S^{(\mathrm{I})}(t) = \frac{2}{\frac{U^2}{\Gamma_S^2}+8}\left\{4+\sin^2\left[t\left(\Gamma_\mathrm{P}+\frac{4\Gamma_\mathrm{S}\Gamma_+}{U}\right)\right]+4\left(\cos^2\left[t\left(\Gamma_\mathrm{P}+\frac{4\Gamma_\mathrm{S}\Gamma_+}{U}\right)\right]\right.\right.$$
$$\left.\left.-2\cos\left(\Gamma_\mathrm{P}t\right)\cos\left[t\left(\frac{U}{2}+6\frac{\Gamma_\mathrm{S}^2+\Gamma_+^2}{U}\right)\right]\right)\right\}. \tag{5.23}$$

Stage II: The analysis of stage II is very similar. In this stage the relevant states form the subspace $\{|D\rangle, |T\rangle, |S\rangle\}$. The resulting three level Hamiltonian is given by

$$H = \begin{pmatrix} -U & \sqrt{2}\Gamma_- & \sqrt{2}\Gamma_+ \\ \sqrt{2}\Gamma_- & -U & 0 \\ \sqrt{2}\Gamma_+ & 0 & -U \end{pmatrix},$$

where Γ_+ and Γ_- were defined in Eqs. (5.16) and (5.17). Owing to the threefold degeneracy of the bare states, this Hamiltonian can easily be diagonalized. The eigenstates are given by

$$|\psi_0\rangle = \frac{1}{\sqrt{\Gamma_+^2+\Gamma_-^2}}\left(-\Gamma_+|T\rangle+\Gamma_-|S\rangle\right),$$
$$|\psi_1\rangle = \frac{1}{\sqrt{2\left(\Gamma_+^2+\Gamma_-^2\right)}}\left(-\sqrt{\Gamma_+^2+\Gamma_-^2}\,|D\rangle+\Gamma_-|T\rangle+\Gamma_+|S\rangle\right),$$
$$|\psi_2\rangle = \frac{1}{\sqrt{2\left(\Gamma_+^2+\Gamma_-^2\right)}}\left(\sqrt{\Gamma_+^2+\Gamma_-^2}\,|D\rangle+\Gamma_-|T\rangle+\Gamma_+|S\rangle\right).$$

The corresponding eigenenergies are

$$E_0 = -U,$$
$$E_1 = -U-\sqrt{2\left(\Gamma_+^2+\Gamma_-^2\right)},$$
$$E_2 = -U+\sqrt{2\left(\Gamma_+^2+\Gamma_-^2\right)}.$$

To account for an imperfect state preparation after stage I, we consider and initial state for stage II of the form $a|D\rangle+b|S\rangle$ with $|a|^2+|b|^2=1$. With this, the probability of

finding the system in the triplet state $|T\rangle$ at time t is given by

$$\mathcal{F}_T^{(\mathrm{II})}(t) = \frac{\Gamma_-^2}{\left(\Gamma_+^2+\Gamma_-^2\right)^2} \times \left\{ |a|^2 \left(\Gamma_+^2+\Gamma_-^2\right) \sin^2\left(t\sqrt{2\left(\Gamma_+^2+\Gamma_-^2\right)}\right) \right.$$
$$\left. +|b|^2\Gamma_+^2 \left[1-2\cos\left(t\sqrt{2\left(\Gamma_+^2+\Gamma_-^2\right)}\right)+\cos^2\left(t\sqrt{2\left(\Gamma_+^2+\Gamma_-^2\right)}\right)\right]\right\}. \quad (5.24)$$

Note that because only the initial state probabilities $|a|^2$ and $|b|^2$ appear in Eq. (5.24), there are no interference terms between stage I and II in the present approach. Thus we can simply obtain the triplet fidelity by multiplying the fidelities of the double occupancy (5.19) and the *ideal* triplet fidelity obtained from (5.24) by setting $a = 1$ and $b = 0$. The latter is given by

$$\mathcal{F}_T^{\mathrm{ideal}}(t) = \frac{1}{1+\left(\frac{\Gamma_+}{\Gamma_-}\right)^2} \sin^2\left(t\sqrt{2\left(\Gamma_+^2+\Gamma_-^2\right)}\right), \quad (5.25)$$

from which we immediately obtain an estimate for the ideal duration of stage II,

$$T_2 \approx (\pi/2)\left[2\left(\Gamma_-^2+\Gamma_+^2\right)\right]^{-1/2}, \quad (5.26)$$

as well as an estimate for the maximal triplet fidelity, given an initially doubly occupied QD,

$$\mathcal{F}_T^{\mathrm{ideal}} \approx \frac{1}{1+\left(\frac{\Gamma_+}{\Gamma_-}\right)^2} \approx 1-\left(\frac{U}{\Delta_Z}\right)^2. \quad (5.27)$$

An estimate for the achievable triplet fidelity in the regime $\Gamma_0 \ll U \ll \Delta_Z \ll \Delta$ is therefore obtained by multiplying the obtained fidelities in the end of each stage, Eqs. (5.21) and (5.27). This results in the triplet fidelity of Eq. (5.1),

$$\mathcal{F}_T \approx \mathcal{F}_D \mathcal{F}_T^{\mathrm{ideal}} \approx 1-\left(\frac{U}{\Delta_Z}\right)^2 - 8\left(\frac{\Gamma_0}{U}\right)^2. \quad (5.28)$$

The expression on the right hand side has a simple interpretation: The term $8(\Gamma_0/U)^2$ describes the loss of fidelity due to the competition between resonant pair tunneling and off resonant Cooper pair splitting in the first stage of the scheme. The term $(U/\Delta_Z)^2$ describes the loss of fidelity during the second stage of the scheme due to the residual spin-symmetric term in H_D that favors singlet pairing and competes with the spin antisymmetric term that favors triplet pairing.

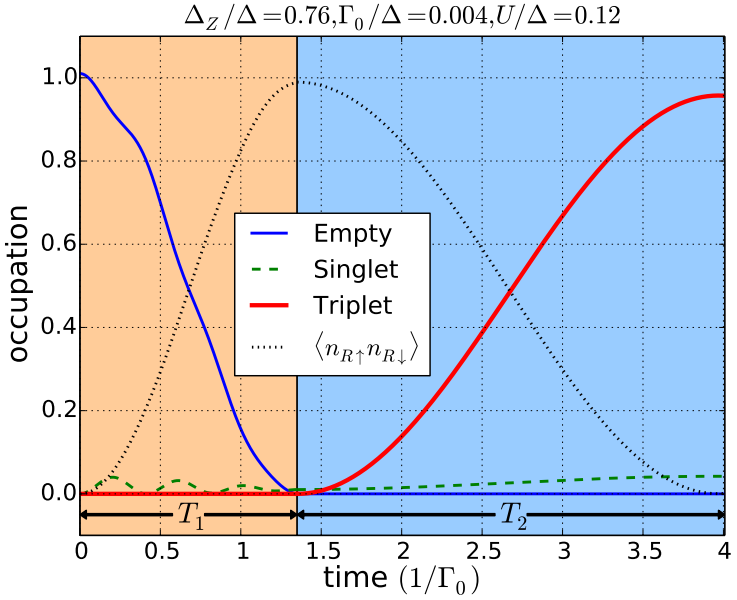

FIGURE 5.5: Analytical prediction for the dynamics of the triplet state generation for $U/\Delta = 0.12$, $\Delta_Z/\Delta = 0.76$ and $\Gamma_0/\Delta = 0.004$. This result agrees qualitatively with the full numerics shown in Fig. 5.3.

Using this analytic model, we also note that the probability for the system to be found in the doubly occupied state $|D\rangle$ at time t is given by

$$\mathcal{F}_D^{(\mathrm{II})}(t) = |a|^2 \cos^2\left(t\sqrt{2\left(\Gamma_+^2+\Gamma_-^2\right)}\right) + \frac{|b|^2}{1+\left(\frac{\Gamma_-}{\Gamma_+}\right)^2}\sin^2\left(t\sqrt{2\left(\Gamma_+^2+\Gamma_-^2\right)}\right), \quad (5.29)$$

while the probability for the system to be found in the singlet state $|S\rangle$ at time t is given by

$$\mathcal{F}_S^{(\mathrm{II})}(t) = \frac{\Gamma_+^2}{\left(\Gamma_+^2+\Gamma_-^2\right)^2} \times \left\{ |a|^2\left(\Gamma_+^2+\Gamma_-^2\right)\sin^2\left(t\sqrt{2\left(\Gamma_+^2+\Gamma_-^2\right)}\right) \right.$$
$$\left. + |b|^2\Gamma_+^2\left[\frac{\Gamma_-^4}{\Gamma_+^4} + \frac{2\Gamma_-^2}{\Gamma_+^2}\cos\left(t\sqrt{2\left(\Gamma_+^2+\Gamma_-^2\right)}\right) + \cos^2\left(t\sqrt{2\left(\Gamma_+^2+\Gamma_-^2\right)}\right)\right]\right\}. \quad (5.30)$$

We have plotted in Fig. 5.5 the occupation of the different states in stage I and in stage II using the analytical results obtained, Eqs. (5.19)-(5.30). This can be compared with Fig. 5.3.

5.6 Conclusions

In order to experimentally verify the successful generation of a non local triplet and distinguishing it from a non local singlet state, we propose two different schemes. Firstly,

the QDs could be attached to mesoscopic wires forming the inputs of an electronic beam-splitter. Depending on whether the two interfering electrons form a singlet or a triplet, the sign of the two particle interference term will differ [16, 111]. Secondly, a gate tunable direct inter-dot tunneling term makes it possible to employ the spin-blockade technique pioneered in [94, 98]. This enables a mapping from the two spin states onto two distinct charge states of one of the two QDs. The charge states can then be distinguished via a capacitively coupled rf-single electron transistor device [44, 115].

In conclusion, our work represents a first step in the investigation of the CPS beyond the infinite-U limit. We analyze effects of electron-electron interaction in the CPS in the presence or absence of a magnetic Zeeman field. We derive an analytic low-energy effective Hamiltonian for this system and identify a novel term that describes an inter-QD interaction mediated by the superconductor. We make use of this interaction and of the electrostatic tunability of the QD levels to propose a scheme to generate a non local triplet state on the two QDs. Thereby we extend the capabilities of the CPS to generate two of the four maximally entangled Bell states with high fidelities. Experimental investigations testing the validity of the presented effective low-energy model in this novel parameter regime seem feasible with current technologies and would be a very useful step towards quantum state engineering with the CPS.

CHAPTER 6

CONCLUSIONS

"Be the change you wish to see in the world"

Was not said by Gandhi. Perhaps it was said by his grandson Arun.

In most of the work presented in this thesis, we have studied the phase and amplitude dynamics of quantum self-oscillators. Specifically, we have investigated the synchronization and amplitude death phenomena in the quantum regime. First, in Ch. 2, we have found synchronization behavior which is *qualitatively* different than the synchronization behavior which is expected from a corresponding semiclassical model. Examining a quantum anharmonic van der Pol (vdP) oscillator model, we found that an external reference drive may lead to synchronization of the quantum anharmonic vdP oscillator at each of its different possible quantized oscillation frequencies. When plotting our choice of synchronization measure S as a function of the detuning Δ, Figs. 2.3 and 2.4, this was clearly observed as discrete maximas. We expect this result to be quite general, and to be present for different self-oscillators with anharmonicity in their energy spectrum. We have developed an analytical model, predicting the existence of these maximas. We have further related the occupation number of the different Fock levels to the number of apparent synchronization resonances. As a complementary view, we have shown that the frequency of the self-oscillator can be entrained by the frequency of the reference drive at the expected synchronization resonances. In addition we have demonstrated that negative densities in the steady-state Wigner function quasi-probability distribution appear for strong driving. This is another clear indication of the non-classicality of the resulting synchronized state. We believe these results could be relevant in future studies:

- Synchronization of oscillator networks: The Hilbert space of a vdP oscillator model, when operating in a very quantum parameter regime, may be truncated above the second energy level. Having such a small Hilbert space may allow for

the investigation of synchronization of oscillator networks. How will the synchronization of a harmonic oscillator network behave in comparison with the synchronization of an anharmonic oscillator network? Could we observe quantized synchronization in networks as well? A first step in that direction was taken in Ref. [78].

- Synchronization to a two-photon drive: Ref. [120] had theoretically studied the synchronization of a squeezing-driven quantum vdP oscillator. It was demonstrated that squeezing enhances synchronization in this system. Can it also enhance quantum synchronization in quantum anharmonic vdP oscillators? Will stronger synchronization resonances then be found? Will a narrower steady-state power spectrum be observed? This may allow the use of smaller values for the Kerr parameter, therefore enabling an experimental verification of this phenomenon with current optomechanical systems.

- Synchronization to a two-tone drive: In the work presented in Ch. 2, we have studied the synchronization of a self-oscillator with multiple quantized frequencies to a harmonic reference drive. One can also study the synchronization to a drive with multiple frequencies. Could the anharmonic self-oscillator exhibit simultaneous synchronization to multiple frequencies? In a semi-classical model we expect the self-oscillator to synchronize to only one of the driving frequencies, with possible transitions to other frequencies due to noise.

In Ch. 3, we have examined the amplitude death phenomenon for two coupled quantum vdP oscillators with Kerr anharmonicity in their energy spectrum. We have first demonstrated that the anharmonicity suppresses the oscillation amplitude in the presence of noise. We have shown that this suppression is not accounted for in a classical noiseless model, and we have further shown *quantitative* differences in the strength of this suppression between a quantum model and a semiclassical noisy model. Then, as in Ch. 2, we have found a behavior in the amplitude death phenomenon which is *qualitatively* different from the behavior expected when using a corresponding semiclassical model. This was reflected as quantized resonances in the mean phonon number of the oscillators, which are not seen in the corresponding semiclassical model. These resonances appeared for frequency detunings which match relevant transition frequencies in the energy spectrum of the anharmonic vdP oscillators. To the best of our knowledge, this is the first time that genuine quantum effects are discussed in the context of the amplitude death phenomenon. An interesting direction for future investigations:

- Amplitude death of oscillator networks: As is seen by comparing Fig. 3.5 to Fig. 3.6, the phonon number peaks are more pronounced when one of the self-oscillators is harmonic. It will be interesting to examine oscillator networks, in which multiple harmonic oscillators and one anharmonic oscillator are present. Will the anharmonic oscillator still lead to quantized amplitude death? Could the many resonances become almost equal in magnitude to the single resonance appearing when only harmonic oscillators are dissipatively coupled?

In the work presented in Ch. 4, we have studied the synchronization of an optomechanical system to two different drives: (1) An optical drive, applied onto the electromagnetic cavity; (2) A mechanical drive, applied onto the mechanical oscillator. For both these cases, we used the master equation as our starting point, applied the laser theory for optomechanical limit cycles [79], and have obtained an analytical description of the emerging synchronization, which is contained in an Adler equation. In the process of doing so, we have also obtained Fokker-Planck equations describing the dynamics of the self-oscillator for these two cases. This description was valid in a classical parameter regime. We then demonstrated using numerical exact simulations that synchronization is expected also in a quantum parameter regime. A future use of this work may be:

- Noise-reduction for the mechanical self-oscillator: In the Fokker-Planck equation obtained, Eq. (4.45), the additional laser drive appears as terms in the diffusion coefficients. It will be interesting to use this analytical description to explore noise-reduction in the radial direction, therefore stabilizing the amplitude of the self-oscillator, or in the tangential direction, hoping to achieve a better signal-to-noise ratio for the synchronization.

While our work presented in Chs. 2-4 has dealt with self-oscillators demonstrating an almost circular limit-cycle in phase-space, an interesting direction of future research in the study of phase and amplitude dynamics of quantum self-oscillators may be in the direction of relaxation oscillators:

- Relaxation oscillators produce a non-sinusoidal repetitive output signal, such as a triangle wave or a square wave (this is indeed captured by the classical equation for the vdP oscillator, Eq. (1.2)). Brain neurons and fireflies are examples of relaxation oscillators. Constructing a quantum model for such an oscillator had never been done, and may help to advance our understanding of quantum self-oscillators. If this mission could be accomplished, many research questions may follow: Could quantum relaxation oscillators synchronize? What is the effect of quantum noise? How about networks of relaxations oscillators?

In Ch. 5 of this thesis, we have investigated the Cooper pair splitter beyond the Coulomb blockade approximation. We have analytically derived a low-energy effective Hamiltonian for this system, describing the allowed transport processes. These include Cooper pair splitting, Cooper pair tunneling, and an inter-quantum dot (QD) interaction which is mediated by the superconductor. We have made use of this interaction, together with the electrostatic tunability of the QD levels and an in-plane magnetic field, and proposed a scheme to generate a non local triplet state on the two QDs. We have numerically and analytically demonstrated that this triplet state could be generated with high fidelity. This research therefore extends the capabilities of the Cooper pair splitter to generate two of the four maximally entangled Bell states.

APPENDIX A

NUMERICAL METHODS

"There's a sucker born every minute"

Adam Forepaugh (not P. T. Barnum)

In each work presented in this thesis, we have used numerical simulations. These simulation were employed for different reasons: (1) Obtaining exact numerical results was used to test analytical approximations, approving the used analytical approach (Ch. 2, Ch. 4 and Ch. 5); (2) Using numerical methods allowed us to deal with problems for which an analytical treatment was not possible (Ch. 3); (3) Some problems were analytically accessible in some parameter regime, but not in another (Ch. 2, Ch. 4). Numerical simulations were used to explore the parameter regime in a more complete manner.

In this appendix, it is our goal to clearly explain the numerical code used in Chapters 3-5. It is our hope that it should help future researchers exploring the themes covered in this thesis. Explaining the numerical principles of simulating open quantum systems, of numerically solving complex-valued differential equations, and of simulating stochastic processes is not within the scope of this appendix. For thorough explanations regarding these topics, the reader is refered to Refs. [60, 61, 67, 123].

The numerical simulations were mostly coded in the high-level programming `python` language. We have further used the open-source computational toolbox for quantum optics, `QuTiP` [60, 61], since it offers easy-to-use, quick-to-handle, and simple commands to define Hamiltonians and Lindblad operators. It further allows for simulating the time-evolution of systems defined via these operators. Additionaly, standard packages of `python` were used: `numpy`, `scipy` and `matplotlib`. We have also used `Mathematica` in numerical simulations performed in Ch. 3.

Throughout this appendix, when using the scripting language `python`, we have used the `QuTiP` and `numpy` packages, which were imported as

```
from qutip import *
import numpy as np
```

A.1 Numerics of Chapter 3

Quantum Model

The parameters of the system can then be easily defined,

```
Dc = ? # Hilbert space dimensions for one oscillator.
omega1 = ? # Natural oscillation frequency of 1st oscillator.
omega2 = ? # Natural oscillation frequency of 2nd oscillator.
K1 = ? # Kerr nonlinearity of 1st oscillator.
K2 = ? # Kerr nonlinearity of 2nd oscillator.
G = ? # Energy gain rate.
kappa = ? # Energy decay rate.
V = ? # Strength of dissipative coupling
```

One can then define the relevant operators, which describe a system of two dissipatively coupled vdP oscillators with Kerr nonlinearities in their energy spectrum,

```
a1 = tensor(destroy(Dc), qeye(Dc)) # Annihilation operator for 1st oscillator.
a2 = tensor(qeye(Dc), destroy(Dc)) # Annihilation operator for 2nd oscillator.

H = omega1*a1.dag()*a1 + omega2*a2.dag()*a2 # Hamiltonian
        +K1*(a1.dag()*a1*a1.dag()*a1)+K2*(a2.dag()*a2*a2.dag()*a2)

c_ops = [] #Lindblad operators
c_ops.append(np.sqrt(G)*a1.dag()) # Linear energy gain - 1st oscillator.
c_ops.append(np.sqrt(G)*a2.dag()) # Linear energy gain -  2nd oscillator.
c_ops.append(np.sqrt(kappa)*a1**2) # Nonlinear energy loss - 1st oscillator.
c_ops.append(np.sqrt(kappa)*a2**2) # Nonlinear energy loss - 2nd oscillator.
c_ops.append(np.sqrt(V)*(a1 - a2)) # Dissipative coupling.
```

In the work done in Ch. 3, we have always solved for the steady state of the system. Implementing it in `QuTiP` is extremely simple,

```
rho_ss = steadystate(H, c_ops) # Solve for steady state density matrix
```

Using the steady state density matrix, obtaining the wanted expectation value is done via

```
? = expect(?, rho_ss)# Obtain expectation value for operator '?'
```

Using this simple code is enough to reproduce all quantum simulation results of Ch. 3.

Classical Model

When numerically simulating the classical model, Eq. (3.2), one needs to solve a system of complex-valued coupled differential equations. After defining the parameters of the system (done in the same manner as for the quantum model), solving our equation is done using

```
def odeintz(func, z0, t, **kwargs):
    """An odeint-like function for complex valued differential equations."""

    # Make sure z0 is a numpy array of type np.complex128.
    z0 = np.array(z0, dtype=np.complex128, ndmin=1)

    def realfunc(x, t, *args):
        z = x.view(np.complex128)
        dzdt = func(z, t, *args)
        # func might return a python list, so convert its return
        # value to an array with type np.complex128, and then return
        # a np.float64 view of that array.
        return np.asarray(dzdt, dtype=np.complex128).view(np.float64)

    # Standard 'odeint' to solve real-valued coupled differential equations.
    result = odeint(realfunc, z0.view(np.float64), t, **kwargs)

    if kwargs.get('full_output', False):
        z = result[0].view(np.complex128)
        infodict = result[1]
        return z, infodict
    else:
        z = result.view(np.complex128)
        return z


if __name__ == "__main__":

# Define the right-hand-side of the differential equation.
def zfunc(z, t):
alpha1, alpha2 = z
return [-1j*(omega1+K1*(np.abs(alpha1)**2 + 1))* alpha1+(G/2)*alpha1-
                  (kappa)*np.abs(alpha1)**2*alpha1+(V/2)*(alpha2-alpha1)
          , -1j * (omega2+K2*(np.abs(alpha2)**2 + 1)) * alpha2 + (G/2)*alpha2-
                  (kappa)*np.abs(alpha2)**2*alpha2+(V/2)*(alpha1-alpha2)]

# Set up the inputs and call odeintz to solve the system.
 z0 = np.array([0.01+0.0j, 0.01+0.0j])

t_f = 300 # final time.
t_points = 1000 # number of points in the time grid.
t = np.linspace(0, t_f, t_points)
```

```
z, infodict = odeintz(zfunc, z0, t, full_output=True)
```

In the last code, the complex-valued differential equations are replaced with real-valued differential equations in the user defined `odeintz` function. This function then uses the standard differential equation solver `odeint`. Our classical equations, Eq. (3.2), are defined using a function `zfunc`. The initial conditions are given using `z0`, and the time grid is defined in the variable `t`.

Semiclassical Model

To numerically simulate the semiclassical Langevin equation, Eq. (3.10), we have used `Mathematica`. We start by defining a function for the drift vector $\boldsymbol{\mu}$

```
defineMuVec[omega1_, omega2_, G_, kappa_, V_, K1_, K2_]:= Module[{},
# Dirft vector x1, y1, x2 and y2 components:
mux1 = (omega1 + K1(2(x1**2+y1**2)))*y1
                        + (G/2-kappa(x1**2+y1**2-1)-V/2)*x1+V/2*x2;
muy1 = -(omega1 + K1(2(x1**2+y1**2)))*x1
                        + (G/2-kappa(x1**2+y1**2-1)-V/2)*y1+V/2*y2;
mux2 = (omega2 + K2(2(x2**2+y2**2)))*y2
                        + (G/2-kappa(x2**2+y2**2-1)-V/2)*x2+V/2*x1;
muy2 = -(omega2 + K2(2(x2**2+y2**2)))*x2
                        + (G/2-kappa(x2**2+y2**2-1)-V/2)*y2+V/2*y1;
mu = {mux1, muy1, mux2, muy2} # Returns vector mu
mu]
```

and a function for the noise matrix $\boldsymbol{\sigma}$

```
defineSigmaMat[omega1_, omega2_, G_, kappa_, V_]:= Module[{},
# Dirft vector x1, y1, x2 and y2 components:
nu1 = G/2 + kappa(2(x1**2 + y1**2)-1) + V/2;
nu2 = G/2 + kappa(2(x2**2 + y2**2) -1) + V/2;
uplus = -(nu1 - nu2 + ((nu1 - nu2)**2 + V**2)**(1/2)) /V;
uminus = -(nu1 - nu2 - ((nu1 - nu2)**2 + V**2)**(1/2)) /V;
lambdaplus = (nu1 + nu2 + ((nu1 - nu2)**2 + V**2)**(1/2) /4;
lambdaminus = (nu1 + nu2 - ((nu1 - nu2)**2 + V**2)**(1/2) /4;
sigmaMat = ((lambdaplus)**(1/2)/(uplus-uminus)){
        {uplus-uminus*(lambdaminus/lambdaplus)**(1/2), 0,
                        1 - (lambdaminus/lambdaplus)**(1/2), 0}
        {0, uplus-uminus*(lambdaminus/lambdaplus)**(1/2),
                        0, 1 - (lambdaminus/lambdaplus)**(1/2)}
        {1-(lambdaminus/lambdaplus)**(1/2), 0,
                        uplus*(lambdaminus/lambdaplus)**(1/2)-uminus, 0}
        {0, 1-(lambdaminus/lambdaplus)**(1/2),
                        0, uplus*(lambdaminus/lambdaplus)**(1/2)-uminus}
};
sigmaMat]
```

The Langevin equation itself is defined via the function

```
defineItoProcess[mu, sigmaMat]:= Module[{},
proc = ItoProcess[
\[DifferentialD]x1[t]==mu[[1]]\[DifferentialD]t +
      (sigmaMat[[1,1]] + sigmaMat[[1,2]] + sigmaMat[[1,3]] + sigmaMat[[1,4]])
                \[DifferentialD]w1[t],
\[DifferentialD]y1[t]==mu[[2]]\[DifferentialD]t +
      (sigmaMat[[2,1]] + sigmaMat[[2,2]] + sigmaMat[[2,3]] + sigmaMat[[2,4]])
                \[DifferentialD]w2[t],
\[DifferentialD]x2[t]==mu[[3]]\[DifferentialD]t +
      (sigmaMat[[3,1]] + sigmaMat[[3,2]] + sigmaMat[[3,3]] + sigmaMat[[3,4]])
                \[DifferentialD]w3[t],
\[DifferentialD]x2[t]==mu[[1]]\[DifferentialD]t +
      (sigmaMat[[4,1]] + sigmaMat[[4,2]] + sigmaMat[[4,3]] + sigmaMat[[4,4]])
                \[DifferentialD]w4[t],
{x1[t]**2, y1[t]**2, x2[t]**2, y2[t]**2},
{{x1, y1, x2, y2}, {x1_0, y1_0, x2_0, y2_0}}, t,
{w1 = WienerProcess[], w2 = WienerProcess[],
                                  w3 = WienerProcess[], w4 = WienerProcess[]}
];
proc];
```

where the solution will be found for the square of the x and y coordinates, i.e. for $x_1^2(t), y_1^2(t), x_2^2(t), y_2^2(t)$, and the initial conditions should be defined by specifying the appropriate value for $x_1(0), y_1(0), x_2(0), y_2(0)$. To obtain realizations of this stochastic process, we use the functions just defined in the following manner:

```
mu = defineMuVec[];
sigmaMat = defineSigmaMat[];
process = defineItoProcess[mu, sigmaMat];
fTime = ?;
stepSize = ?;
numPaths = ?;
realization = RandomFunction[process, {0., fTime, stepSize}, numPaths];
```

In the last piece of code, the command `RandomFuncion` generates $n =$ `numPaths` random realizations of `process`, from time $t = 0$ to $t =$ `fTime`, using a time step `stepSize`. In Ch. 3 we have used this code on several occasions. On each occasion, different physical parameters were used. This difference in physical parameters led to a different choice of numerical parameters . This varying choices of numerical parameters, used for the different plots appearing in Ch. 3, are summarized in the following table:

Parameters used in Ch. 3			
Figure name	'fTime'	'stepSize'	'numPaths'
Fig. 3.2, $V = \{2, 4, 6, 8, 10\}$	20.0	$5 * 10^{-5}$	1500
Fig. 3.5, $V = 2$	1.0	$5 * 10^{-6}$	60000
Fig. 3.5, $V = 8$	2.0	10^{-5}	6000
Fig. 3.6, $V = 2$	0.2	10^{-6}	60000
Fig. 3.6, $V = 8$	2.0	$5 * 10^{-6}$	6000

Because of the large number of trajectories involved, and the large number of time steps, the numerical calculations were performed at sciCORE (http://scicore.unibas.ch/) scientific computing core facility at University of Basel. Finally, to obtain the radius of oscillation from the many realizations, we use

```
r = TimeSeriesThread[Mean, realization][``ValueList''][[1]][[All,1]]
        + TimeSeriesThread[Mean, realization][``ValueList''][[1]][[All,2]];
radius = Mean[r[[Floor[Fraction*fTime/stepSize];;Floor[fTime/stepSize]]]];
```

where the variable `Fraction` should be chosen such as to keep only this part of `r` for which the system is already in the steady state.

A.2 Numerics of Chapter 4

In this section, we would like to describe the code used to obtain the results which are described in Ch. 4. Let us first define a few parameters and operators, which would be used later on in the suggested code,

```
H          # Full Hamiltonian.
H0         # Hamiltonian with no additional external drive.
c_op_list  # List of collapse operators
omega_e    # Frequency of additional external drive.
acc        # Accuracy to accept quasi-steady state (see below).
Initial    # Initial state.
ppc        # points per cycle.
tnc        # Number of cycles to evolve.
NP         # Number of points.
N_opt      # Number of optical Fock states
N_mech     # Number of mechanical Fock states
```

Now, as discussed in Sec. 4.4, the system does not reach a steady state, but a time-periodic quasi-steady state. That means, that in the quasi-steady state, the expectation value of some operator $\langle b \rangle$, for example, should fulfill $\langle b(t) \rangle = \langle b(t+T) \rangle$, with $T =$

$1/\omega_e^{op,m}$ being the periodicity. To make sure the system has reached the quasi-steady state, we let the system evolve a time $t = T$ using the function

```
def evolve_one_cycle(H, c_op_list, omega_e, Initial):
        NP = 200
        time_list = np.linspace(0, 2*np.pi/np.abs(omega_e), NP)
        result_one_cycle = mesolve(H,Initial,
                                   time_list, c_op_list, [],args=args)
        Initial = result_one_cycle.states[-1] # Last state
        b_expect = expect(b, result_one_cycle.states[-1]) # Last <b>
        return (Initial, b_expect)
```

and then check if $\langle b(t)\rangle = \langle b(t+T)\rangle$ holds (up to some given accuracy). If it is indeed so, we have reached the quasi-steady state. The whole process is captured by the following function

```
def evolve_until_steady_state(H, H0, c_op_list, omega_e, acc):
        psi0_temp = steadystate(H0, c_op_list)
                        # Initial state for the calculation.
        b_exp = []; count = 0; count_cycles = 0;
        while (count<15):
                (psi0_temp, b_temp) = evolve_one_cycle(H
                                    , c_op_list, omega_e, psi0_temp)
                count_cycles = count_cycles + 1
                b_exp.append(b_temp)
                if (count_cycles > 2):
                        if (np.abs(np.real(b_exp[-1]-b_exp[-2]))<acc):
                                count = count + 1
                        else:
                                count = 0
        print('The quasi-steady state begin after %s cycles' % (count_cycles))
        return(psi0_temp) #  quasi-steady state.
```

Using the last two functions, it is easy to reproduce Fig. 4.2. After reaching the quasi-steady state, we would like to calculate the time-average synchronization measure $\bar{S}$, as shown in Figs. 4.5-4.7. The first stage is therefore obtaining a structure containing the states of the system over a period T. This is easily done in `QuTiP`,

```
(psi0_qss) = evolve_until_steady_state(H, H0, c_op_list, omega_e, acc)
times = np.linspace(0.0, 2*np.pi*tnc/omega_e, ppc*t_number_cycles)
result_state = mesolve(H, psi0_qss, times,  c_op_list, [],args=args)
```

Now, as further described ins Sec. 4.4, we need to displace the resulting states by β_c. This is done via the defined function

```
def shift_quantum_object(Result_State):
    (beta_c, rho_steadystate)=beta_shift (H0, c_op_list)
    D = tensor(qeye(N_opt),displace(N_mech, -beta_c))
    Result_State_Copy = copy.deepcopy(Result_State)
    for i in range(len(Result_State_Copy.states)):
        Result_State_Copy.states[i] = D* Result_State_Copy.states[i] * D.dag().
    return Result_State_Copy
```

which shifts all density matrices appearing in a quantum object of `QuTiP` type `result.states`. The synchronization measure S can be calculated using

```
def S1_SS(result_State):
    test=np.abs(expect(b,result_State))/np.sqrt(expect(b_dag*b,result_State))
    return test
```

We would like to calculate S for each state in appearing in our structure of `QuTiP` type `result.states`, and then average. This is achieved via

```
S_Temporal = np.zeros(ppc)
for NS in range(0, ppc):
        S_Temporal[NS] = S1_measure(shifted_result_state.states[NS])
S_Final = np.average(S_Temporal)
```

Of course, in order to obtain Figs. 4.5-4.7, this suggested algorithm should be repeated many times. We have therefore parallelized the computation, using a different core at sciCORE (http://scicore.unibas.ch/) scientific computing core facility at University of Basel, for each specific $\bar{S}$ value.

Obtaining Figs. 4.3-4.4 is rather straightforward, as we have specific form for the analytical predictions. Simulating Eqs. (4.62)-(4.65) can be done using the differential equation integrator we have introduced in Sec. A.1.

A.3 Numerics of Chapter 5

In the following, we shall present the code used to numerically simulate the Schrödinger equation which time-evolves according to the effective low-energy Hamiltonian, Eq. (5.10). The operators acting on a single QD are defined as a Class instance using `QuTiP` as

```
import qutip as q
import numpy as np

class OpDot:
```

```
    # Identity operator
    I0 = q.tensor(q.qeye(2), q.qeye(2))

    # Fermionic creation and annihilation operators
    cU = q.tensor(q.destroy(2), q.qeye(2))
    cD = q.tensor(q.qeye(2), q.destroy(2))
    cUd = cU.dag()
    cDd = cD.dag()

    # Number operators
    nU = cUd * cU
    nD = cDd * cD

    # Several electron states
    sEmpty = q.tensor(q.basis(2, 0), q.basis(2, 0))
    sU = q.tensor(q.basis(2, 1), q.basis(2, 0))
    sD = q.tensor(q.basis(2, 0), q.basis(2, 1))
    sDouble = q.tensor(q.basis(2, 1), q.basis(2, 1))

    # Projection operators
    pEmpty = sEmpty * sEmpty.dag()
```

We can then move further to define a Class instance for the operators which act on the Hilbert space of the double QDs,

```
class OpDoubleDot:

    QD1 = OpDot()
    QD2 = OpDot()

    # Identity operator
    I0 = q.tensor(QD1.I0, QD2.I0)

    # Fermionic creation and annihilation operators.
    # We use the Jordan-Wigner transform to enforce proper anti-commutation
    c1U = q.tensor(QD1.cU, QD2.I0)
    c1Ud = c1U.dag()
    c1D = q.tensor(QD1.cD, QD2.I0)
    c1D = c1D * (-1j*np.pi*c1Ud*c1U).expm()
    c1Dd = c1D.dag()
    c2U = q.tensor(QD1.I0, QD2.cU)
    c2U = c2U * (-1j*np.pi*(c1Ud*c1U + c1Dd*c1D)).expm()
    c2Ud = c2U.dag()
    c2D = q.tensor(QD1.I0, QD2.cD)
    c2D = c2D * (-1j*np.pi*(c1Ud*c1U + c1Dd*c1D + c2Ud*c2U)).expm()
    c2Dd = c2D.dag()

    # Number operators
    n1U = q.tensor(QD1.nU, QD2.I0)
    n1D = q.tensor(QD1.nD, QD2.I0)
    n2U = q.tensor(QD1.I0, QD2.nU)
    n2D = q.tensor(QD1.I0, QD2.nD)

    # Several electron states
    sEmpty = q.tensor(QD1.sEmpty, QD2.sEmpty)
    sSinglet = 1/np.sqrt(2) * (c1Ud * c2Dd - c1Dd * c2Ud) * sEmpty
```

```
    sTriplet0 = 1/np.sqrt(2) * (c1Ud * c2Dd + c1Dd * c2Ud ) * sEmpty
    sTripletp = (c1Dd * c2Dd) * sEmpty
    sTripletm = (c1Ud * c2Ud) * sEmpty
    sTripletSameDot = (c1Ud * c2Ud) * sEmpty
    sSingletSameDot = (c2Ud * c2Dd) * sEmpty
    sDoubleDot1 = (c1Ud * c1Dd) * sEmpty

    # Projectors
    pSinglet = sSinglet * sSinglet.dag()
    pTriplet0 = sTriplet0 * sTriplet0.dag()
    pTripletp = sTripletp * sTripletp.dag()
    pTripletm = sTripletm * sTripletm.dag()
    pEmpty = sEmpty * sEmpty.dag()
```

The parameters for the numerical simulation are defined via

```
class Para:

    class Times:
        # Simulation times
        tInitial = 0.0
        T1 = 62.5
        T2 = 200.0
        tStep = 0.01
        tEvalStep = 5

    class DotHH:
        # Parameters for the "heavy hole band",
        # i.e., the dot levels which absorb the split Cooper pair
        Delta = 1.0   # that is the scale for all parameters.
                      # Therefore DeltaZ=0.01 means 1/100 of Delta.
        MuL = ?       # On-site energy of left dot
        MuR = 0.0     # On-site energy of right dot
        DeltaZ = ?    # Zeeman splitting
        U = ?         # Charging energy of the left dot
        GammaC = 0.01 # Half the value which is given in the paper

    class DriveDip:
        # Parameters related to the drive due to the change of chemical
        # potential which fills the heavy hole band with a split Cooper pair
        ADriveL = -0.2
        ADriveR = 0.0
        alphaDrive = 100.00
        DriveFuncL = 'ADriveL*(1 + tanh(alphaDrive*(t-tStartDrive)))/2.0'
        DriveFuncR = 'ADriveR*(1 + tanh(alphaDrive*(t-tStartDrive)))/2.0'
```

Please note that using `ADriveR` $= 0.0$ sets the driving of the chemical potential of the right QD to zero. This is important for the transition between the first and second phase of the triplet generating scheme. The time-dependence of the driving of the chemical potential of the left QD is given by `DriveFuncL`. Now we can finally define the low-energy Hamiltonian,

```
# Shortcut for the heavy-hole band parameters and the
# corresponding quantum operators for the double dot system
op = self.op = OpDoubleDot()
# Shortcuts for the Hamitlonian parameters
D = Para.DotHH.Delta
DZ = Para.DotHH.DeltaZ
UL = Para.DotHH.U
UR = Para.DotHH.U
MuL = Para.DotHH.MuL
MuR = Para.DotHH.MuR
GammaC = Para.DotHH.GammaC

# Define the Hamiltonian for the onsite energies
h0_left = (MuL + DZ/2) * op.n1U + (MuL - DZ/2) * op.n1D + UL * op.n1U * op.n1D
h0_right =(MuR + DZ/2) * op.n2U + (MuR - DZ/2) * op.n2D + UR * op.n2U * op.n2D

# Define the Hamiltonian for the proximity terms:
# Cooper pair splitting
h_prox = q.Qobj(
        GammaC * (1.0/np.sqrt(1.0-(DZ/(2*D))**2)*(2.0-op.n1D-op.n2U)
                + 1.0/np.sqrt(1.0-((DZ/2+UL)/D)**2)*op.n1D
                + 1/np.sqrt(1-((DZ/2-UR)/D)**2)*op.n2U)
                                *op.c2Dd * op.c1Ud
        - GammaC * (1/np.sqrt(1-(DZ/(2*D))**2)*(2- op.n1U - op.n2D)
                + 1/np.sqrt(1-((DZ/2 - UL)/D)**2)*op.n1U
                + 1/np.sqrt(1-((DZ/2+UR)/D)**2)*op.n2D)
                                * op.c2Ud * op.c1Dd
                )
# Tunneling to the same dot
h_prox += GammaC*(1.0/np.sqrt(1.0-(DZ/(2*D))**2)
          +(0.5+np.arctan(((DZ/2+UR)/D)/np.sqrt(1-((DZ/2+UR)/D)**2))/np.pi)
                                        /np.sqrt(1-((DZ/2+UR)/D)**2)
          +(0.5-np.arctan(((DZ/2-UR)/D)/np.sqrt(1-((DZ/2-UR)/D)**2))/np.pi)
                                        /np.sqrt(1.0-((DZ/2-UR)/D)**2))
                                                * op.c2Dd * op.c2Ud
        + GammaC * (1/np.sqrt(1.0-(DZ/(2*D))**2)
        + (0.5+np.arctan(((DZ/2+UL)/D)/np.sqrt(1-((DZ/2+UL)/D)**2))/np.pi)
                                        /np.sqrt(1-((DZ/2+UL)/D)**2)
        + (0.5-np.arctan(((DZ/2-UL)/D)/np.sqrt(1-((DZ/2-UL)/D)**2))/np.pi)
                                        /np.sqrt(1-((DZ/2-UL)/D)**2))
                                                * op.c1Dd * op.c1Ud
# Tunneling from one dot to the other
h_prox += GammaC*(DZ/2.0/np.sqrt(D**2-(DZ/2)**2)*(2.0-op.n1D-op.n2D)
                +(DZ/2.0+UL)/np.sqrt(D**2-(DZ/2+UL)**2)*op.n1D
                +(DZ/2.0+UR)/np.sqrt(D**2 -(DZ/2+UR)**2)*op.n2D)
                                * op.c2Ud * op.c1U
        - GammaC * (DZ/2/np.sqrt(D**2-(DZ/2)**2)*(2.0-op.n1U-op.n2U)
                +(DZ/2-UL)/np.sqrt(D**2-(DZ/2-UL)**2)*op.n1U
                +(DZ/2-UR)/np.sqrt(D**2-(DZ/2-UR)**2)*op.n2U)
                                * op.c2Dd * op.c1D
# add the h.c. terms
h_prox = h_prox + h_prox.dag()

# Construct the full time-independent Hamiltonian
h = h0_right + h0_left + h_prox

# Time-dependent parts of the Hamiltonian
h_time_left = op.n1U + op.n1D
h_time_right = op.n2U + op.n2D
```

```
self.hamiltonian = [h, [h_time_left, Para.DriveDip.DriveFuncL],
                                [h_time_right, Para.DriveDip.DriveFuncR]]
```

The time-dependent part of the Hamiltonian is just the detuning of the chemical potential at the transition between the first phase and second phase of our scheme, starting about $t = T_1$. The time evolution of the system can then be calculated using the function,

```
def time_evolution(self, initial_state=OpDoubleDot.sEmpty):
        times = np.arange(Para.Times.tInitial, Para.Times.T1 +
                                        Para.Times.T2, Para.Times.tStep)
        args = {
        'ADriveL': Para.DriveDip.ADriveL,
        'ADriveR': Para.DriveDip.ADriveR,
        'alphaDrive': Para.DriveDip.alphaDrive,
        'tStartDrive': Para.Times.T1,
        }

        sol = q.sesolve(self.hamiltonian, initial_state, times, [], args=args)
        return sol
```

The quantum object `sol` contains all the information regarding the time evolution of the system. Using it, one can easily obtain the occupation of the different states as a function of time, and therefore reproduce Fig. 5.3 for example. The process described here can be performed for different parameters. Varying Δ_Z and U, in particular, allows one to reproduce Fig. 5.4.

BIBLIOGRAPHY

[1] Ameri, V., Eghbali-Arani, M., Mari, A., Farace, A., Kheirandish, F., Giovannetti, V., and Fazio, R. (2015). Mutual information as an order parameter for quantum synchronization. *Phys. Rev. A*, **91**:012301.

[2] Amitai, E., Koppenhöfer, M., Lörch, N., and Bruder, C. (2018). Quantum effects in amplitude death of coupled anharmonic self-oscillators. *Phys. Rev. E*, **97**:052203.

[3] Amitai, E., Lörch, N., Nunnenkamp, A., Walter, S., and Bruder, C. (2017). Synchronization of an optomechanical system to an external drive. *Phys. Rev. A*, **95**:053858.

[4] Amitai, E., Tiwari, R. P., Walter, S., Schmidt, T. L., and Nigg, S. E. (2016). Nonlocal quantum state engineering with the Cooper pair splitter beyond the Coulomb blockade regime. *Phys. Rev. B*, **93**:075421.

[5] Armour, A. D. and Rodrigues, D. A. (2012). Quantum dynamics of a mechanical resonator driven by a cavity. *C. R. Phys.*, **13**:440.

[6] Aronson, D. G., Ermentrout, G. B., and Kopell, N. (1990). Amplitude response of coupled oscillators. *Physica D*, **41**:403.

[7] Aspect, A., Dalibard, J., and Roger, G. (1982). Experimental test of Bell's inequalities using time- varying analyzers. *Phys. Rev. Lett.*, **49**:1804.

[8] Aspelmeyer, M., Kippenberg, T. J., and Marquardt, F. (2014). Cavity optomechanics. *Rev. Mod. Phys.*, **86**:1391.

[9] Bagheri, M., Poot, M., Fan, L., Marquardt, F., and Tang, H. X. (2013). Photonic cavity synchronization of nanomechanical oscillators. *Phys. Rev. Lett.*, **111**:213902.

[10] Balanov, A., Janson, N., Postnov, D., and Sosnovtseva, O. (2009). *Synchronization: from simple to complex*. Springer.

[11] Bar-Eli, K. (1984). Coupling of chemical oscillators. *J. Phys. Chem.*, **88**:3616.

[12] Bastidas, V. M., Omelchenko, I., Zakharova, A., Schöll, E., and Brandes, T. (2015). Quantum signatures of chimera states. *Phys. Rev. E*, **92**:062924.

[13] Bell, J. S. (1964). On the Einstein-Podolsky-Rosen paradox. *Physics*, **1**:195.

[14] Bouwmeester, D., Pan, J.-W., Mattle, K., Eibl, M., Weinfurter, H., and Zeilinger, A. (1997). Experimental quantum teleportation. *Nature*, **390**:575.

[15] Breuer, H.-P. and Petruccione, F. (2002). *The Theory of Open Quantum Systems*. Oxford University Press.

[16] Burkard, G., Loss, D., and Sukhorukov, E. V. (2000). Noise of entangled electrons: Bunching and antibunching. *Phys. Rev. B*, **61**:R16303.

[17] Buters, F. M., Eerkens, H. J., Heeck, K., Weaver, M. J., Pepper, B., de Man, S., and Bouwmeester, D. (2015). Experimental exploration of the optomechanical attractor diagram and its dynamics. *Phys. Rev. A*, **92**:013811.

[18] Carmele, A., Kabuss, J., Schulze, F., Reitzenstein, S., and Knorr, A. (2013). Single photon delayed feedback: A way to stabilize intrinsic quantum cavity electrodynamics. *Phys. Rev. Lett.*, **110**:013601.

[19] Carmichael, H. (1999). *Statistical Methods in Quantum Optics 1: Master Equations and Fokker-Planck Equations*. Springer.

[20] Carmon, T., Rokhsari, H., Yang, L., Kippenberg, T. J., and Vahala, K. J. (2005). Temporal behavior of radiation-pressure-induced vibrations of an optical microcavity phonon mode. *Phys. Rev. Lett.*, **94**:223902.

[21] Chan, C.-K., Lee, T. E., and Gopalakrishnan, S. (2015). Limit-cycle phase in driven-dissipative spin systems. *Phys. Rev. A*, **91**:051601.

[22] Chan, J., Alegre, T. P. M., Safavi-Naeini, A. H., Hill, J. T., Krause, A., Groblacher, S., Aspelmeyer, M., and Painter, O. (2011). Laser cooling of a nanomechanical oscillator into its quantum ground state. *Nature*, **478**:89.

[23] Chevallier, D., Rech, J., Jonckheere, T., and Martin, T. (2011). Current and noise correlations in a double-dot Cooper-pair beam splitter. *Phys. Rev. B*, **83**:125421.

[24] Chiaverini, J. and Sage, J. M. (2014). Insensitivity of the rate of ion motional heating to trap-electrode material over a large temperature range. *Phys. Rev. A*, **89**:012318.

[25] Choi, M.-S., Bruder, C., and Loss, D. (2000). Spin-dependent Josephson current through double quantum dots and measurement of entangled electron states. *Phys. Rev. B*, **62**:13569.

[26] Clerk, A. A., Devoret, M. H., Girvin, S. M., Marquardt, F., and Schoelkopf, R. J. (2010). Introduction to quantum noise, measurement, and amplification. *Rev. Mod. Phys.*, **82**:1155.

[27] Das, A., Ronen, Y., Heiblum, M., Mahalu, D., Kretinin, A. V., and Shtrikman, H. (2012). High-efficiency Cooper pair splitting demonstrated by two-particle conductance resonance and positive noise cross-correlation. *Nat. Commun.*, **3**:1165.

[28] Davis-Tilley, C. and Armour, A. D. (2016). Synchronization of micromasers. *Phys. Rev. A*, **94**:063819.

[29] Deacon, R. S., Oiwa, A., Sailer, J., Baba, S., Kanai, Y., Shibata, K., Hirakawa, K., and Tarucha, S. (2015). Cooper pair splitting in parallel quantum dot Josephson junctions. *Nat. Commun.*, **6**:7446.

[30] Diehl, S., Micheli, A., Kantian, A., Kraus, B., Büchler, H. P., and Zoller, P. (2008). Quantum states and phases in driven open quantum systems with cold atoms. *Nat. Phys.*, **4**:878.

[31] DiVincenzo, D. P. (1995). Quantum computation. *Science*, **270**:255.

[32] Dodonov, V. V. and Mizrahi, S. S. (1997). Exact stationary photon distributions due to competition between one- and two-photon absorption and emission. *J. Phys. A. Math. Gen.*, **30**:5657.

[33] Droste, S., Andergassen, S., and Splettstoesser, J. (2012). Josephson current through interacting double quantum dots with spin–orbit coupling. *J. Phys. Condens. Matter*, **24**:415301.

[34] Drummond, P. D. and Walls, D. F. (1980). Quantum theory of optical bistability. I. Nonlinear polarisability model. *J. Phys. A. Math. Gen.*, **13**:725.

[35] Dykman, M. (2012). *Fluctuating Nonlinear Oscillators: From Nanomechanics to Quantum Superconducting Circuits*. OUP Oxford.

[36] Einstein, A., Podolsky, B., and Rosen, N. (1935). Can quantum-mechanical description of physical reality be considered complete? *Phys. Rev.*, **47**:777.

[37] Eldridge, J., Pala, M. G., Governale, M., and König, J. (2010). Superconducting proximity effect in interacting double-dot systems. *Phys. Rev. B*, **82**:184507.

[38] Epstein, R. J., Seidelin, S., Leibfried, D., Wesenberg, J. H., Bollinger, J. J., Amini, J. M., Blakestad, R. B., Britton, J., Home, J. P., Itano, W. M., Jost, J. D., Knill, E., Langer, C., Ozeri, R., Shiga, N., and Wineland, D. J. (2007). Simplified motional heating rate measurements of trapped ions. *Phys. Rev. A*, **76**:033411.

[39] Ermentrout, G. (1990). Oscillator death in populations of "all to all" coupled nonlinear oscillators. *Physica D*, **41**:219.

[40] Falci, G., Feinberg, D., and Hekking, F. W. J. (2001). Correlated tunneling into a superconductor in a multiprobe hybrid structure. *EPL*, **54**:255.

[41] Gardiner, C. and Zoller, P. (2004). *Quantum Noise: A Handbook of Markovian and Non-Markovian Quantum Stochastic Methods with Applications to Quantum Optics.* Springer, 3rd edition.

[42] Giorgi, G. L., Galve, F., Manzano, G., Colet, P., and Zambrini, R. (2012). Quantum correlations and mutual synchronization. *Phys. Rev. A*, **85**:052101.

[43] Giustina, M., Versteegh, M. A. M., Wengerowsky, S., Handsteiner, J., Hochrainer, A., Phelan, K., Steinlechner, F., Kofler, J., Larsson, J.-A., Abellán, C., Amaya, W., Pruneri, V., Mitchell, M. W., Beyer, J., Gerrits, T., Lita, A. E., Shalm, L. K., Nam, S. W., Scheidl, T., Ursin, R., Wittmann, B., and Zeilinger, A. (2015). Significant-loophole-free test of Bell's theorem with entangled photons. *Phys. Rev. Lett.*, **115**:250401.

[44] Goldhaber-Gordon, D., Shtrikman, H., Mahalu, D., Abusch-Magder, D., Meirav, U., and Kastner, M. A. (1998). Kondo effect in a single-electron transistor. *Nature*, **391**:156.

[45] Goodwin, J. F., Stutter, G., Thompson, R. C., and Segal, D. M. (2016). Resolved-sideband laser cooling in a Penning trap. *Phys. Rev. Lett.*, **116**:143002.

[46] Gywat, O., Krenner, H., and Berezovsky, J. (2010). *Spins in Optically Active Quantum Dots.* Wiley-VCH.

[47] Haake, F. and Lewenstein, M. (1983). Adiabatic expansion for the single-mode laser. *Phys. Rev. A*, **27**:1013.

[48] Heinrich, G., Ludwig, M., Qian, J., Kubala, B., and Marquardt, F. (2011). Collective dynamics in optomechanical arrays. *Phys. Rev. Lett.*, **107**:043603.

[49] Hensen, B., Bernien, H., Dreau, A. E., Reiserer, A., Kalb, N., Blok, M. S., Ruitenberg, J., Vermeulen, R. F. L., Schouten, R. N., Abellan, C., Amaya, W., Pruneri, V., Mitchell, M. W., Markham, M., Twitchen, D. J., Elkouss, D., Wehner, S., Taminiau, T. H., and Hanson, R. (2015). Loophole-free Bell inequality violation using electron spins separated by 1.3 kilometres. *Nature*, **526**:682.

[50] Herrmann, L. G., Portier, F., Roche, P., Yeyati, A. L., Kontos, T., and Strunk, C. (2010). Carbon nanotubes as Cooper-pair beam splitters. *Phys. Rev. Lett.*, **104**:026801.

[51] Hofstetter, L., Csonka, S., Baumgartner, A., Fülöp, G., d'Hollosy, S., Nygård, J., and Schönenberger, C. (2011). Finite-bias Cooper pair splitting. *Phys. Rev. Lett.*, **107**:136801.

[52] Hofstetter, L., Csonka, S., Nygard, J., and Schönenberger, C. (2009). Cooper pair splitter realized in a two-quantum-dot y-junction. *Nature*, **461**:960.

[53] Holmes, C. A., Meaney, C. P., and Milburn, G. J. (2012). Synchronization of many nanomechanical resonators coupled via a common cavity field. *Phys. Rev. E*, **85**:066203.

[54] Home, J. P., Hanneke, D., Jost, J. D., Leibfried, D., and Wineland, D. J. (2011). Normal modes of trapped ions in the presence of anharmonic trap potentials. *New J. Phys.*, **13**:073026.

[55] Hush, M. R., Li, W., Genway, S., Lesanovsky, I., and Armour, A. D. (2015). Spin correlations as a probe of quantum synchronization in trapped-ion phonon lasers. *Phys. Rev. A*, **91**:061401.

[56] Huygens, C. (1986). *Christiaan Huygens' the pendulum clock, or, Geometrical demonstrations concerning the motion of pendula as applied to clocks.* Ames : Iowa State University Press.

[57] Ishibashi, K. and Kanamoto, R. (2017). Oscillation collapse in coupled quantum van der Pol oscillators. *Phys. Rev. E*, **96**:052210.

[58] Jacobs, K. and Landahl, A. J. (2009). Engineering giant nonlinearities in quantum nanosystems. *Phys. Rev. Lett.*, **103**:067201.

[59] Jin, J., Rossini, D., Fazio, R., Leib, M., and Hartmann, M. J. (2013). Photon solid phases in driven arrays of nonlinearly coupled cavities. *Phys. Rev. Lett.*, **110**:163605.

[60] Johansson, J., Nation, P., and Nori, F. (2012). Qutip: An open-source Python framework for the dynamics of open quantum systems. *Comput. Phys. Commun.*, **183**:1760.

[61] Johansson, J., Nation, P., and Nori, F. (2013). Qutip 2: A Python framework for the dynamics of open quantum systems. *Comput. Phys. Commun.*, **184**:1234.

[62] Kenfack, A. and Życzkowski, K. (2004). Negativity of the Wigner function as an indicator of non-classicality. *J. Opt. B Quantum Semiclassical Opt.*, **6**:396.

[63] Kheruntsyan, K. V. (1999). Wigner function for a driven anharmonic oscillator. *J. Opt. B Quantum Semiclassical Opt.*, **1**:225.

[64] Kimble, H. J. (2008). The quantum internet. *Nature*, **453**:1023.

[65] Kippenberg, T. J., Rokhsari, H., Carmon, T., Scherer, A., and Vahala, K. J. (2005). Analysis of radiation-pressure induced mechanical oscillation of an optical microcavity. *Phys. Rev. Lett.*, **95**:033901.

[66] Kleckner, D., Pepper, B., Jeffrey, E., Sonin, P., Thon, S. M., and Bouwmeester, D. (2011). Optomechanical trampoline resonators. *Opt. Express*, 19:19708.

[67] Kloeden, P. and Platen, E. (1992). *Numerical Solution of Stochastic Differential Equations.* Springer.

[68] Koseska, A., Volkov, E., and Kurths, J. (2013a). Oscillation quenching mechanisms: Amplitude vs. oscillation death. *Phys. Rep.*, **531**:173.

[69] Koseska, A., Volkov, E., and Kurths, J. (2013b). Transition from amplitude to oscillation death via Turing bifurcation. *Phys. Rev. Lett.*, **111**:024103.

[70] Landa, P. S. (1996). *Nonlinear Oscillations and Waves in Dynamical Systems.* Kluwer Academic Publishers.

[71] Lee, T. E., Chan, C.-K., and Wang, S. (2014). Entanglement tongue and quantum synchronization of disordered oscillators. *Phys. Rev. E*, **89**:022913.

[72] Lee, T. E. and Sadeghpour, H. R. (2013). Quantum synchronization of quantum van der Pol oscillators with trapped ions. *Phys. Rev. Lett.*, **111**:234101.

[73] Leibfried, D., Blatt, R., Monroe, C., and Wineland, D. (2003). Quantum dynamics of single trapped ions. *Rev. Mod. Phys.*, **75**:281.

[74] Leijnse, M. and Flensberg, K. (2012). Parity qubits and poor man's Majorana bound states in double quantum dots. *Phys. Rev. B*, **86**:134528.

[75] Lesovik, G. B., Martin, T., and Blatter, G. (2001). Electronic entanglement in the vicinity of a superconductor. *Eur. Phys. J. B*, **24**:287.

[76] Li, A. C. Y., Petruccione, F., and Koch, J. (2014). Perturbative approach to Markovian open quantum systems. *Sci. Rep.*, **4**:4887.

[77] Lörch, N., Amitai, E., Nunnenkamp, A., and Bruder, C. (2016). Genuine quantum signatures in synchronization of anharmonic self-oscillators. *Phys. Rev. Lett.*, **117**:073601.

[78] Lörch, N., Nigg, S. E., Nunnenkamp, A., Tiwari, R. P., and Bruder, C. (2017). Quantum synchronization blockade: Energy quantization hinders synchronization of identical oscillators. *Phys. Rev. Lett.*, **118**:243602.

[79] Lörch, N., Qian, J., Clerk, A., Marquardt, F., and Hammerer, K. (2014). Laser theory for optomechanics: Limit cycles in the quantum regime. *Phys. Rev. X*, **4**:011015.

[80] Lü, X.-Y., Liao, J.-Q., Tian, L., and Nori, F. (2015). Steady-state mechanical squeezing in an optomechanical system via Duffing nonlinearity. *Phys. Rev. A*, **91**:013834.

[81] Ludwig, M., Kubala, B., and Marquardt, F. (2008). The optomechanical instability in the quantum regime. *New J. Phys.*, **10**:095013.

[82] Ludwig, M. and Marquardt, F. (2013). Quantum many-body dynamics in optomechanical arrays. *Phys. Rev. Lett.*, **111**:073603.

[83] Mari, A., Farace, A., Didier, N., Giovannetti, V., and Fazio, R. (2013). Measures of quantum synchronization in continuous variable systems. *Phys. Rev. Lett.*, **111**:103605.

[84] Marquardt, F., Chen, J. P., Clerk, A. A., and Girvin, S. M. (2007). Quantum theory of cavity-assisted sideband cooling of mechanical motion. *Phys. Rev. Lett.*, **99**:093902.

[85] Marquardt, F., Harris, J. G. E., and Girvin, S. M. (2006). Dynamical multistability induced by radiation pressure in high-finesse micromechanical optical cavities. *Phys. Rev. Lett.*, **96**:103901.

[86] Matheny, M. H., Grau, M., Villanueva, L. G., Karabalin, R. B., Cross, M. C., and Roukes, M. L. (2014). Phase synchronization of two anharmonic nanomechanical oscillators. *Phys. Rev. Lett.*, **112**:014101.

[87] Metzger, C., Ludwig, M., Neuenhahn, C., Ortlieb, A., Favero, I., Karrai, K., and Marquardt, F. (2008). Self-induced oscillations in an optomechanical system driven by bolometric backaction. *Phys. Rev. Lett.*, **101**:133903.

[88] Mirollo, R. E. and Strogatz, S. H. (1990). Amplitude death in an array of limit-cycle oscillators. *J. Stat. Phys.*, **60**:245.

[89] Mogilevtsev, D., Slepyan, G. Y., Garusov, E., Kilin, S. Y., and Korolkova, N. (2015). Quantum tight-binding chains with dissipative coupling. *New J. Phys.*, **17**:043065.

[90] Navarrete-Benlloch, C., Weiss, T., Walter, S., and de Valcárcel, G. J. (2017). General linearized theory of quantum fluctuations around arbitrary limit cycles. *Phys. Rev. Lett.*, **119**:133601.

[91] Nigg, S. E., Tiwari, R. P., Walter, S., and Schmidt, T. L. (2015). Detecting nonlocal Cooper pair entanglement by optical Bell inequality violation. *Phys. Rev. B*, **91**:094516.

[92] Nunnenkamp, A., Børkje, K., Harris, J. G. E., and Girvin, S. M. (2010). Cooling and squeezing via quadratic optomechanical coupling. *Phys. Rev. A*, **82**:021806.

[93] Okamoto, K., Kijima, A., Umeno, Y., and Shima, H. (2016). Synchronization in flickering of three-coupled candle flames. *Sci. Rep.*, **6**:36145.

[94] Ono, K., Austing, D. G., Tokura, Y., and Tarucha, S. (2002). Current rectification by Pauli exclusion in a weakly coupled double quantum dot system. *Science*, **297**:1313.

[95] Ozden, I., Venkataramani, S., Long, M. A., Connors, B. W., and Nurmikko, A. V. (2004). Strong coupling of nonlinear electronic and biological oscillators: Reaching the "amplitude death" regime. *Phys. Rev. Lett.*, **93**:158102.

[96] Palomaki, T. A., Harlow, J. W., Teufel, J. D., Simmonds, R. W., and Lehnert, K. W. (2013). Coherent state transfer between itinerant microwave fields and a mechanical oscillator. *Nature*, **495**:210.

[97] Peixoto de Faria, J. (2006). Time evolution of the classical and quantum mechanical versions of diffusive anharmonic oscillator: an example of Lie algebraic techniques. *Eur. Phys. J. D*, **42**:153.

[98] Petta, J. R., Johnson, A. C., Taylor, J. M., Laird, E. A., Yacoby, A., Lukin, M. D., Marcus, C. M., Hanson, M. P., and Gossard, A. C. (2005). Coherent manipulation of coupled electron spins in semiconductor quantum dots. *Science*, **309**:2180.

[99] Pikovsky, A., Rosenblum, M., and Kurths, J. (2003). *Synchronization: A Universal Concept in Nonlinear Sciences*. Cambridge University Press.

[100] Purdy, T. P., Brooks, D. W. C., Botter, T., Brahms, N., Ma, Z.-Y., and Stamper-Kurn, D. M. (2010). Tunable cavity optomechanics with ultracold atoms. *Phys. Rev. Lett.*, **105**:133602.

[101] Purdy, T. P., Peterson, R. W., and Regal, C. A. (2013). Observation of radiation pressure shot noise on a macroscopic object. *Science*, **339**:801.

[102] Qian, J., Clerk, A. A., Hammerer, K., and Marquardt, F. (2012). Quantum signatures of the optomechanical instability. *Phys. Rev. Lett.*, **109**:253601.

[103] Rech, J., Chevallier, D., Jonckheere, T., and Martin, T. (2012). Current correlations in an interacting Cooper-pair beam splitter. *Phys. Rev. B*, **85**:035419.

[104] Recher, P., Sukhorukov, E. V., and Loss, D. (2001). Andreev tunneling, Coulomb blockade, and resonant transport of nonlocal spin-entangled electrons. *Phys. Rev. B*, **63**:165314.

[105] Rips, S., Kiffner, M., Wilson-Rae, I., and Hartmann, M. J. (2012). Steady-state negative Wigner functions of nonlinear nanomechanical oscillators. *New J. Phys.*, **14**:023042.

[106] Risken, H. (1984). *The Fokker-Planck Equation*. Springer.

[107] Rodrigues, D. A. and Armour, A. D. (2010). Amplitude noise suppression in cavity-driven oscillations of a mechanical resonator. *Phys. Rev. Lett.*, **104**:053601.

[108] Roth, A. and Hammerer, K. (2016). Synchronization of active atomic clocks via quantum and classical channels. *Phys. Rev. A*, **94**:043841.

[109] Safavi-Naeini, A. H., Hill, J. T., Meenehan, S., Chan, J., Gröblacher, S., and Painter, O. (2014). Two-dimensional phononic-photonic band gap optomechanical crystal cavity. *Phys. Rev. Lett.*, **112**:153603.

[110] Salomaa, M. M. (1988). Schrieffer-Wolff transformation for the Anderson Hamiltonian in a superconductor. *Phys. Rev. B*, **37**:9312.

[111] Samuelsson, P., Sukhorukov, E. V., and Büttiker, M. (2004). Electrical current noise of a beamsplitter as a test of spin entanglement. *Phys. Rev. B*, **70**:115330.

[112] Saxena, G., Prasad, A., and Ramaswamy, R. (2012). Amplitude death: The emergence of stationarity in coupled nonlinear systems. *Phys. Rep.*, **521**:205.

[113] Schindele, J., Baumgartner, A., and Schönenberger, C. (2012). Near-unity Cooper pair splitting efficiency. *Phys. Rev. Lett.*, **109**:157002.

[114] Schindler, P., Müller, M., Nigg, D., Barreiro, J. T., Martinez, E. A., Hennrich, M., Monz, T., Diehl, S., Zoller, P., and Blatt, R. (2013). Quantum simulation of dynamical maps with trapped ions. *Nat. Phys.*, **9**:361.

[115] Schoelkopf, R. J., Wahlgren, P., Kozhevnikov, A. A., Delsing, P., and Prober, D. E. (1998). The radio-frequency single-electron transistor (RF-SET): A fast and ultrasensitive electrometer. *Science*, **280**:1238.

[116] Schrieffer, J. R. and Wolff, P. A. (1966). Relation between the Anderson and Kondo Hamiltonians. *Phys. Rev.*, **149**:491.

[117] Schrödinger, E. (1935). Discussion of probability relations between separated systems. *Math. Proc. Cambridge*, **31**:555.

[118] Shalm, L. K., Meyer-Scott, E., Christensen, B. G., Bierhorst, P., Wayne, M. A., Stevens, M. J., Gerrits, T., Glancy, S., Hamel, D. R., Allman, M. S., Coakley, K. J., Dyer, S. D., Hodge, C., Lita, A. E., Verma, V. B., Lambrocco, C., Tortorici, E., Migdall, A. L., Zhang, Y., Kumor, D. R., Farr, W. H., Marsili, F., Shaw, M. D., Stern, J. A., Abellán, C., Amaya, W., Pruneri, V., Jennewein, T., Mitchell, M. W., Kwiat, P. G., Bienfang, J. C., Mirin, R. P., Knill, E., and Nam, S. W. (2015). Strong loophole-free test of local realism. *Phys. Rev. Lett.*, **115**:250402.

[119] Shlomi, K., Yuvaraj, D., Baskin, I., Suchoi, O., Winik, R., and Buks, E. (2015). Synchronization in an optomechanical cavity. *Phys. Rev. E*, **91**:032910.

[120] Sonar, S., Hajdušek, M., Mukherjee, M., Fazio, R., Vedral, V., Vinjanampathy, S., and Kwek, L.-C. (2018). Squeezing enhances quantum synchronization. *Phys. Rev. Lett.*, **120**:163601.

[121] Sothmann, B. and Tiwari, R. P. (2015). Josephson response of a conventional and a noncentrosymmetric superconductor coupled via a double quantum dot. *Phys. Rev. B*, **92**:014504.

[122] Sothmann, B., Weiss, S., Governale, M., and König, J. (2014). Unconventional superconductivity in double quantum dots. *Phys. Rev. B*, **90**:220501.

[123] Stanoyevitch, A. (2005). *Introduction to Numerical Ordinary and Partial Differential Equations Using Matlab*. Wiley-Interscience.

[124] Strogatz, S. H. (2003). *Sync: How Order Emerges from Chaos in the Universe, Nature, and Daily Life*. Hachette Books.

[125] Teufel, J. D., Donner, T., Li, D., Harlow, J. W., Allman, M. S., Cicak, K., Sirois, A. J., Whittaker, J. D., Lehnert, K. W., and Simmonds, R. W. (2011). Sideband cooling of micromechanical motion to the quantum ground state. *Nature*, **475**:359.

[126] Thompson, J. D., Zwickl, B. M., Jayich, A. M., Marquardt, F., Girvin, S. M., and Harris, J. G. E. (2008). Strong dispersive coupling of a high-finesse cavity to a micromechanical membrane. *Nature*, **452**:72.

[127] Tiwari, R. P., Belzig, W., Sigrist, M., and Bruder, C. (2014). Quantum transport signatures of chiral edge states in Sr_2RuO_4. *Phys. Rev. B*, **89**:184512.

[128] Ullner, E., Zaikin, A., Volkov, E. I., and García-Ojalvo, J. (2007). Multistability and clustering in a population of synthetic genetic oscillators via phase-repulsive cell-to-cell communication. *Phys. Rev. Lett.*, **99**:148103.

[129] Ursin, R., Tiefenbacher, F., Schmitt-Manderbach, T., Weier, H., Scheidl, T., Lindenthal, M., Blauensteiner, B., Jennewein, T., Perdigues, J., Trojek, P., Omer, B., Furst, M., Meyenburg, M., Rarity, J., Sodnik, Z., Barbieri, C., Weinfurter, H., and Zeilinger, A. (2007). Entanglement-based quantum communication over 144km. *Nat. Phys.*, **3**:481.

[130] van der Pol, B. (1926). On "relaxation-oscillations". *The London, Edinburgh, and Dublin Philosophical Magazine and Journal of Science*, **7**:978.

[131] van der Pol, B. and van der Mark, J. (1928). The heartbeat considered as a relaxation oscillation, and an electrical model of the heart. *The London, Edinburgh, and Dublin Philosophical Magazine and Journal of Science*, **6**:763.

[132] Walls, D. F. and Milburn, G. J. (2008). *Quantum Optics*. Springer, 2nd edition.

[133] Walter, S., Budich, J. C., Eisert, J., and Trauzettel, B. (2013). Entanglement of nanoelectromechanical oscillators by Cooper-pair tunneling. *Phys. Rev. B*, **88**:035441.

[134] Walter, S., Nunnenkamp, A., and Bruder, C. (2014). Quantum synchronization of a driven self-sustained oscillator. *Phys. Rev. Lett.*, **112**:094102.

[135] Walter, S., Nunnenkamp, A., and Bruder, C. (2015). Quantum synchronization of two van der Pol oscillators. *Ann. Phys.*, **527**:131.

[136] Wang, L. and Babikov, D. (2011). Adiabatic coherent control in the anharmonic ion trap: Numerical analysis of vibrational anharmonicities. *Phys. Rev. A*, **83**:022305.

[137] Weiss, T. (2017). *Nonlinear dynamics in quantum synchronization and topological transport*. PhD thesis, Friedrich-Alexander-Universität Erlangen-Nürnberg.

[138] Weiss, T., Kronwald, A., and Marquardt, F. (2016). Noise-induced transitions in optomechanical synchronization. *New J. Phys.*, **18**:013043.

[139] Weiss, T., Walter, S., and Marquardt, F. (2017). Quantum-coherent phase oscillations in synchronization. *Phys. Rev. A*, **95**:041802.

[140] Wigner, E. (1932). On the quantum correction for thermodynamic equilibrium. *Phys. Rev.*, **40**:749.

[141] Wilson-Rae, I., Nooshi, N., Zwerger, W., and Kippenberg, T. J. (2007). Theory of ground state cooling of a mechanical oscillator using dynamical backaction. *Phys. Rev. Lett.*, **99**:093901.

[142] Xu, M. and Holland, M. J. (2015). Conditional Ramsey spectroscopy with synchronized atoms. *Phys. Rev. Lett.*, **114**:103601.

[143] Xu, M., Tieri, D. A., Fine, E. C., Thompson, J. K., and Holland, M. J. (2014). Synchronization of two ensembles of atoms. *Phys. Rev. Lett.*, **113**:154101.

[144] Yin, X.-F., Zhang, W.-Z., and Zhou, L. (2017). The synchronization and entanglement of optomechanical systems. *J. Mod. Opt.*, **64**:578.

[145] Zaitsev, S., Pandey, A. K., Shtempluck, O., and Buks, E. (2011). Forced and self-excited oscillations of an optomechanical cavity. *Phys. Rev. E*, **84**:046605.

[146] Zhang, J., Peng, B., Özdemir, S. K., Liu, Y.-X., Jing, H., Lü, X.-Y., Liu, Y.-l., Yang, L., and Nori, F. (2015a). Giant nonlinearity via breaking parity-time symmetry: A route to low-threshold phonon diodes. *Phys. Rev. B*, **92**:115407.

[147] Zhang, M., Shah, S., Cardenas, J., and Lipson, M. (2015b). Synchronization and phase noise reduction in micromechanical oscillator arrays coupled through light. *Phys. Rev. Lett.*, **115**:163902.

[148] Zhang, M., Wiederhecker, G. S., Manipatruni, S., Barnard, A., McEuen, P., and Lipson, M. (2012). Synchronization of micromechanical oscillators using light. *Phys. Rev. Lett.*, **109**:233906.

[149] Zhao, M. and Babikov, D. (2008). Coherent and optimal control of adiabatic motion of ions in a trap. *Phys. Rev. A*, **77**:012338.

[150] Zhirov, O. and Shepelyansky, D. (2006). Quantum synchronization. *Eur. Phys. J. D*, **38**:375.

[151] Zhu, B., Schachenmayer, J., Xu, M., Herrera, F., Restrepo, J. G., Holland, M. J., and Rey, A. M. (2015). Synchronization of interacting quantum dipoles. *New J. Phys.*, **17**:083063.